UNIVERSIDAD COMPLUTENSE DE MADRID

FACULTAD DE CIENCIAS FÍSICAS
Departamento de Física de Materiales

OPTICAL AND TRANSPORT PROPERTIES OF COMPLEX MOLECULAR SYSTEMS.

MEMORIA PARA OPTAR AL GRADO DE DOCTOR

PRESENTADA POR

Elena Díaz García

Bajo la dirección del doctor

Francisco Domínguez-Adame Acosta

Madrid, 2010

- **ISBN: 978-84-693-3354-9**

Departamento de Física de Materiales
Facultad de Ciencias Físicas
Universidad Complutense de Madrid

PROPIEDADES ÓPTICAS Y DE TRANSPORTE DE SISTEMAS MOLECULARES COMPLEJOS

OPTICAL AND TRANSPORT PROPERTIES OF COMPLEX MOLECULAR SYSTEMS

Memoria de Tesis presentada para la obtencion
del título de Doctor en Física por:
Elena Díaz García

Dirigida por:
Dr. Francisco Domínguez-Adame Acosta.

A mi familia

Agradecimientos

Mi primer gracias ha de ir dedicado al que ha sido mi mentor desde el primer día que empecé en el mundo de la investigación, al Prof. Francisco Domínguez-Adame. A él he de agradecer todo su esfuerzo y dedicación, destacando sobre todo su admirable sentido de la seriedad en el trabajo.

También me gustaría mostar mi gratitud a personas con las que he colaborado en algunos de los trabajos relacionados con esta tesis. Entre ellas destaco a, Víctor Malyshev que ha estado presente en mayor o menor medida a lo largo de todo mi doctorado, Ara Sedrakyan que me enseñó lo que era Mathematica y me dedicó sin limites su tiempo y su esfuerzo, Andrey Malyshev cuyos consejos sobre cálculo numérico y su interpretación física han sido de gran valor, Rodrigo Lima con el que ha sido un placer trabajar codo con codo en un ambiente amistoso y distendido, y por último, Erik Schultes que me enseñó todo lo que sé sobre la vida en el laboratorio en un fascinante ambiente lleno de optimismo.

Aparte de estos colaboradores directos, quiero destacar el apoyo del resto de componentes de mi grupo de investigación Antonio Rodriguez, Mario Amado, Clara González-Santander y Javier Munárriz. Agradezco particularmente a Antonio el esfuerzo que ha dedicado a la corrección de este manuscrito y a los más jóvenes, gracias por todos las veces que os he buscado por detrás de la pantalla de mi ordenador y he encontrado vuestra ayuda. De la misma manera quiero mencionar al GISC-Grupo Interdisciplinar de Sistemas Complejos por su apoyo y por los buenos ratos.

No debo olvidar tampoco agradecer al Departamento de Física de Materiales de la UCM por haberme acogido de forma excepcional desde el primer día, así como la hospitalidad que me brindaron Cord Müller, Jasper Knoester y Thomas Labean en las estancias de investigación que he realizado en el extranjero durante los años de mi doctorado.

Dicho esto, fuera de lo profesional quiero dar las gracias en primer lugar, y con mayúsculas, a mis padres y a mi hermano. Gracias por todo, por tantas cosas que no cabrían ni en una enciclopedia y por más, que ni si quiera haya sido consciente de ellas. Por ayudarme con mis primeras ecuaciones en el cole, por obligarme a estudiar inglés, por arreglarme el flexo o montarme la silla anatómica y por supuesto por venir a la mesa

y decirme, qué tal vas enana? y luego echarnos unos bailes. De la misma manera quiero agradecer de forma destacada a mis otras dos madres, mi tía y mi abuela, por transmitirme todo el cariño y sabiduría popular que en la universidad no se enseña. Y extendiéndome un poco más, agradezco de verdad a toda mi familia por el apoyo que durante estos años me han aportado incluso no entendiendo muy bien a qué me dedicaba, gracias por estar orgullosos de mí!

Mis amigos también han jugado un papel fundamental en esta etapa. Gracias a Vicky, Marcos, Blanca, Celia y Mario, por estar ahí incondicionalmente. Y gracias al resto de mis compañeros de la carrera, Chechu, Sergio, Jarín, Dani, Willy... por todo lo que hemos compartido. Gracias a Inés por nuestras apasionantes conversaciones y a Raquel por los viajes, las lecciones sobre la vida del investigador y especialmente por prestarme la quote de su tesis.

Gracias a toda la gente con la que he coincidido en mi departamento, desde los comienzos hasta ahora: a Manu, Lucas, David, Violeta, Pili, Óscar, Rocío, Emilio, Clara, Irene, Belén, Ángela, Javi... gracias por todas las veces que me habéis ayudado en el día a día del doctorando y por supuesto, por haber creado un ambiente de trabajo y personal maravilloso que se resume en el concepto cuchipanda.

Y por último doy las gracias al Dr. Cabrera por ayudarme con cualquier cosa a cualquier hora, gracias por dejarme aprovechar su testarudez para resolver cualquier problema de ciencia, software o hardware. Igualmente, agradezco a Edu por ser como es, por haber sido mi primer contacto dentro del sistema, por haberme trasmitido parte de su admirable pragmatismo y por enseñarme el bosque escondido entre los arboles. Gracias por la paz que emanas y por compartirla conmigo.

A todos vosotros, mil gracias por haber compartido conmigo la etapa que hoy llega a su fin. Os espero en la próxima!

Man muss nicht alles wissen, man muss nur wissen, wo es zu suchen ist.

ALBERT EINSTEIN

Contents

Chapter 1

Introduction

1.1. Why molecular systems?

The research on complex molecular systems offers fascinating questions to challenge the theoretical and experimental physicists. This is a highly interdisciplinary field of study where the collaboration between physicist, chemists and biologists is crucial [1,2]. The variety of molecules in nature is already enormous if we think about the proteins, DNAs or RNAs for instance. But in the same way we could hardly imagine our nowadays life without a great number of synthetic macromolecules like polyethylene, polystyrene or Teflon [3]. Generally speaking, these complex molecular systems can be formed by many identical or different molecules units bound together by intermolecular interactions, especially Van der Waals forces [4]. Such molecular interactions are indeed the basis of many highly selective recognition, transport and regulatory processes in biological systems [5].

The physical contributions to this topic have initially focused on the structural characterization by X-ray or neutron diffraction and magnetic resonance techniques [6]. However, experimental and theoretical approaches from physics are also necessary to describe the conformation and organization of molecular systems and to establish the physical rules taking place in the construction of such systems. Such

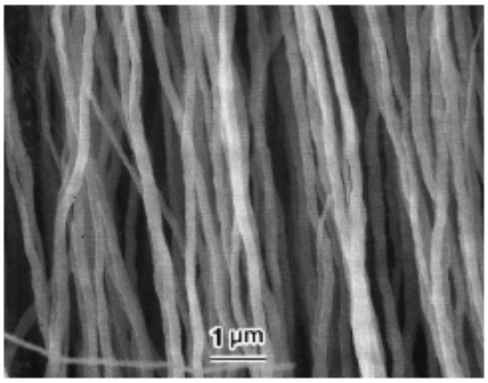

Figure 1.1. *Scanning electron microscope image of the aligned polyacetylene thin film with uniaxially oriented fibril morphology. The film contains partially disordered strands of linear polymer molecules. This picture was taken by M. Kyotani and coworkers in Ref. [9].*

a study is absolutely relevant to determine their possible functionality and their reaction ability.

Among the physical interests in this area, one of the most important is the search for molecular systems with a high electrical conductivity. In the last years, this became one of the main objectives in the development of the molecular electronics as we will see later [7]. For example, since the discovery of the doped polyacetylene $(CH)_n$ which presents highly conducting properties [8], a lot of research effort has been focused on the study of the conducting behavior of polymers. Figure. 1.1 shows a scanning electron microscope image of polyacetylene molecules aligned in a thin film.

Another important property of these complex molecular systems which attracts the attention of chemists is molecular recognition. This interesting process takes place in systems where the integrating molecules are held together by intermolecular noncovalent forces so that the molecular fitting is determined electronically or geometrically [10]. By taking advantage of this property, many molecules can be specifically designed with a particular size or structure to contribute in reactions or transport processes as preferable [11].

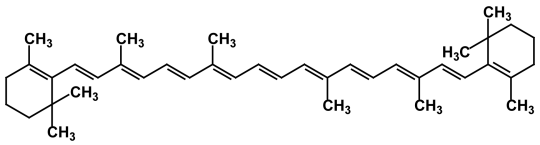

Figure 1.2. *Chemical structure of β-carotene.*

The conversion of optical radiation into chemical energy takes also place in many molecular systems. Usually the light absorption occurs in a component of the system (donor) and such excitation is driven by electronic couplings to the reaction center [12]. Remarkably, transfer of electronic excitation energy between molecules over long distances is a process of great importance in many molecular systems. Even more, by using suitable energy transfer systems, one can thus drive the energy preferentially to particular molecules with specific properties to produce preferable effects [11]. This is what occurs for instance in the so-called antenna complexes which collect light for photosynthesis, as well as in technical applications such as photography [13]. Notice that there is a wide range of J-aggregates which show these interesting functions, see Refs. [14–17]. Looking at the biological world, the most important photoreceptor involved in this kind of photoreactions is the chlorophyll [12]. This molecule consists of a large ring with delocalized electrons responsible for the characteristic light absorption of the photosynthesis. The carotenoids are also another important group of pigment molecules in plants and animals [13]. The linear chemical structure of an example of this group, β-carotene, is shown in Fig. 1.2.

The biological realm is also the best example to describe the huge possibilities of storage and transfer of information in molecular systems [12]. Proteins, which are the foundations of life, are folded polypeptide chains made up of amino acids in a specific sequence determined by the genetic code and synthesized during cell development. According to its specific sequence and structure, proteins can perform numerous biochemical functions. The biosynthesis of proteins is determined by the nucleic acids, in particular DNAs (deoxyribonucleic acids) and RNAs (ribonucleic acids). Thus, during the transcription process RNAs help to pass the stored information in DNAs on and make use of it in the proteins synthesis. DNA is a long-chain polymer

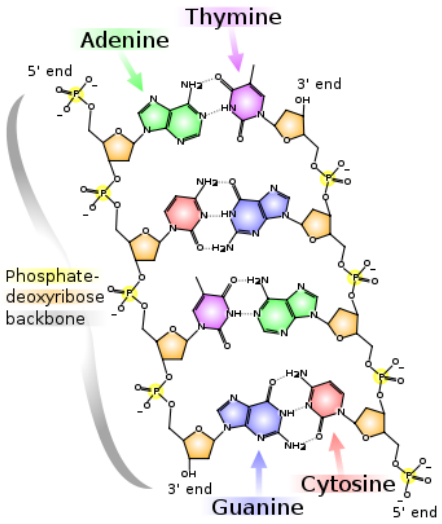

Figure 1.3. *Schematic figure of the chemical structure of a fragment of DNA double-helix.*

made up of molecules of the sugar deoxyribose together with phosphates groups which alternate with the sugar molecules to form a double-helix chain, see Fig. 1.3.

In view of all these examples, it is clear that the variety of complex molecular systems which already exist in nature and many others that can be artificially designed, constitute a huge rich field of study whose possible applications can be determinant in our future day-life[a].

1.2. Molecular electronics

Molecular chemists and condensed-matter physicists have been trying to give shape to a new idea of the conventional electronics since some years ago, the molecular electronics [7]. This relatively new term refers to the research and speculations of substituting or at least complementing the nowadays silicon-based electronics. Though its main interest is mainly focused on the miniaturization of the present-day devices, the variety of structures and functions supported by organic molecular systems, as well as the chemical control of its design and its easy production are

[a]For further reading about this topic, see Ref. [18].

very promising. The big challenge of molecular electronics is to exploit all properties of organic molecular materials related to the transmittal or storage of information. But eventually, the final objective is much more ambitious and it involves the design of electronic circuits where molecular systems play the role of conductors, switchers and logic or storage elements. A lot of interdisciplinary efforts of the current basic research are devoted to this clearly nontrivial goal in order to hopefully perform its real applications in the future.

The first devices of a circuit to think about are the conductors which connect all electronic components. The substitutes of such conductors in the molecular electronics are usually known as molecular wires. The thinnest molecular wire one can imagine is consistent of a chain of carbon atoms, which indeed exists in polymer molecules [19]. In these materials, all kind of conducting behavior can be found depending on the particular characteristics of such polymers. Other more complex candidates as molecular conductors are the polyenes which contain organic and inorganic components. However, the structural complexity of these materials has as a consequence the existence of nondesired defects in its fabrication [20]. On the contrary, among the family of carbon compounds, the carbon nanotubes are the most promising systems working as molecular wires. Their synthesis method is well established and they can behave as metals or semiconductors depending on its specific structure [21]. Besides, the possibility of a metal-insulator or metal-semiconductor phase transition induced by an electric or magnetic field brings the possibility to use these molecular wires as transistors as well [22]. As a last remark in the discussion, it is to be mentioned the contradictory but maybe promising conducting properties of DNA molecules which have been widely studied in the last decade [23]. According to experimental results, DNA molecules can behave as metals, insulators, semiconductors or even superconductors depending on the DNA sequence and the solution conditions [23]. Indeed, many electronic applications have been already proposed for DNA-based devices, although there is not a common description of the basic electronic properties of this biomolecule yet [24].

Other typical components of an electronic circuit are the switches, whose role can be played by molecules which are bistable in regard to light or to electric or

magnetic fields. An example of such molecules are the fulgides, whose photochemistry properties gives rise to a structural transformation [25]. The optical bistability properties supported by some J-aggregates can also be useful for this electronic application [26].

The light-matter interaction can also taken into account to design storage elements. Thus, it would be possible to change the state of a molecular system by the action of light into a new state which is stable and distinguishable from the initial state, and read out this information or erase it by a second light beam. The hole-burning phenomenon [27] might be useful for this application and it is based on the inhomogeneously broadening of single molecules spectral lines when dealing with the spectra of molecules embedded in a solid matrix. This broadening is typical from J-aggregates due to the influence of the local environment on the molecule energy levels [26, 28].

A further issue to be studied by molecular physicists is the transport of excitations through molecules in such a way that some specific regions of a large molecular system behaves as a wire. Nevertheless, in this process the molecules do not conduct electrical current but electronic excitation. This application was already introduced in the previous section by mentioning molecules like the photosynthesis antenna complexes and the J-aggregates which present this type of functionality [16, 17].

Needless to say that molecular recognition and self-organization properties of some molecular systems can constitute an enormous help in the design and fabrication of these molecular circuits [11]. These procedures are not affected by the typical problems occurring in the conventional lithography technics. The final structure in the natural self-assembly only depends on the initial structures of the individual components to be assembled and even more, already existent biological structures can be used as the initial template to start the self-assembling or the production process. For instance, these properties have been already well established for DNA [29, 30].

1.3. Disorder effects

Disorder can arise by nonintentional defects like in solid crystals as impurities, vacancies or dislocations or it can exist due to different local environments which is mostly the case when dealing with molecular systems. Similarly to the conclusions of the Anderson model for tridimensional systems [31], it is well established that the inclusion of uncorrelated disorder in low-dimensional lattices results in the localization of all eigenstates [32, 33]. On the contrary, some types of correlations affecting the disorder may lead to delocalized states in the thermodynamic limit [34–37]. In the case of localized states, in some specific systems the localization length might be larger than the typical system sizes used in experiments and thus, their transport properties might remind those of extended states. These localization properties are clearly crucial in the energy or charge transport in physical systems, giving rise to coherent or incoherent transport processes or a superposition of both possible mechanisms, depending on the particular system under consideration [38].

In molecular aggregates such as J-aggregates, the main source of disorder arises from the various local environments which shift the energy levels of the molecules by different amounts [39]. This leads to a inhomogeneously broadening of the absorption spectra which has been clearly observed in experiments [40].

In the case of biomolecules, such as DNA-polymers, the situation is much more complicated. On one hand, disorder effects, appearing directly from the sequence of nucleotides, have an important influence on the localization properties [41]. Besides, in vivo and most experimental situations, DNA is exposed to diverse environments which may alter its structure and properties. For instance, water molecules or counterions which surround DNA molecules, might bind with the backbone sites inducing local fluctuations of the site energies on the base pairs. This environment conditions introduce midgap states similar to those created by impurities in semiconductors which can enhance the conductivity by thermally activated hopping mechanisms [42]. On the other hand, dynamical fluctuations of the counterions can also give rise to configurations which might affect the carrier transport along the system. In particular, due to the softness of some organic molecules such as DNA-polymers,

dynamical disorder effects might lead to the excitation of low-energy vibrational modes which can couple to the charge tunneling. In this regard, a study of the electron-phonon interactions is in order in this kind of systems since they can even lead to polaron formation [43].

In view of these arguments it is clear that disorder effects have to be considered in the study of the physical properties of molecular systems which are strongly affected by environment conditions.

1.4. Main objectives of the Thesis

In the preceding sections it was argued the relevance of the study of complex molecular systems due to their promising applicability in different fields such as physics, chemistry, electronics or computer science. The difficulty of a complete description of these systems is highly increased due to the wide variety of molecular systems, as well as the different environment conditions which might affect their properties. Therefore, an interdisciplinary collaboration is necessary to describe such complex scenario with simple models based on effective interactions, whose application and understanding lead to the basic comprehension of their main properties.

This Thesis presents a study of the optical and transport properties of one and quasi-one dimensional molecular systems by way of tight-binding models which have been previously demonstrated to be a very powerful tool in this regard [44–47]. In particular this work is focused on two kind of systems: linear molecular aggregates and DNA double helix.

In ***Chapter 2*** the localization properties of a disordered one-dimensional Frenkel Hamiltonian are studied. Long-range correlations are considered in the model of disorder which is introduced in the on-site transition frequencies. Clear evidences of a localization-delocalization transition (LDT) at the center of the band in the case of strong correlations are presented. In this regard, the effect of such particular long-range correlations in biased disordered linear aggregates on the absorption spectra is studied in ***Chapter 3***. In particular, the appearance of a periodic pattern in these

spectra when a bias is present in the system and correlations are strong enough, is numerically demonstrated and attributed to the Wannier-Stark quantization. In ***Chapter 4*** we will establish a clear relationship between this quantization and the radiative decay of excitons (fluorescence). ***Chapter 5*** is dedicated to the study of the localization properties of a DNA-ladder model by means of the calculation of the Landauer and Lyapunov exponents. The intrinsic correlations due to the base complementarity in DNA are demonstrated not to give rise to extended states in the system, while the hopping parameters are revealed to have a much more important role on this regard. The optical absorption spectra of DNA-homopolymers is studied in ***Chapter 6*** by considering different DNA-ladder models. It is argued that the characterization of such spectra can contribute to a better description of the hopping parameters of the model. Disorder effects and the helix conformation impact is also considered in this study. A brief experimental proposal is introduced at the end of this chapter, pointing out the difficulties to be considered in the design of a real experimental set up.

Chapters 7 and **8** are focused on the study of transport properties of DNA-homopolymers. In ***Chapter 7*** an incoherent hopping formalism is proposed to describe the semiconducting current-voltage curves observed in some experiments. By introducing on-site disorder we demonstrated that disorder effects cannot smear out the semiconductor gap, as it is also observed in some experiments, within the master equation formalism proposed in this chapter. On the contrary, ***Chapter 8*** is dedicated to the study of coherent transport in biased systems where charge-lattice coupling is considered within the Peyrard-Bishop-Holstein model (PBH). In such a case, oscillating currents are claimed to appear in uniform DNA sequences, as well as in the case of disordered ones provided strong long-range correlations are present in the system.

Chapter 2

Localization-delocalization transition in a 1D lattice with scale-free disorder

The localization properties shown by a long-range correlated model of disorder in 1D systems is under consideration. By diagonalizing the corresponding tight-binding Hamiltonian, we will obtain the eigenstates and eigenenergies of the system. Different magnitudes of interest will be analyzed, searching for signatures of a localization-delocalization transition at the center of the band. A qualitative explanation to support our numerical results is proposed as well.

2.1. Introduction

Since the Anderson model [31] was introduced in 1958, a lot of effort has been devoted to study the localization properties of quasiparticles in disordered systems. In particular Anderson studied a tridimensional lattice with random uncorrelated site energies and nearest-neighbor interaction. He established that in such a case a localization-delocalization transition (LDT) arises, resulting in the localization of all states at large magnitude of disorder. This transition is also known as Anderson transition or metal-insulator transition. One of its main signatures is the existence of mobility edges which separate the localized and extended phases in the thermodynamic limit. Nevertheless, for low-dimensional systems Mott and Twose (1D) and Abrahams *et al.* (2D) concluded that all eigenstates are localized for any magnitude of uncorrelated disorder [32,33]. It is worth mentioning that Anderson shared the Nobel Prize in Physics with Mott and Van Vleck in 1977 by their research on the electronic structure in magnetic disordered systems [48].

At the end of the eighties some theoretical works demonstrated that even in 1D a set of discrete extended eigenstates arise if short-range correlations are included in the on-site energies [34–37]. This theoretical prediction was also experimentally proven [49]. However, this cannot be referred to as a true Anderson transition since the mobility edges are not well defined in these models.

More recent studies based on models supporting long-range correlations have demonstrated the possibility of a true LDT in these systems [50–52]. These long-range correlated disorder distributions are characterized by a power-like spectrum of the form $S(k) \propto 1/k^{\alpha}$ with $\alpha > 0$. This function corresponds to the Fourier transform of the correlator $\langle \varepsilon_i \varepsilon_j \rangle$ for the site energies ε_i and ε_j. Here the brackets indicate average over realizations of the disorder. Many stochastic processes in nature present this kind of disorder (see Ref. [53] and references therein). Particularly it seems to be involved in the long-range charge transport properties of DNA molecules [54–56].

Such disorder distributions give rise to a phase of extended states for $\alpha > \alpha_c$ at the center of the band, α_c being a threshold exponent. Moreover this phase is separated from the localized regions by two well characterized mobility edges. Needless to say, this extended phase might present very promising and unusual transport properties for future technological applications. Indeed, there exist experimental evidences of this LDT transition based on microwave transmission measurements on wave guides with correlated

scatterers [57].

From a theoretical point of view, a numerical renormalization approach proved that this model presents a phase of extended states at the center of the band for $\alpha > \alpha_c \approx 2$ in the thermodynamic limit. However, these results were checked just for a single realization of the disorder distribution [50].

Our interest is to provide new evidences of the localization properties of this kind of systems. In particular we will use the model proposed by the authors of Ref. [50]. We will give a more general and precise result than in Refs. [50–52] averaging over several disorder realizations and thus, defining in a proper way the energy of the mobility edges [51]. Furthermore we propose a qualitative explanation to understand the origin of these mobility edges.

2.2. Model

We consider a 1D chain consisting of an even number of sites N and unit spacing. Two allowed levels for every lattice site are assigned, the ground state and the excited one. The transition energy between them is written as $\mathcal{E}_n = \bar{\mathcal{E}} + \varepsilon_n$. We restrict ourselves to nearest-neighbor dipolar coupling. The transition dipole moments are assumed to be perpendicular to the lattice (J-aggregates). We choose the hopping between neighbors $J = -1$, referring all energies involved in the problem to the modulus of this unit. The Hamiltonian finally reads:

$$\mathcal{H} = \sum_{n=1}^{N} \mathcal{E}_n \, |n\rangle\langle n| - \sum_{n=1}^{N-1} \Big(|n\rangle\langle n+1| + |n+1\rangle\langle n| \Big) \, , \tag{2.1}$$

which is expressed in terms of Wannier states $|n\rangle$ localized at site n of the lattice. According to the model proposed by Moura and Lyra in Ref. [50], the diagonal disorder is introduced by means of a stochastic fluctuation in the site energies given by the trace of a fractional Brownian motion

$$\varepsilon_n = \sigma C_\alpha \sum_{k=1}^{N/2} \frac{1}{k^{\alpha/2}} \cos\left(\frac{2\pi k n}{N} + \phi_k \right) \, . \tag{2.2}$$

Here $C_\alpha = \sqrt{2}\big(\sum_{k=1}^{N/2} k^{-\alpha} \big)^{-1/2}$ is a normalization constant and $\phi_1, \ldots, \phi_{N/2}$ are $N/2$ independent random phases. They are generated using a uniform probability distribution within the interval $[0, 2\pi]$. Hereafter we set $\bar{\mathcal{E}} = 0$ without loss of generality.

The relevant correlators of this long-range correlated disorder distribution are

$$\langle \varepsilon_n \rangle = 0 \ , \tag{2.3a}$$

$$\langle \varepsilon_n^2 \rangle^{1/2} = \sigma \ , \tag{2.3b}$$

$$\langle \varepsilon_n \varepsilon_m \rangle = \frac{\sigma^2 C_\alpha^2}{2} \sum_{k=1}^{N/2} \frac{1}{k^\alpha} \cos\left[\frac{2\pi k(n-m)}{N}\right] \ . \tag{2.3c}$$

Here σ refers to the standard deviation, usually known as magnitude of disorder, and $\langle ... \rangle$ indicates average over different sets of random phases.

In this model the strength of the long-range correlations is given by the parameter α which defines the power-like Fourier spectrum $S(k) \sim 1/k^\alpha$. The larger α is, the stronger the correlations are. On the contrary if $\alpha = 0$ the Hamiltonian leads to weakly correlated site energies, see Fig. 2.1.

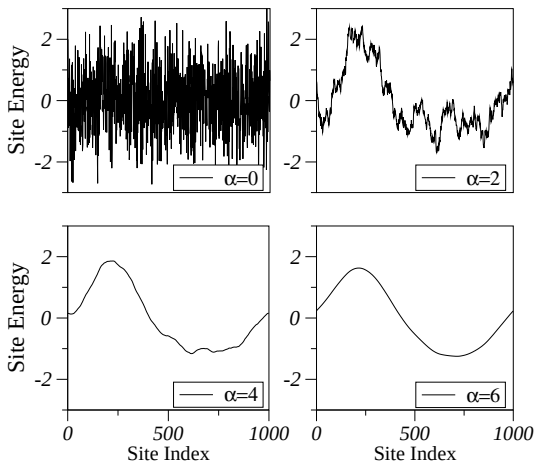

Figure 2.1. *Energy landscape obtained from a single realization of the random phases appearing in Eq. (2.2). Different correlation exponents α are considered for the same magnitude of disorder $\sigma = 1$.*

2.3. Numerical results

2.3.1. Inverse participation ratio

An interesting magnitude to study the localization properties of the eigenstates is the participation ratio (PR) or its inverse (IPR) which are defined as:

$$\mathrm{PR} = 1/\sum_{n=1}^{N} |\psi_{\nu n}|^4, \quad \mathrm{IPR} = \sum_{n=1}^{N} |\psi_{\nu n}|^4, \tag{2.4}$$

where $\psi_{\nu n}$ represents the amplitude at site n of the normalized eigenstate ν with eigenenergy E_ν.

In the case of considering Bloch states, $\psi_{kn} = \frac{1}{\sqrt{N}} \exp^{ikn}$, the probability of the particle being at any of the sites of the lattice is the same and then, $\mathrm{IPR}_{\mathrm{Bloch}} = 1/N$. Dealing with extended states which are not Bloch states, things are slightly different. Though the probability of the quasiparticle being at every site is not the same, in average the IPR depends on the size N in the same way, $\mathrm{IPR}_{\mathrm{ext}} = 1/N$.

On the other hand, if the eigenstate is localized in a finite region of the chain, its probability amplitude $\psi_{\nu n}$ will not be uniform along the chain. Indeed, it will be exactly zero for some sites, while in others it will be significantly higher to keep the eigenstate normalization. Thus, the condition $\mathrm{IPR}_{\mathrm{loc}} \gg 1/N$ arises and the size-dependence of the IPR disappears for large enough systems.

Keeping in mind these concepts, we perform the direct diagonalization of the Hamiltonian by means of a standard numerical method [58]. We obtain the eigenenergies and eigenstates of the system and calculate the IPR. Repeating this procedure for different sizes of the system within the range $1000 - 2500$ sites, we will be able to study the dependence of the IPR on the lattice size. Assuming a power-like dependence of the IPR on the system size as follows $\mathrm{IPR} = N^\beta$, we can extract information about the eigenstate localization properties through the calculation of the exponent β. Then, according to the previous arguments, $\beta \approx -1$ for extended states and $\beta = 0$ for localized ones.

Figure 2.2 shows the value of the exponent β at different eigenenergies at the center of the band and three different values of the correlation exponent α. For $\alpha = 1 < \alpha_c$ we obtain $\beta \approx 0$ as a signature of localized states, while for $\alpha = 3$ and $5 > \alpha_c$ the existence of extended states reveals an exponent β close to minus one. The fact that β does not reach the exact values zero nor one is a consequence of finite-size effects. Notice that the concept of extended state is strictly defined only in the thermodynamic limit, while we

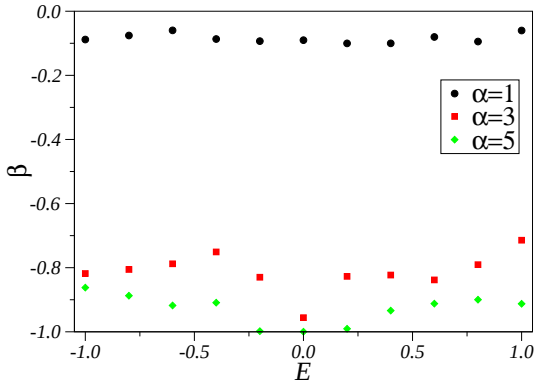

Figure 2.2. *Exponent β which defines the power dependence of the IPR on the system size for different eigenenergies and three values of α. The magnitude of disorder is $\sigma = 1$*

are dealing with systems of a maximum size of $N = 2500$. For the same reason we cannot either properly detect the mobility edges, the energies where the LDT occurs, using this procedure.

2.3.2. Transmission coefficient

In this section the transmission coefficient τ for a finite disordered chain is calculated considering plane waves with different incoming energies. To this end two semi-infinite regular chains are added to both ends of the one under study. The site energy of these new chains is set to zero and we keep considering nearest-neighbor coupling set to -1. This calculation is performed by means of an iterative method based on the transfer matrix approach [59].

In order to get information of the extended phase we study the behavior of $\log \tau$ for different system sizes and energies within the range $E = 0.0 - 1.4$. The results are summarized in Fig. 2.3 and Fig. 2.4. For $\alpha = 1 < \alpha_c$ (Fig. 2.3), the transmission coefficient decays exponentially with the system size for any value of the energy, clearly indicating the localization of the states. However for $\alpha = 3 > \alpha_c$ (Fig. 2.4), we find a phase of extended states at the center of the spectrum where the transmission coefficient keeps constant and close to one. If the spectral region where the LDT occurs is sampled more carefully (inset of Fig. 2.4), we can even approximately determine the energy where

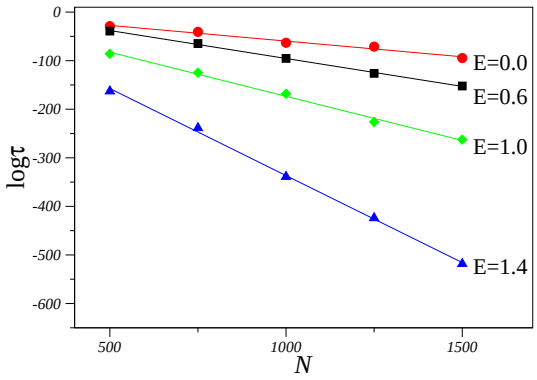

Figure 2.3. *Logarithm of the transmission coefficient as a function of the system size for different incoming energies $\sigma = 1$ and $\alpha = 1$ (circles $E = 0.0$, squares $E = 0.6$, diamonds $E = 1.0$ and triangles $E = 1.4$).*

the transition takes place, the mobility edge, at $E = 0.9 \pm 0.1$.

It is to be noticed that finite-size effects are not so relevant in the study of the transmission properties as in the case of the IPR analysis. In the former case the position of the mobility edges is defined by searching the energies for which the transmission coefficient decays exponentially with the size of the system. Therefore, this tendency is much better defined, even considering system sizes far from the thermodynamic limit, than the numerical value of the exponent β defined as IPR$= N^{\beta}$ (see previous section).

2.3.3. Phase diagram

Once evidences of the existence of an extended phase at the center of the spectrum for $\alpha > \alpha_c$ are established, a phase diagram based on the localization properties is in order. To this end we calculate the transmission coefficient in a system of $N = 3000$ sites averaging over 1000 realizations of disorder. When $\alpha > \alpha_c$ the transmission coefficient behaves as shown in Fig. 2.5 for incoming energies within the energy spectrum. It reaches unity at the center of the band where the extended states are expected, but it abruptly decreases at the mobility edges to become zero at energies of the localized states. In the case $\alpha < \alpha_c$ the transmission coefficient is vanishing small for the whole spectrum and no LDT occurs.

Taking the energies which correspond to the sharp decay of the transmission coefficient

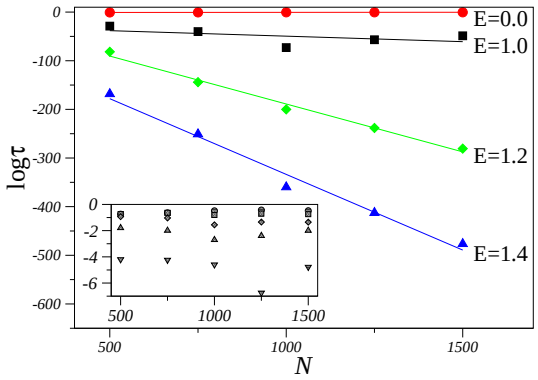

Figure 2.4. *Logarithm of the transmission coefficient as a function of the system size for different incoming energies and* $\alpha = 3$ *(circles* $E = 0.0$*, squares* $E = 1.0$*, diamonds* $E = 1.2$ *and triangles* $E = 1.4$*). The inset presents in detail the behavior of* $\log \tau$ *at the center of the band (circles* $E = 0.0$*, squares* $E = 0.2$*, diamonds* $E = 0.4$*, triangles up* $E = 0.6$ *and triangles down* $E = 0.8$*).*

for every value of α as the mobility edges, we obtain the phase diagram presented in Fig. 2.6. We find a central phase of extended states for values of α larger than a critical one around $\alpha_c \approx 2$ but slightly lower, see Ref. [50]. The reason why it happens is again related to finite-size effects which strongly affect these calculations in a system of $N = 3000$ sites, especially in the vicinity of the mobility edges where the LDT transition occurs. Besides, the extended phase seems to broaden by increasing the value α over the critical one. However its width saturates for $\alpha > 4$ within the energies $[-1.0, 1.0]$. Once again the results of Ref. [50] are confirmed in a qualitative way. Notice that our calculations were performed after averaging over 1000 realizations of disorder while Moura and Lyra considered just one. Therefore, our results are more meaningful and should be taken into account for completeness.

2.4. Qualitative explanation

An analysis of the long-range correlated disorder distribution Eq. (2.2) will make clear our results. The idea is to make some approximations in the distribution of disordered energies (see Fig. 2.7). Bear in mind that it is the sum of harmonic terms whose amplitude is proportional to $k^{-\alpha/2}$. Then, if we consider a large enough α we could keep the first

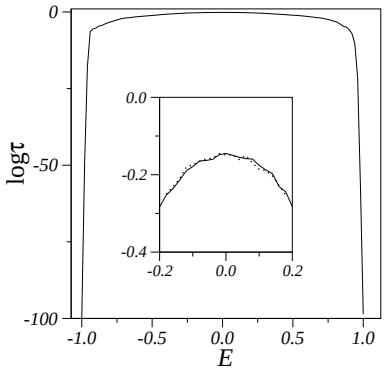

Figure 2.5. *Logarithm of the transmission coefficient as a function of the incoming energy for* $\sigma = 1$, $\alpha = 4$ *and* $N = 3000$. *The inset compares* $\log\tau$ *at the center of the band for two different sizes of the system: solid line* $N = 3000$ *and dashed line* $N = 30000$, *showing that* τ *is size-independent.*

term and neglect the rest since this term is clearly the dominant one. According to this approximation we neglect the summation and the potential profile becomes harmonic with period N. Furthermore we can design a sinusoidal landscape by choosing the initial phase $\phi_1 = -\pi/2$. In such a case, the middle point of the chain coincides with half of the period of the harmonic distribution and a change of sign in the site energies arises at $N/2$. To simplify our reasoning even more we can approximate the site energies of both halves of the chain by the mean value of the sine function in both regions $\pm\bar{\varepsilon}$, where $\bar{\varepsilon} = 2\sigma C_\alpha \pi = 0.63\sigma C_\alpha$, being positive and negative in the first and the second half of the chain respectively (see Fig. 2.7). The new energy landscape becomes $\varepsilon_n = \bar{\varepsilon}$ $\mathrm{sgn}(N/2 - n)$ and we could understand the system like two uniform coupled chains of length $N/2$ hereafter. However, this coupling can be reasonably neglected so that both chains are expected to support an allowed band within the energies $[\pm\bar{\varepsilon} - 2, \pm\bar{\varepsilon} + 2]$. This is the case according to the following estimations. Let us consider the elements of the coupling matrix between the two subchains which are given by [61]

$$V_{k_l k_r} = (-1)^{k_l} \frac{4}{N+2} \sin\left(\frac{2\pi k_l}{N+2}\right) \sin\left(\frac{2\pi k_r}{N+2}\right) \ . \tag{2.5}$$

Here, k_l and k_r, ranging from 1 to $N/2$, number the eigenstates of the left and right sublattices, respectively. From Eq. (2.5) we find that the magnitude of coupling of the lowest state of the right sublattice ($k_r = 1$) to the closest state of the left one ($k_l = 1$) is

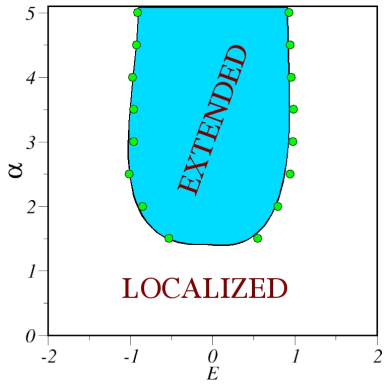

Figure 2.6. *Phase diagram obtained for a system of $N = 3000$ sites and averaging over 1000 realizations of disorder.*

$|V_{11}| \approx 16\pi^2/(N+2)^3$, that is much smaller than $2\bar{\varepsilon} = 1.78$, the energy difference between the lowest band edges (the limit of $N \gg 1$ is implied). In the same way, the magnitude of the coupling of the lowest state of the left sublattice ($k_l = 1$) to the central band states of the right one is about $|V_{1k_r}| \approx 8\pi/(N+2)^2$, whereas the energy spacing at the center of the band is $4\pi/(N+2)$. Again, the coupling is smaller than the energy spacing. This explains the low sensitivity of the states of the subbands to switching on the interaction between the sublattices and therefore, the validity of our simplifications of the model explained in the preceding paragraph.

Our simplified approach explains some of the numerical results of our study. On one hand, the overlapping between the two subbands seems to point out the possibility of an extended phase in the center of the spectrum. Simultaneously this suggests the system may be transparent to the incoming energies where the overlapping occurs which supports our results relative to the transmission coefficient. On the other hand, we can estimate the position of the mobility edges which coincide with the limiting edges of the overlapping region, $\bar{\varepsilon}-2$ and $-\bar{\varepsilon}+2$. Indeed, performing the exact calculations we come to an extended region within $E \in [-1.1, 1.1]$ which is in good agreement with our numerical results.

2.5. Conclusions

Our starting point was a tight-binding model which describes a 1D lattice with long-range correlated diagonal disorder. We diagonalized the Hamiltonian obtaining eigenstates

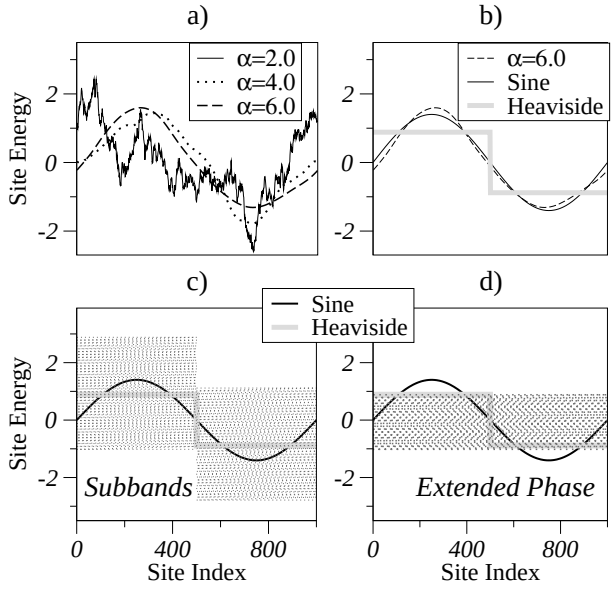

Figure 2.7. *a) Energy landscape for $\sigma = 1$, $\phi_1 = -\pi/2$ and three different values of α. b) Approximated model which replaces the sinusoidal energy landscape by a Heaviside-like one for α large enough. c) Two subbands of allowed eigenstates supported by the Heaviside-like landscape are shown as shadowed bands and d) the central phase where these two subbands overlap giving rise to extended states is presented in a shadow region as well.*

and eigenenergies and we calculated different magnitudes of interest searching for signatures of a localization-delocalization transition at the center of the band. In addition we propose a simple reasoning to explain our numerical results under some approximations.

In light of the results based on the IPR and the transmission coefficient behavior, we proved the existence of an extended phase at the center of the band when $\alpha > \alpha_c \approx 2$ which presents a perfect transmission. Furthermore we performed a phase diagram where the width of the extended phase is estimated. In this sense a slight increase of this width by increasing α over α_c is found. However it saturates for $\alpha > 4$ within the values $[-1, 1]$ in units of the hopping J.

To give an explanation to these results we proposed a simple model based on replacing the disorder distribution Eq. (2.2) with the first and dominant term of its summatory. This is completely justified in the case $\alpha \gg \alpha_c$ since the amplitude of consecutive terms of the sum decreases rapidly as $\sim k^{-\alpha/2}$. After this approximation we argued the possibility

of choosing a proper phase $\phi_1 = -\pi/2$ to have a sinusoidal energy landscape. At this point it seems reasonable to replace this harmonic profile with a Heaviside-like one centered at the middle of the chain. Hereafter we can understand our system like two weakly coupled chains with half of the initial length and uniform site energies of value $\pm\bar{\varepsilon}$ depending on the subchain (see Sec. 2.4). Each of these chains supports an allowed band of states within $[\pm\bar{\varepsilon}-2, \pm\bar{\varepsilon}+2]$ which overlap in the central region of the original band. This leads to the existence of extended states and high transmission properties in this region. Furthermore the mobility edges predicted by this approximated model are in complete agreement with our numerical results based on the IPR and the transmission coefficient behavior.

Chapter 3

Optical absorption in a 1D lattice with scale-free disorder

The linear optical absorption spectrum of a 1D disordered lattice is studied in this chapter. The disorder distribution for the site energies is the one previously studied in Chap. 2 which presents a LDT for a correlation exponent $\alpha > \alpha_c$. As a new anomaly of the model, the unbiased system reveals a double-peaked spectrum when correlations are strong enough. When a bias is applied along the lattice, a competition between disorder and bias effects takes place. We demonstrate that strong correlations, as well as strong bias, enhance the appearance of a periodic pattern in the absorption spectra which we attribute to the Wannier-Stark quantization.

3.1. Introduction

In ordered crystals whose lattices generate a periodic potential, the Bloch theorem predicts uniformly extended states along the whole system [62]. However, if a uniform electrical field is also applied in addition to this periodic potential then, due to the Bragg reflection, all states become localized [63–65]. In such a case, neglecting all kind of scattering effects, the quasiparticle keeps oscillating within a localized lattice region of size $L_B = W/eF$ according to semiclassical arguments. Here $-e$ is the electron charge and W refers to the band width in the unbiased lattice. The oscillation frequency is usually known as Bloch frequency and it is proportional to the applied electric field F as follows $\omega_B = eFa/\hbar$, where a refers to the lattice period which is set to unity hereafter. This periodic motion takes place in real and in k space, and it is known as Bloch oscillations (BOs) [66, 67]. Since scattering processes, due for instance to phonons or defects, destroy the coherence necessary to support BOs, its experimental detection is highly nontrivial. The first BOs were detected in wave packets associated to electrons in semiconducting superlattices [68–74]. Later they were revealed as oscillatory motions of ultracold atoms [75, 76] and Bose-Einstein condensates [77].

On the other hand, since 1998 there exists an enormous interest to study the anomalous localization properties of disordered systems supporting long-range correlations. It is to be noticed that for a large enough correlation exponent of the disorder distribution Eq. (2.2), a phase of extended states at the center of the spectrum arises, see Chap. 2 and references therein. In such a situation, in Ref. [78] the authors established the existence of BOs. This is another reason why long-range correlations in disorder might be interesting from a fundamental point of view. The origin of such oscillations in these systems is the following. As we already said, Bloch states in periodic systems become localized when a bias is applied. Then, it is reasonable to expect a similar effect on the states within the extended phase supported by this kind of disorder. In particular, the mobility edges of the extended phase in the disordered system will behave as the edges of the unperturbed band in the ordered one. Therefore, if the extended phase width is called W^*, BOs within a region of size $L_B = W^*/eF$ are expected to occur [78].

In this chapter we will gain an insight into the finding of BOs for this type of disordered systems considering its counterpart effect in the frequency domain. This is known as the Wannier-Stark ladder (WSL) [79, 80] and consists of a discretization of the spectrum

in equidistant quasistationary energy levels due to the bias effect. The energy spacing between consecutive levels is $\Delta E = \hbar\omega_B = eFa$. The WSL has been clearly observed in photoluminescence [81, 82] and photoconductivity spectra [83] of semiconducting superlattices and might arise also in optical absorption spectra.

In this sense the magnitude of interest in this chapter is the linear optical absorption coefficient of a biased Frenkel chain. We claim that disordered systems generated under the disorder distribution Eq. (2.2) presents a periodic pattern in its absorption spectra as soon as the applied bias is large enough. The intensity of the correlations also enhances the appearance of the WSL structure. Then we provide new evidences of the existence of BOs in disordered lattices with long-range correlations [78] by way of the study of its counterpart effect in the energy domain.

3.2. Hamiltonian description

A 1D Frenkel system with uniform spacing set to unity is described by means of a tight-binding Hamiltonian. Disordered site energies and uniform nearest-neighbor coupling along the chain are considered. Hereafter the latter will be used as the energy unit of the problem $|J| = 1$. The Hamiltonian to describe the eigenstates of a quasiparticle in such a lattice under the effect of an electrical bias $U = eFa$ is the following:

$$\mathcal{H} = \sum_{n=1}^{N} \left[\mathcal{E}_n - U\left(n - \frac{N}{2}\right) \right] |n\rangle\langle n| - \sum_{n=1}^{N-1} \Big(|n\rangle\langle n+1| + |n+1\rangle\langle n| \Big) , \tag{3.1}$$

where $|n\rangle$ is the ket vector of the state in which the nth molecule is excited and the rest are in the ground state. The on-site energy of the nth molecule is $\mathcal{E}_n = \bar{\mathcal{E}} + \varepsilon_n$. For the sake of simplicity $\bar{\mathcal{E}} = 0$ and the number of sites in the lattice N is assumed to be even. We introduce a stochastic contribution in these energies according to the distribution Eq. (2.2). For further details about this distribution see Sec.2.2. The linear potential created by the applied bias is defined by the new term $-U(n - N/2)$ introduced as an on-site contribution. This bias may be due to an internal or external uniform electrical field.

The magnitude of interest in this chapter is the linear optical absorption spectrum (OAS) which is defined as in Ref [84]:

$$A(E) = \frac{1}{N} \left\langle \sum_{\nu=1}^{N} \left(\sum_{n=1}^{N} \psi_{\nu n} \right)^2 \delta(E - E_\nu) \right\rangle , \tag{3.2}$$

where ν and n label the eigenstate and the site index respectively and E_ν and $\psi_{\nu n}$ are the eigenenergies and eigenstates resulting from the diagonalization of the Hamiltonian Eq. (3.1) under rigid boundary conditions.

Another relevant parameter when dealing with optical transitions is the dimensionless oscillator strength of the state ν, $f_\nu = \left(\sum_{n=1}^{N} \psi_{\nu n}\right)^2$, which provides the contribution to the optical absorption spectrum of the state ν.

In order to get into the characteristics of the model, first of all we study the simplest situation: $\alpha = 0$ and $U = 0$. In such a case there is no bias applied to the uncorrelated system. Therefore, it is well known that disorder results in the localization of all the states [33] and in the appearance of Lifshits tails in the density of states (DOS) outside the bare quasi-particle band which ranges from $E = -2$ to $E = 2$ [85, 86].

On the other hand, because of considering a negative hopping, the optically relevant states are those at the bottom of the band. Their importance arises from their bell-like amplitudes of probability within their localization length which do not present any significative node along it. For this reason, their oscillator strength, as well as their contribution to the optical coefficient, will be larger than those of the states of higher energies which present indeed more nodes, the so-called dark states [85, 86]. While the width of these wells N^* is related to the eigenstates localization length, the magnitude $\sigma/\sqrt{N^*}$ determines the absorption line width. This latter effect is usually known as exchange narrowing effect [84–88]. The position of this line is known to be slightly below the bottom of the unperturbed band $E = -2$ and its width is also well defined, see Ref. [84]. In Ref. [87] the localization length of the optically dominant states N^* and the width of the absorption line were estimated as a function of the degree of disorder as:

$$N^* = \left(\frac{3\pi^2}{\sigma}\right)^{2/3} , \tag{3.3a}$$

$$\sigma^* = \frac{2\sigma}{\sqrt{N^*}} = 6\pi^2 \left(\frac{\sigma}{3\pi^2}\right)^{4/3} . \tag{3.3b}$$

It is worth mentioning that both short-range and power-law long-range correlations in disorder enhance the localization of the eigenstates of the system and subsequently, they give rise to broadener absorption lines [60, 61].

3.3. Optical absorption in an unbiased system

Once the absorption spectrum in the absence of correlations and electrical bias has been discussed, the study of the correlations effects is in order. Keeping in mind that the model reveals different localization properties for $\alpha > \alpha_c$ or $\alpha < \alpha_c \approx 2$, hereafter two representative values for the correlation exponent, $\alpha = 1$ and $\alpha = 4$, will be considered. We refer to them as weakly and strongly correlated limits.

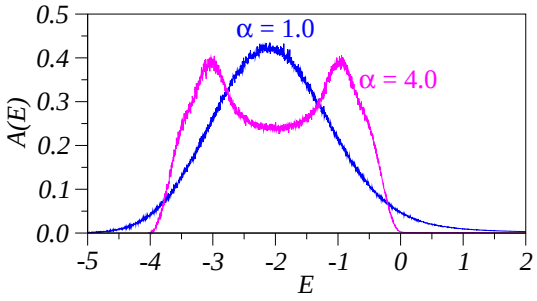

Figure 3.1. *Absorption spectrum for chains of $N = 500$ sites under no applied bias ($U = 0$). Results for the two representative correlation exponents, $\alpha = 1$ and $\alpha = 4$ are shown. In both cases a magnitude of disorder $\sigma = 1$ and an average over 3×10^4 realizations were considered.*

Figure 3.1 shows the optical absorption coefficient of a system of $N = 500$ sites calculated averaging over 3×10^4 realizations of disorder and considering $U = 0$ and $\sigma = 1$. In the weakly correlated case a single absorption line, which is asymmetric and inhomogeneously broadened, arises. Drawing an analogy between this case and the one discussed in the previous section for $\alpha = 0$, this line is situated below the edge $E = -2$ and its width is $\sigma^* \approx 2.2$. This width is approximately three times larger than in the uncorrelated model, Eq. (3.3b). This tendency is in full accordance with what we mentioned in the preceding section. On the contrary the spectrum turns to be double-peaked in the strongly correlated situation, $\alpha = 4$. Both peaks arise from states with large oscillator strength not only at the bottom of the band, but also well inside it.

In order to explain this double-peaked spectrum it is very useful to recall the qualitative explanation proposed in Sec. 2.4 for chains where $\alpha \gg \alpha_c \approx 2$. Under those approximations we come to a simplified system consistent in two weakly coupled subchains with $N/2$ sites. The site energy of these chains is uniform along them and their values are $+\bar{\varepsilon}$ and $-\bar{\varepsilon}$. We

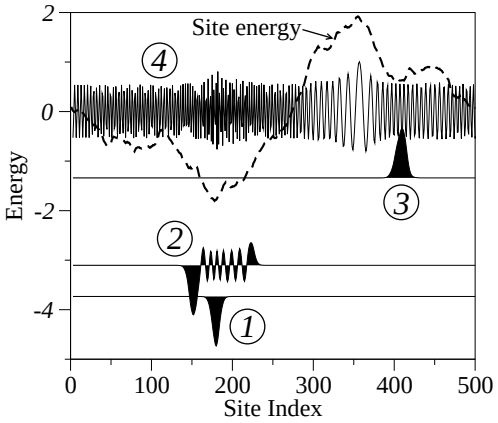

Figure 3.2. *A subset of eigenstates for a typical realization of the random energy potential (dashed line), for a chain of size $N = 500$, magnitude of disorder $\sigma = 1$, and correlation exponent $\alpha = 3$ (larger than the critical value $\alpha_c = 2$). The baselines indicate the energies of each eigenstate. The states 1 and 3 are those which contribute to the low- and high-energy peaks of the absorption spectrum, respectively.*

argue that every subchain gives rise to an allowed band within the range $[\pm\bar{\varepsilon} - 2, \pm\bar{\varepsilon} + 2]$. This explains the existence of an extended phase in the energy region where these two subbands overlap. In particular, this region coincides with the central part of the initial spectrum. Concerning the current topic we are dealing with, the absorption spectrum, this qualitative picture should be taken into account again. It is well established that for a uniform chain the states at the bottom of the band present high oscillator strength and thus, high contribution to the optical absorption (see Ref. [84]). Therefore if our system behaves as one consistent of two uniform subchains, it seems reasonable to think that both of them will present optically active states at the bottom of their bands, $\bar{\varepsilon} - 2$ and $-\bar{\varepsilon} - 2$, see Fig. 3.2. As a result of such states the spectrum becomes double-peaked. Performing the exact calculation of these band edges we find $\bar{\varepsilon} - 2 = -1.11$ and $-\bar{\varepsilon} - 2 = -2.89$ which are in perfect agreement with the position of the absorption lines. Taking into account this finding, the mobility edges may be experimentally detected by means of optical absorption spectroscopy, since one of them coincides with the higher energy line of the spectrum.

3.4. Optical absorption in a biased system

3.4.1. Previous considerations

In the introduction of this chapter it was already mentioned that a uniform electrical field applied to an ordered system localizes all eigenstates within a localization length depending on the magnitude of the field as $L_B = W/eF$, in our units $L_B = 4/U$. The numerator of this equation is the allowed band width in units of the hopping. The effect on the level structure was also reported, claiming that it turns out to be a ladder-like spectrum. The level spacing is uniform and coincides with U in an infinite system [79]. Considering now the disordered case, we should take into account that disorder broadens the absorption peaks. For this reason both, the absorption line width σ_B and the separation between peaks U, must be considered to predict whether we will have enough resolution to observe the WSL in the spectrum.

The first step is to use the same reasoning as in Sec. 3.2 about the exchange narrowing effect (see Refs. [84–88]). Thus, if the quasiparticle is localized within a region L_B due to the bias effect, then it will be affected by a reduced disorder $\sigma/\sqrt{L_B}$. According to Eq. (3.3b) we can estimate the broadening of the WSL levels as

$$\sigma_B = \frac{2\sigma}{\sqrt{L_B}} = \sigma\sqrt{U} \ . \tag{3.4}$$

Under these considerations the WSL may be resolved as long as the level broadening σ_B is smaller than the level spacing U. This reasoning leads to the following condition in our particular case:

$$\sigma < \sqrt{U} \ . \tag{3.5}$$

Those situations where the inequality Eq. (3.5) is fulfilled will be referred as the strong bias limit. Otherwise we will be dealing with the weak bias case.

3.4.2. Weak bias

In the weak bias limit, the absorption spectrum is calculated for systems of $N = 100$ sites under the effect of a bias $U = 0.01$. The site energies are generated with a magnitude of disorder $\sigma = 1$, 10^6 realizations of disorder and two correlation exponents are considered for the weakly and the strongly correlated cases, $\alpha = 1$ and $\alpha = 4$.

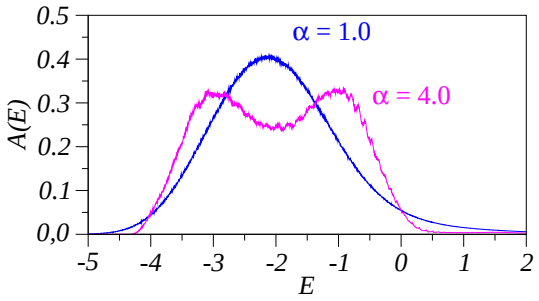

Figure 3.3. *Absorption spectra for chains with* $N = 100$ *sites under an applied bias* $U = 0.01$. *The calculations are performed for two correlation exponents* $\alpha = 1$ *and* $\alpha = 4$. *In both cases the magnitude of disorder is* $\sigma = 1$ *and the number of averages is* 10^6.

Being considered the weak bias limit $\sigma \gg \sqrt{U}$, the WSL is not resolved (see Fig. 3.3). Due to the chosen parameters, the potential drop along the whole system is $UN = 1$, smaller than the line width in the unbiased system ($\sigma^* \approx 2.2$, see Sec. 3.3). The main feature of these spectra is that the effect of the bias is weak, leading only to an unnoticeable broadening of the spectra and smoothing the shape of the doublet (at $\alpha = 4$) as compared to the bias-free conditions (compare to Fig. 3.1).

As a further step the absorption spectrum for the same set of parameters of Fig. 3.3 but a higher bias $U = 0.1$ is calculated.

In this situation the potential drop along the system due to the bias is $UN = 10$ which is larger than the line width for the unbiased system, producing a transformation of the spectra (see Fig. 3.4). These spectra are defined by the effect of the bias and not by the disorder anymore. Thus, they present a well defined plateau in the central part whose width coincides with the potential drop along the system ≈ 10. Since the bias is the dominant parameter, there is no relevant difference between the spectra calculated for weak and strong correlations. This is consistent with the fact that disorder and its relative parameters are not significative for weak fields.

3.4.3. Moderate bias

As it was already mentioned, the WSL is expected to be resolved in the strong bias limit, however in this section we demonstrate that for the case of moderate bias the WSL

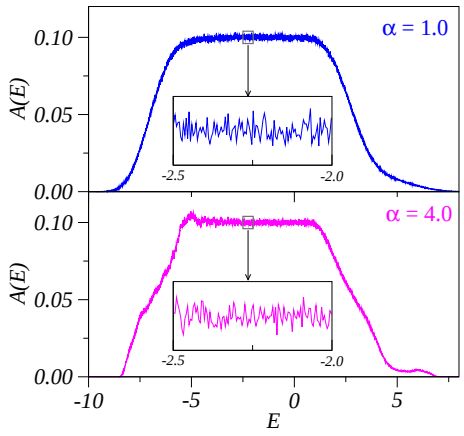

Figure 3.4. *Absorption spectra for chains with $N = 100$ sites under an applied bias $U = 0.1$. The calculations are performed for two correlation exponents $\alpha = 1$ and $\alpha = 4$. In both cases the magnitude of disorder is $\sigma = 1$ and the number of averages is 10^6. Insets show enlarged views of the absorption spectra.*

can arise provided the correlations are strong enough. Figure. 3.5 shows the absorption spectra for the same set of parameters as before but with an even higher bias, $U = 0.5$.

For weak correlations, $\alpha = 1 < \alpha_c = 2$, the WSL is not resolved according to the condition Eq. (3.5) deduced in Sec. 3.4.1, which is not fulfilled with this set of parameters. However, for strong correlations, $\alpha = 4 > \alpha_c = 2$, the spectrum gives rise to a clearly periodic pattern with period $U = 0.5$. The same structure is revealed by studying the oscillator strength f_ν as a function of the energy level E_ν, left panel of Fig. 3.6.

In view of these results we claim that this pattern corresponds to the Wannier Stark ladder. We have also proven that the period of the periodic pattern does not depend on the size of the system, meaning that it is not a finite-size effect. In this regard the right panel of Fig. 3.6 shows the absorption spectra for the same set of parameters that in Fig. 3.5 but a different size of the system.

It is to be noticed that for $U = 0.5$ the WSL is not expected to be resolved according to the condition Eq. (3.5). The disorder distribution Eq. (2.2) should be analyzed in more detail to understand this effect. In particular, for the strongly correlated limit $\alpha = 4$, this distribution can be approximated for its first and dominant term, see Sec. 2.4. This implies that the magnitude of the actual disorder is at least a factor of $2^{-\alpha/2}$ smaller than the bare value σ. Therefore, strong correlations facilitate the condition Eq. (3.5) to be

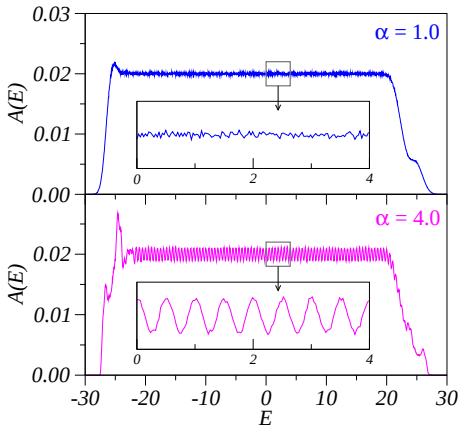

Figure 3.5. *Same as in Fig. 3.4 but considering a stronger bias $U = 0.5$. The WSL is observed for $\alpha = 4$.*

fulfilled: by reducing σ the WSL will be resolved at lower bias.

3.4.4. Strong bias

Finally, we study the absorption spectra using a set of parameters to enhance the WSL observation even when the most weakly correlated case $\alpha = 0$ is considered: $\sigma = 0.2$ y $U = 0.1$. The resulting optical absorption spectra are shown in Fig. 3.7 for correlation exponents $\alpha = 0$ and $\alpha = 5$. In the upper panel the spectrum for $\alpha = 0$ is shown. In the central part the WSL arises as a set of equidistant peaks with period $U = 0.1$. For the strongly correlated case, $\alpha = 5$ (lower panel) every single peak of the upper level transforms in a double peak. Nevertheless the periodic pattern with period $U = 0.1$ remains. The origin of this splitting is the same that the one mentioned in Sec. 3.3. Then, the anomalous behavior of the absorption spectrum due to the particular correlated disorder distribution Eq. (2.2) occurs even in the strong bias limit.

Regarding the irregular edges of the spectrum our claim is that they are a consequence of finite-size effects. These effects are more relevant for states localized in regions close to the lattice edges whose properties are quite different from those of the center of the band.

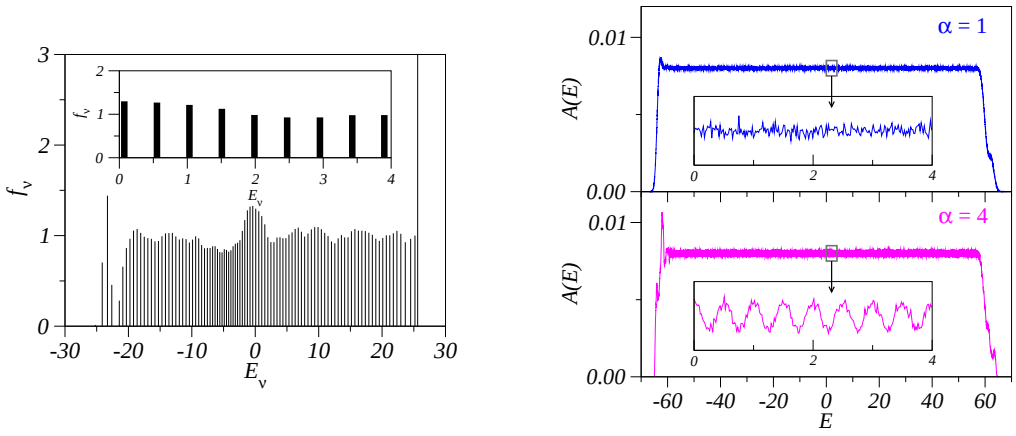

Figure 3.6. *Left panel shows the oscillator strength distribution as a function of energy. This calculation is performed with the same set of parameters of Fig. 3.5 and* $\alpha = 4$*. Right panel shows the same as in Fig. 3.5 but for a larger system of* $N = 250$ *sites.*

3.5. Conclusions

In this chapter the linear optical absorption spectrum in a 1D disordered lattice is studied. The disorder distribution for the site energies is long-range correlated and its power spectrum has the form $1/k^{\alpha}$.

The starting point is the simplest case, the unbiased system. The spectrum reveals itself as single-peaked for the weakly correlated limit $\alpha < \alpha_c = 2$. This peak is situated slightly below the band bottom of the uncorrelated system and splits by considering stronger correlations $\alpha > \alpha_c = 2$. Notice that this effect is an interesting peculiarity of the disorder distribution.

By applying a weak or a moderate bias along the system, the properties of the spectra depend on the competition between bias and disorder effects. Thus, there is a significative transformation of the spectra only if the potential drop along the system UN is larger than the spectrum line width in the unbiased system. In such a case, the spectra present a wide central plateau of width UN not depending on the correlation exponent since the disorder effects are not relevant for moderate bias.

Considering a strong enough bias to fulfill the condition $\sigma < \sqrt{U}$ (see Sec. 3.4.1), periodic patterns with period U in the optical absorption spectrum are expected. We claim that this effect is related to the Wannier-Stark level quantization of the spectrum

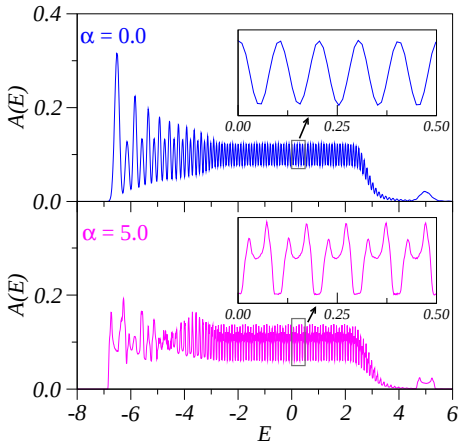

Figure 3.7. *Same as in Fig. 3.4 but considering* $\sigma = 0.2$ *and correlation exponents* $\alpha = 0$ *and* $\alpha = 5$*. Insets show enlarged views of the absorption spectra.*

produced by the applied bias. We demonstrated that this behavior does not depend on the system size and therefore, it is not related to finite-size effects.

Due to the anomalous characteristics of the disorder distribution, the correlations seem to enhance the Wannier-Stark ladder resolution. Moreover, the splitting of the single peak studied in the unbiased system for $\alpha > \alpha_c = 2$ (see Sec. 3.3), arises as well in the periodic spectra for strong biased lattices.

It is interesting to remark that the modeled bias can be external or internal to the system. Then our predictions may be applied to electrons moving in the conduction band of a 1D disordered chain [89] as well as to Frenkel excitons, where the field is intrinsic due to the particular properties of the system like in dendrimers (see Ref. [90]).

Chapter 4

Fluorescence decay in a 1D lattice with scale-free disorder

We investigate transport properties of a 1D disordered system by analyzing the survival probability of an initially created excitation. The disorder distribution under consideration was studied in the preceding chapters and it presents long-range correlations. The dynamics of the intraband excitonic relaxation is monitored by the fluorescence decay calculated after broadband pulse excitation by way of the Pauli master equation. An exponential fluorescence decay arises when considering the case of strongly long-range correlated disorder which in previous chapters has revealed to be a limiting situation giving rise to anomalous properties.

4.1. Introduction

Transport properties of disordered systems have received a lot of attention from a fundamental and also from an applied point of view [91, 92]. Indeed it can be considered in different and complementary ways, namely in the coherent [93] or incoherent [94] regimes. Generally speaking conclusions about this topic arise from studies of localization properties or spectroscopy on one hand, but they can also be established by means of the analysis of the distribution and the dynamics of excited states. In this sense, the magnitude of interest in this chapter will be the fluorescence decay, which is directly accessible through optical experiments [95]. The fluorescence gives a measurement of the survival probability of the initial excitation in any of the eigenstates of the system before decaying by radiative channels. In most works substitutional or interstitial traps were included in the lattice to quench the excitation [96–98] and different theoretical approaches have been proposed to simulate its time-evolution. For instance random walks theories [99, 100], imaginary non-Hermitian Hamiltonians [98,101] or Pauli master equations [102,103] have been used to gain an insight into this topic. Also different disorder distributions for the traps position [101, 102, 104] and for the transition energies of the molecules conforming the lattice [96, 105, 106] have been considered. The most relevant and widely accepted conclusion is that the general asymptotic behavior at very long times of the survival probability fits a stretched exponential of the form $I(t) \sim \exp\left[-(t/\tau_\infty)^\beta\right]$, where both τ_∞ and $\beta < 1$ depend on the particular characteristics of the disordered system under consideration [97, 102].

As a further step in this matter, we propose the study of the survival probability under the definition of Ref. [102] in a system with long-range correlated diagonal disorder. We will use the disorder distribution Eq. (2.2) proposed in Ref. [50] keeping in mind its main peculiarities: the appearance of an extended phase at the center of the band considering high correlations, see Chap. 2, as well as the splitting of the single peaked absorption spectrum, see Chap. 3. Moreover, this model might support Bloch oscillations [78] for a large enough correlation exponent in the strong bias limit. This can be tested in the frequency domain by way of the study of the WSL in the absorption spectrum, see Chap. 3.

The main difference with previous studies about this topic is that in these correlated systems, the role of the additional traps is played by their unusual states at the center of the band which present high oscillator strength, see Sec. 3.3. Then, the excitation of the

system will be quenched by radiative processes which take place due to the high coupling to the light of these states. Our main goal in this chapter is to study the fluorescence decay in this kind of systems considering two representative situations, highly correlated and weakly correlated disorder, under a master equation approach. Thus, we will try to establish a relationship with previous results concerning the absorption spectrum and provide new experimental procedures to support the existence of the WSL in the spectrum of this kind of systems when a bias is applied.

4.2. Model description

4.2.1. Tight-binding Hamiltonian

As in previous chapters we consider a tight binding Hamiltonian to describe a 1D disordered lattice of N sites, assuming N to be even. Biased systems are under consideration so we use the Hamiltonian described in Sec. 3.2:

$$\mathcal{H} = \sum_{n=1}^{N} \left[\mathcal{E}_n - U \left(n - \frac{N}{2} \right) \right] |n\rangle\langle n| - \sum_{n=1}^{N-1} \left(|n\rangle\langle n+1| + |n+1\rangle\langle n| \right) , \tag{4.1}$$

considering a long-range correlated disorder distribution for the site energies $\mathcal{E}_n = \bar{\mathcal{E}} + \varepsilon_n$, assuming $\bar{\mathcal{E}} = 0$ hereafter for simplicity (see Sec. 2.2 for further details) and:

$$\varepsilon_n = \sigma C_\alpha \sum_{k=1}^{N/2} \frac{1}{k^{\alpha/2}} \cos\left(\frac{2\pi k n}{N} + \phi_k \right) . \tag{4.2}$$

As we already mentioned the Hamiltonian Eq. (4.1) with this disorder distribution supports a phase of extended states at the center of the band among other interesting peculiarities for strongly correlated systems, see previous chapters for details. On the contrary all the states are localized in the weakly correlated limit.

4.2.2. Pauli master equation

In disordered systems exciton levels are usually localized. Hopping between them may involve a loss or a gain of energy which is exchanged with the host medium by means of phonons. For this reason, this kind of hopping is usually known as incoherent hopping. In this sense, two important assumptions to simplify our study will be considered hereafter:

the exciton-vibration coupling is weak not considering polaron effects and only one-phonon processes are assumed.

According to Ref. [107] the transition rate from the state ψ_μ (with energy E_μ) to the state ψ_ν (with energy E_ν) is defined as following:

$$W_{\mu\nu} = W_0\, S(|\Delta E_{\mu\nu}|)\, F(\Delta E_{\mu\nu}, T)\, \mathcal{I}_{\mu\nu}\ , \tag{4.3}$$

with $\Delta E_{\mu\nu} \equiv E_\mu - E_\nu$. The constant W_0 characterizes the amplitude of transitions. A spectral density function of the form $S(|\Delta E|) = |\Delta E|/J$ holds for glassy hosts [107, 108]. Temperature T enters into this expression through the function $F(\Delta E, T) = \theta(\Delta E) + n(\Delta E, T)$, where θ is the Heaviside step function and $n(\Delta E, T) = [\exp(|\Delta E|/k_B T) - 1]^{-1}$ is the occupation number of the vibration mode with frequency $\Delta E/\hbar$. The parameter

$$\mathcal{I}_{\mu\nu} \equiv \sum_{n=1}^{N} \psi_{\mu n}^2 \psi_{\nu n}^2 \tag{4.4}$$

represents the overlap integral of exciton probabilities for the states ψ_μ and ψ_ν. The principle of detailed balance is fulfilled by these transition rates: $W_{\nu\mu} = W_{\mu\nu} \exp(-\Delta E_{\mu\nu}/k_B T)$.

We describe the process of exciton relaxation by means of the Pauli master equation for the level population P_μ of the μ th exciton eigenstate

$$\frac{dP_\mu}{dt} = -\gamma_\mu P_\mu + \sum_{\nu=1}^{N} (W_{\nu\mu}\, P_\nu - W_{\mu\nu}\, P_\mu)\ , \tag{4.5}$$

where $\gamma_\mu = \gamma\, f_\mu$ is the spontaneous emission rate of the μ th exciton state, while γ is that of a monomer, $f_\mu = (\sum_{n=1}^{N} \psi_{\mu n})^2$ being the dimensionless oscillator strength. After broadband pulse excitation, each level is populated according to its oscillator strength, namely $P_\mu(0) = f_\mu/N$. Consequently, the initial total population is normalized to one $\sum_\mu P_\mu(0) = 1$. The normalized fluorescence after pulse excitation is then obtained from

$$I(t) = N\, \frac{\sum_{\mu=1}^{N} f_\mu P_\mu(t)}{\sum_{\mu=1}^{N} f_\mu^2}\ , \tag{4.6}$$

which is the magnitude of interest in this chapter.

4.3. Fluorescence decay in unbiased systems

In order to get familiar with the fluorescence decay in our model we start explaining the unbiased system. Under rigid boundary conditions we diagonalized the Hamiltonian

Eq. (4.1) to obtain the eigenenergies and eigenstates to monitor the evolution of the fluorescence Eq. (4.6). As we already did in previous chapters we make calculations for different values of the correlation exponent α.

Hereafter we restrict ourselves to $T = 0$, although we have checked that our main conclusions are valid when the temperature is a fraction of J/k_B. For instance, in J-aggregates of cyanine dyes I $J \approx 0.05\,\mathrm{eV}$ [26], this means that our results would be relevant for a wide range of temperatures below $J/k_B \approx 600\,\mathrm{K}$. We also choose the parameter $W_0 = \gamma$, so that radiative decay is favored with respect to intraband relaxation. This statement can be understood from previous estimations in unbiased lattices with uncorrelated disorder [103]. When $\sigma = 1$, the largest intraband transition rate $W_{\mu\nu}$ is of the order $\sim 0.06W_0$ but the highest spontaneous emission rate γ_μ is about $\sim 9\gamma$.

Figure. 4.1 presents the fluorescence decay after an initial broadband excitation. The time scale is set to γt hereafter. The lattice size is $N = 250$ and the results comprises the average over 200 realizations of the disorder. Looking at the logarithm axis for the fluorescence we can conclude that in none of the considered cases the decay is exponential. However, at large times, the fluorescence can be fitted by a stretched exponential $I(t) \sim \exp\left[-(t/\tau_\infty)^\beta\right]$, where both τ_∞ and $\beta < 1$ depend on the correlation exponent α. It is to be stressed that the fluorescence decay of weakly correlated systems is significantly faster than in the strongly correlated ones. The different fluorescence decay rates can be understood

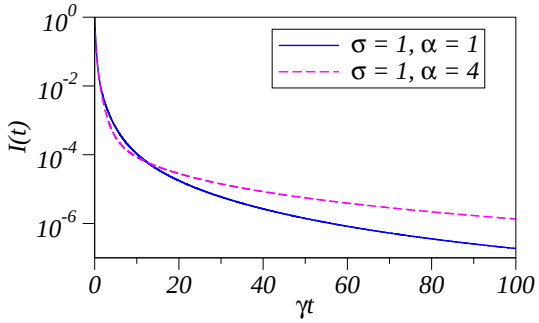

Figure 4.1. *Time dependence of the fluorescence decay after pulse excitation in weakly ($\alpha = 1$) and strongly ($\alpha = 4$) correlated 1D lattices when $U = 0$ for a magnitude of disorder $\sigma = 1$. Lattice size is $N = 250$ and the results comprise the average over* 200 *realizations of the disorder.*

keeping in mind the amplitude of probabilities of the eigenstates, see Fig. 4.2. When

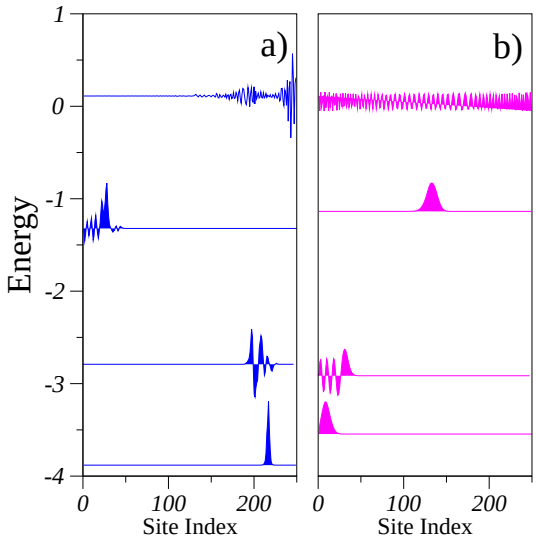

Figure 4.2. *A subset of eigenstates for a typical realization of the random energy potential for a lattice of size* $N = 250$*, magnitude of disorder* $\sigma = 1$*, and correlation exponents a)* $\alpha = 1$ *and b)* $\alpha = 4$*. The baseline indicates the energy of the eigenstate.*

$\alpha < \alpha_c$, all states are localized and the higher the eigenenergy is, the smaller oscillator strength of the eigenstate is. Therefore, higher energy states are weakly coupled to the light and their populations after the initial excitation will be scarce. These states will be referred to as dark states hereafter. Indeed, the excitation gets soon stuck at the bottom state and the exciton emits a photon on average after a time $1/\gamma$ has elapsed. On the contrary, when $\alpha \gg \alpha_c$, high energy states can be excited by the initial excitation due to the anomalous states with large oscillator strength at the center of the band around $E = -1$. This kind of states do not decay radiatively because it exists a non-zero probability of hopping between them and other lower energy dark states. This means that the excitation is transferred through these states down to reach the ones at the bottom of the band when a photon is emitted. Consequently, on average there are more intraband scattering events through dark states when α is large and this entails a longer fluorescence decay time as observed in Fig. 4.1.

4.4. Fluorescence decay in biased systems

4.4.1. Objectives

The bias effect on the energy levels, the WSL [79] was analyzed in Chap. 3. It was mentioned that the eigenstates turn out to be localized in a region of size $L_B = 4/U$ in units of the lattice period (see Sec. 3.4.1). It is convenient to review the main conclusions of that chapter before going into the fluorescence analysis. Generally speaking the most important fact is that long-range correlations facilitate the occurrence of the WSL even if the magnitude of disorder is large. In this case, a periodic pattern is found to build up at the center of the optical absorption band. Its period is equal to U, as for the WSL in an ideal lattice, and independent of the system size N. This pattern was attributed to the Wannier-Stark quantization of the energy spectrum in the long-range correlated disordered lattice.

Once the existence of the WSL in this kind of disordered systems was proved, our goal now is to establish a relationship between the anomalous optical spectra shown in Chap. 3 and the fluorescence decay behavior. This would open another experimental possibility to determine if this model of disorder supports the WSL. For this reason we compare the absorption and fluorescence spectra in the most characteristic cases.

4.4.2. Main results

In Fig. 4.3 the absorption spectra (see Sec. 3.2) calculated for chains of $N = 250$ sites is plotted. The magnitude of disorder is $\sigma = 1$ and the bias magnitude is $U = 0.05$. Averages over 10^6 realizations of disorder were performed in Eq. (3.2). Two values of the correlation exponents are considered, $\alpha = 1$ and $\alpha = 4$. The spectra broaden as compared to those of the unbiased systems (not shown in the figure, see Fig. 3.1 for completeness) but they are still featureless and no signatures of the WSL are detected. The corresponding fluorescence decay is shown in Fig. 4.3, where we observe that the decay is non-exponential. At large time the decay is slower on increasing the magnitude of the correlations, similarly to what was found in the absence of bias, see Fig. 4.1.

In Fig. 4.4 we plot the absorption spectra calculated for a higher value of the bias $U = 0.5$ and same set of parameters than in Fig. 4.3. As we explained in Sec. 3.4.4 in the case of $\alpha < \alpha_c$, the spectrum remains structureless, while for strong correlations,

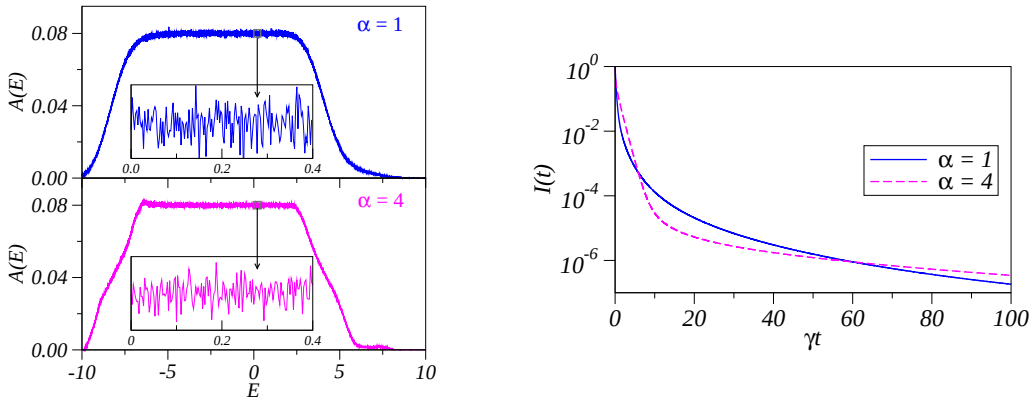

Figure 4.3. *Absorption spectra (left) and time-dependence of the fluorescence decay (right) of biased chains ($U = 0.05$) with $N = 250$ sites calculated for two values of the correlation exponent α, shown in the plot. The magnitude of disorder is $\sigma = 1$. Every absorption spectrum and fluorescence decay curve was obtained after averaging over 10^6 and 200 realizations of disorder respectively. Insets show enlarged views of the absorption spectra.*

$\alpha > \alpha_c$, it presents a periodic pattern shown in detail in the inset of the lower panel. Most important, the period of the modulation is exactly equal to $U = 0.5$, as results from the occurrence of the WSL in the energy spectrum of the system.

Looking at the right panel of Fig. 4.4 we present evidences that long-range correlations also have a remarkable impact on the fluorescence decay. In particular it turns out to be still non-exponential when $\alpha < \alpha_c$, while the decay is exponential in the opposite limit, when $\alpha > \alpha_c$. Moreover we checked that this new exponential fluorescence decay is a real consequence of the considered disorder model and not a finite-size effect. In Fig. 4.4, it is observed that the fluorescence decay behavior does not depend on the lattice size N. In view of these results, we claim that the existence of the WSL in the optical spectrum is associated to an exponential fluorescence decay. Thus, we propose two related methods to elucidate if the disorder distribution Eq. (2.2) can support the WSL.

For completeness we study how the fluorescence behaves in a last case for which the bias is strong enough to resolve the WSL even in a weakly correlated system, see Sec. 3.4.4. As before we calculate the absorption spectrum and the fluorescence decay for the same set of parameters but for a smaller magnitude of disorder $\sigma = 0.2$ in order that the Eq. (3.5) is fulfilled for any strength of the correlations.

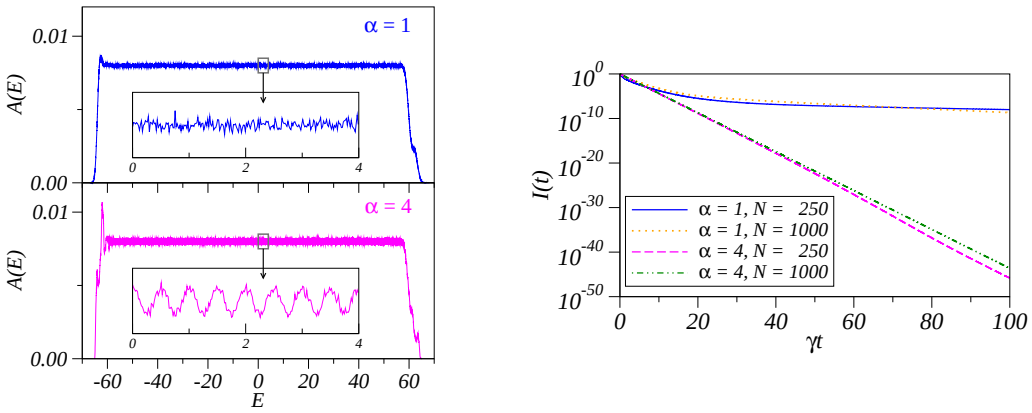

Figure 4.4. *Same as in Fig. 4.3 but considering a stronger bias $U = 0.5$. The right panel shows the time-dependence of the fluorescence decay for two different system sizes.*

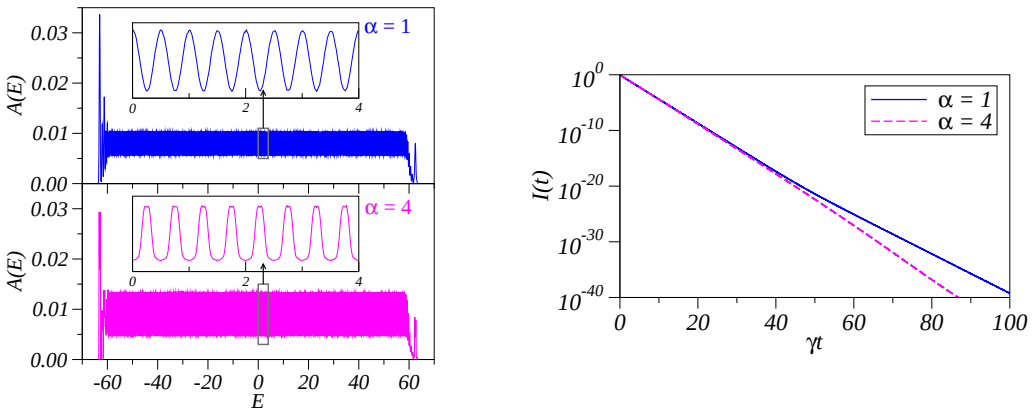

Figure 4.5. *Same as in Fig. 4.3 but considering a stronger bias $U = 0.5$ and a weaker magnitude of disorder $\sigma = 0.2$.*

In Fig. 4.5 it is observed that a periodic pattern with period U arises considering weak and strong correlations. In the same way, an exponential fluorescence decay is observed for both limits.

4.5. Qualitative picture

Results shown in Figs. 4.4 and 4.5 provide compelling evidences that the occurrence of the WSL in the energy spectrum may result in an exponential decay of the fluorescence. In the left panel of Fig. 4.4 we observed no WSL signatures in the optical absorption spectrum when $\alpha < \alpha_c$ and the magnitude of disorder σ is large. Simultaneously, the fluorescence decay is non-exponential for this set of parameters, as shown in the right panel of Fig. 4.4. This behavior, as well as such situations which support the WSL pattern, can be explained by the following reasoning. When σ is large and correlations are weak ($\alpha < \alpha_c$) the oscillator strength depends on the energy state, similarly to what is found in the absence of bias (see Sec. 4.3). This finally leads to a non-exponential decay of the fluorescence. However, when correlations are strong, $\alpha > \alpha_c$, or the magnitude of disorder σ is smaller than $\sqrt{U}$, the occurrence of the WSL ladder is accompanied by an exponential decay of the fluorescence, as shown in the right panel of Fig. 4.4. In this case localization by the bias U prevails over that produced by disorder effects. When the WSL arises, the shape of the eigenfunction is almost the same for all states, except for a trivial space shift and excluding finite-size effects (see Fig. 4.6). Consequently, the oscillator strength of all states has the same value, yielding a single exponential in the decay law of the fluorescence.

4.6. Finite-size effects

In the current and the previous chapters the existence of the WSL structure in the optical absorption spectrum, as well as the exponential behavior for the fluorescence decay in strongly correlated disordered systems generated according to Eq. (2.2), were demonstrated not to depend on the system size. This means that these peculiar properties of such a disorder distribution are not a consequence of finite-size effects. In this section we provide new evidences for this claim respect to the topic we are dealing with in this chapter, the time-dependence of the fluorescence decay.

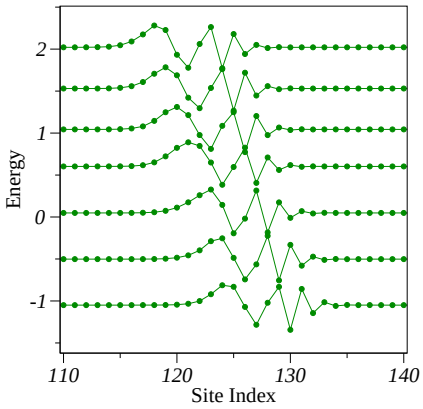

Figure 4.6. *A subset of eigenstates for a typical realization of the random energy potential when* $U = 0.5$ *for a lattice of size* $N = 250$*, magnitude of disorder* $\sigma = 0.2$*, and correlation exponent* $\alpha = 1$*. The baseline indicates the energy of the eigenstate.*

Firstly it is worth noticing that the peculiarities observed at the low- and high-energy sides of the absorption spectra shown in Figs. 4.4 and 4.5 are associated with finite-size effects as it was already mentioned in Sec. 3.4.4. The energy levels of the spectrum edges are formed by the states localized close to the system ends. Therefore, the corresponding eigenfunctions differ from those at the band center. As a consequence, not all eigenstates present exactly the same value of the oscillator strength and a slight deviation from the single exponential decay of the fluorescence can be detected.

We propose an analysis to establish the relevance of these deviations taking as the starting point the biased disorder-free lattice which is well described theoretically [109]. In such a case, the normalized eigenstates of the Hamiltonian Eq.(4.1) can be expressed in terms of the Bessel functions as $\psi_{\mu n} = J_{n-\mu}(2J/U)$ in the thermodynamic limit ($N \to \infty$). The corresponding eigenenergies are $E_\mu = \mu U$, μ being an integer (i.e. the WSL structure). The oscillator strength can also be calculated exactly in this limiting case as $f_\mu = 1$, which takes the same value for all states, as expected. Remarkably, the oscillator strength becomes also independent of the bias U in large disorder-free systems. From Eq. (4.6) we conclude that the normalized fluorescence intensity is nothing but the survival probability $I(t) = \sum_{\mu=1}^{N} P_\mu(t)$ in this case. Summing over all states in Eq. (4.5) we obtain $\dot{I}(t) = -\gamma I(t)$, leading to $I(t) = \exp(-\gamma t)$. Consequently, the fluorescence decay in biased

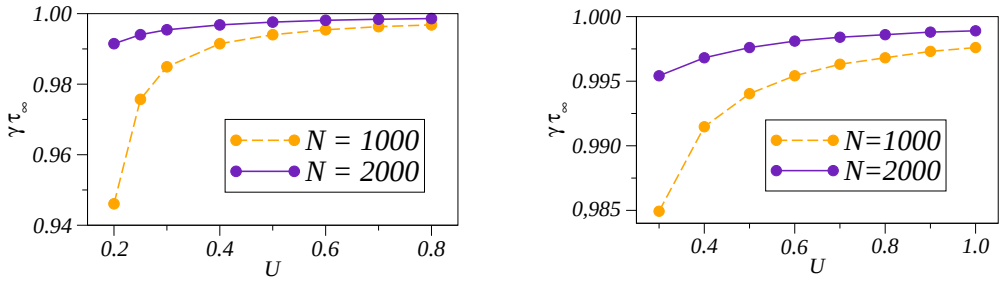

Figure 4.7. *Bias dependence of $\gamma\tau_\infty$ for different system sizes. The left panel shows the disorder-free lattice $\sigma = 0$. The right panel displays the results, comprising averages over 50 realizations of disorder, for the biased lattice with long-range correlated disorder, $\sigma = 1$ and $\alpha = 4$.*

disorder-free lattices is the same as in the isolated monomer (i.e. single exponential with decay time $1/\gamma$), when the system is large enough.

A similar exponential decay of the fluorescence is expected for finite-size ordered systems. Moreover disordered lattices, generated according to the disorder distribution Eq. (2.2) in the strong correlated limit, seem to behave also in a similar way due to the numerical results obtained for the optical absorption spectrum and the fluorescence decay. In such cases the decay time is found to be the same as in the single monomer as well and consequently, it is independent of the bias. We have performed simulations in finite systems when $\sigma = 0$ to obtain the decay time τ_∞ from the fluorescence intensity curves when $t \to \infty$. Results are shown in the left panel of Fig. 4.7, where we observe that $\gamma\tau_\infty$ approaches the theoretical limit ($\gamma\tau_\infty = 1$) on increasing both the system size or the bias. The localization length L_B due to the presence of the bias decreases on increasing U, leading to smaller finite-size effects. For the sake of completeness we perform the same study in a biased lattice with long-range correlated disorder. As expected, in the right panel of Fig. 4.7 we observe a similar trend to that found in disorder-free lattices. The main difference is related to the value of τ_∞, which is slightly lower than in disorder-free lattices of the same size due to disorder effects.

4.7. Conclusions

In this chapter we studied the intraband exciton relaxation in a biased 1D system whose site energies are disordered following a long-range correlated distribution. Exciton transport is considered as incoherent hoppings between the eigenstates of the static lattice, arising when the coupling to vibrations is taken into account. The dynamics of the intraband relaxation is monitored by means of the fluorescence decay after broadband pulse excitation calculated within a Pauli master formalism.

Our starting point was the unbiased system ($U = 0$) for which a non-exponential fluorescence decay was found for any value of correlation exponent. This time-dependence reflects the existence of many decay channels in the system with different decay times. As a main feature, it is to be noticed that a fluorescence decay slowdown arises when $\alpha > \alpha_c$, which we relate to the peculiar level structure in this case, see Sec. 4.3.

In biased systems the fluorescence behaves differently depending on the intensity of the bias as the same way as the absorption spectrum does, see Chap. 3. Indeed, a relationship between both magnitudes can be established.

At moderate bias no signatures of the WSL are found in the absorption spectrum. This gives rise to a non-exponential fluorescence decay. However, on further increasing the magnitude of the bias, a periodic pattern is found to build up at the center of the (already wide) absorption band when $\alpha > \alpha_c$. Its period is independent of the system size N and equal to U as for the WSL in an ideal lattice. Simultaneously, the fluorescence decay is described approximately by a single exponential. Finally, when the parameter $\sqrt{U}$ exceeds the magnitude of disorder σ, the WSL in the absorption spectrum and the exponential decay of the fluorescence appear, irrespective of the value of the correlation exponent α.

We qualitatively explained the correspondence between the WSL absorption spectrum and the exponential fluorescence decay. When the localization by the bias effect is large enough, all states will display the same amplitude of probability within their localization length. As a result they carry approximately the same value of the oscillator strength. Therefore, a single exponential decay characterized by same time-scale relaxation is expected. Deviations from perfect exponential decay were related not only to stochastic fluctuations of the disorder but mainly to finite-size effects as studied in Sec. 4.6.

Chapter 5

Effect of the intrinsic base pairing on the localization properties of DNA molecules

In this chapter we consider a ladder model of DNA for describing electronic transport in a fully quantum-mechanical regime. Backbone effects are neglected while a single orbital is assigned to every base, assuming that conduction takes place through orbital overlap. Due to the disorder appearing in DNA sequences, localized states are expected in general, giving rise to an insulator behavior for DNA. However, correlations in the disorder might enhance the conduction along DNA molecules by increasing the localization length of the system states. In this regard, we study the localization properties revealed by a DNA-ladder model and its dependence on the intrinsic base pairing correlations, as well as on the hopping parameters of the model.

5.1. Introduction

DNA has always attracted much attention from different perspectives due to its main role in biological processes. Nevertheless in the last decade its electronic properties turned out to be a new promising field of study due to the search of new materials for nanotechnological aims such wires, transistors, diodes and all sorts of molecular electronics [110–113]. Furthermore DNA, assembling spontaneously [29], has also revealed itself as a very useful building material to organize other higher conductive nanomaterials [30].

In this sense a lot of experiments have been performed searching for signatures of long-range transport along DNA molecules. However, there is not a common conclusion about its conducting properties yet. The particular sequence, the contacts and the surrounding environment seem to have enormous effects on the experimental results. Therefore, different conducting behaviors for DNA molecules have been reported, i.e. metallic [114–117], semiconducting [118–123], insulating [124–126] or even superconducting [127].

From a theoretical point of view it is to be noticed that according to standard theories of disordered systems [33], all states in low-dimensional systems with uncorrelated disorder are spatially localized. This is the general case when dealing with DNA molecules which do not present periodic sequences, i. e. λ-DNA [126]. Then, in a pure quantum-mechanical regime, these molecules would lead to an insulator behavior unless the localization length of their states reaches anomalously large values. On the contrary, spatial correlations of the nucleobases might enhance the long-range transport along the molecules [54–56, 128–130]. In particular, those models which support long-range correlations so that its power-law spectral density reads $S(k) \sim 1/k^{\alpha}$ with $\alpha > 0$, result in a phase of extended states at the band center, provided α is larger than a critical value α_c [50–52]. As a consequence, long-range charge DNA transport might be feasible even at very low temperature, provided the chemical potential lies within the band of extended states, see Chap. 2.

Some authors claimed that intrinsic DNA-correlations, due to the base pairing (AT and GC) between the two DNA-strands, lead to electron delocalization even if the base sequence along one of the strands is random and uncorrelated [131]. Indeed, they pointed out that there is a localization-delocalization transition (LDT) for certain hopping parameters range. Nevertheless it was later proven that this is not the case and all states remain localized [132].

In this chapter we make clear the role of the intrinsic DNA correlations due to the

base pairing in electronic transport. To this end we study the Landauer and the Lyapunov coefficients in a DNA-ladder model to analyze the spatial extent of its eigenstates. Furthermore we point out the main features resulting from considering different values of the hopping parameters.

5.2. DNA-ladder model

The DNA is a double-stranded molecule in which each of these strands is consistent of a sequence of nucleotides formed by a nucleobase bonded to sugar and phosphates. These latter are usually known as the backbone of the molecule. The most common geometry for observed DNA molecules is the double-helix geometry which is usually known as B-type DNA. From a theoretical point of view it seems reasonable to consider the untwisted helix as a first approximation, and to deal with a planar geometry for the DNA molecule [133].

In order to describe this system we consider a ladder model of DNA in a fully coherent regime and assign a single orbital to each base. Conduction through the sugar-phosphate backbone is neglected hereafter. The double-stranded DNA molecule is described by means of a tight-binding Hamiltonian within the nearest-neighbor approximation. It is worth mentioning that consecutive bases along the stacking direction are coupled by covalent interactions while the coupling within a base pair is due to hydrogen bonds. Because of the different nature of these interactions, two hopping parameters are considered in the model, namely interstrand ($t_\perp$) and intrastrand ($t_\parallel$) hoppings. For the sake of simplicity we will assume that both hoppings do not depend on the base hereafter. Figure 5.1 shows a schematic view of a fragment of this ladder model.

Four different energy sites (ε_A, ε_T, ε_C, and ε_G) are randomly assigned in one of the strands with the same probability while the second strand is defined following the DNA pairing (A–T and C–G). Hereafter we will restrict ourselves to the following values of the site energies, taken from molecular orbital calculations [134, 135], $\varepsilon_A = 8.24\,\mathrm{eV}$, $\varepsilon_T = 9.14\,\mathrm{eV}$, $\varepsilon_C = 8.87\,\mathrm{eV}$ and, $\varepsilon_G = 7.75\,\mathrm{eV}$. The two remaining parameters in the model, namely $t_\perp$ and $t_\parallel$, will be varied in our calculations.

The described model is the one considered by Caetano and Schulz in Ref. [131] which does not consider backbone effects. It is to be noticed that the lattice model including the backbone can be easily mapped onto a ladder model similar to that presented above with energy-dependent hoppings [45, 46].

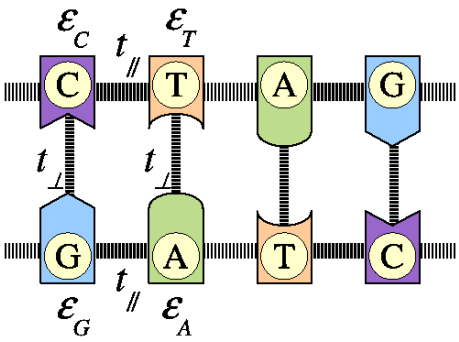

Figure 5.1. *Schematic view of a fragment of the ladder model for DNA molecules, excluding the sugar-phosphate backbone. A single orbital is associated to each base, with a corresponding energy ε_n, n being A, T, C or G.*

According to the proposed model, we can write down the equations for the amplitudes at different bases as following:

$$E\psi_n^{(1)} = \varepsilon_n^{(1)}\psi_n^{(1)} + t_{\parallel}\left(\psi_{n+1}^{(1)} + \psi_{n-1}^{(1)}\right) + t_{\perp}\psi_n^{(2)} \ , \tag{5.1a}$$

$$E\psi_n^{(2)} = \varepsilon_n^{(2)}\psi_n^{(2)} + t_{\parallel}\left(\psi_{n+1}^{(2)} + \psi_{n-1}^{(2)}\right) + t_{\perp}\psi_n^{(1)} \ . \tag{5.1b}$$

The notation reads as follows: $\psi_n^{(\sigma)}$ refers to the amplitude of the state at the bases, $\sigma = 1, 2$ runs over the two strands and $n = 1, 2, \ldots, N$ denotes the position of the bases at each strand. As it was already mentioned $\varepsilon_n^{(\sigma)}$ takes one of the four values of the site energies.

5.3. Landauer and Lyapunov exponents

The previous equations for the amplitudes can be expressed in a compact form by using 4×4 transfer matrices. To this end we introduce the 4-vector $\mathbf{\Phi}_n \equiv \left(\psi_n^{(1)}, \psi_n^{(2)}, \psi_{n-1}^{(1)}, \psi_{n-1}^{(2)}\right)^t$ where the superscript t indicates the transpose. Defining the following 2×2 matrix [136]

$$M_2^{(n)} \equiv \begin{pmatrix} \frac{E-\varepsilon_n^{(1)}}{t_{\parallel}} & -\frac{t_{\perp}}{t_{\parallel}} \\ -\frac{t_{\perp}}{t_{\parallel}} & \frac{E-\varepsilon_n^{(2)}}{t_{\parallel}} \end{pmatrix} \ , \tag{5.2}$$

the transfer matrix equation of the model reads $\mathbf{\Phi}_{n+1} = T_n\mathbf{\Phi}_n$, with

$$T_n \equiv \begin{pmatrix} M_2^{(n)} & -\mathcal{I}_2 \\ \mathcal{I}_2 & \mathcal{O}_2 \end{pmatrix} \ , \tag{5.3}$$

where $\mathcal{I}_2$ and $\mathcal{O}_2$ are the unity and null 2×2 matrices, respectively. One can easily find, that the 4×4 transfer matrix T_n satisfies the condition $T_n^\dagger \mathcal{J} T_n = \mathcal{J}$ where $\dagger$ denotes the Hermitian conjugate matrix and

$$\mathcal{J} = \begin{pmatrix} 0 & 0 & -i & 0 \\ 0 & 0 & 0 & -i \\ i & 0 & 0 & 0 \\ 0 & i & 0 & 0 \end{pmatrix} , \tag{5.4}$$

meaning that T_n belong to the $SU(2,2)$ group.

In order to study the localization properties of the whole sequence, the full transfer matrix $\mathcal{M}_N = \prod_{n=N}^{1} T_{n,ij}$ should be taken into account. Notice that, due to the intrinsic base pairing only four transfer matrices can appear in an arbitrary DNA sequence: $T_{n,AT}$, $T_{n,TA}$, $T_{n,CG}$ or $T_{n,GC}$.

Assuming exponential localization for the eigenstates, the eigenvalues of the limiting matrix $\lim_{N\to\infty} \ln(\mathcal{M}_N \mathcal{M}_N^\dagger)^{1/2N}$ provide information about the localization length of the states [137], which is measured in units of the base separation along a single strand (3.4 nm). These eigenvalues are usually known as the Lyapunov exponents λ_{Ly}. Notice that the infinite limit can be substituted by a product of random transfer matrices over a long enough system due to the self-averaging property of the Lyapunov exponent [138].

On the other hand, the Landauer exponent whose definition reads $\lambda_{\mathrm{La}}(N) = \ln\langle\, ||\prod_{n=N}^{1} T_{n,ij}||\,\rangle^{1/N}$ (hereafter $\langle \ldots \rangle$ denotes ensemble averages) becomes twice the largest Lyapunov exponent for extended states in 1D systems [139, 140].

Both exponents are relevant in the analysis of the localization properties of the system. Indeed, in a quasi-one-dimensional system as the considered DNA-ladder model, it is expected that the Lyapunov and the Landauer exponents are also proportional but the ratio between them can be different from 2. It is worth noticing that the former might be affected by convergence problems [141] while the latter can be analytically calculated, see Refs. [136, 142, 143]. Therefore, both exponents provide complementary information and should be considered for completeness.

5.4. Base pairing effects

5.4.1. Landauer exponent

In Refs. [136, 142, 143] it was shown that the Landauer exponent can be calculated exactly. To this end, the direct product $\mathcal{M}_N \otimes \mathcal{M}_N^\dagger$ of the fundamental representations of transfer matrices of the $SU(1,1)$ group is reduced to the adjoint one. We apply this technique here for the group $SU(2,2)$. In order to calculate this direct product exactly, we use the known representation of the permutation operator via generators τ^μ ($\mu = 1, \ldots, 15$) of the $sl(4)$ algebra as $P = (1/4)(\mathbb{I} \otimes \mathbb{I} + \tau^\mu \otimes \tau^\mu)$. Thus the matrix elements satisfy

$$\delta_{\alpha_1}^{\alpha_2}\delta_{\beta_1}^{\beta_2} = \frac{1}{4}\left[\delta_{\alpha_1}^{\beta_2}\delta_{\beta_1}^{\alpha_2} + (\tau^\mu)_{\alpha_1}^{\beta_2}(\tau_\mu)_{\beta_1}^{\alpha_2}\right] , \tag{5.5}$$

where we assume summation in the repeated indices μ. Among the generators τ^μ there is one which coincides with the metric $\mathcal{J}$ defined in Eq (5.4). We denote the corresponding index μ as J, namely $\tau^J = \mathcal{J}$.

Multiplying Eq. (5.5) by T_n and $T_n^\dagger$ from the left and right hand sides respectively, one can express the direct product of T_n and $T_n^\dagger$ via their adjoint representation

$$(T_n)_{\alpha'}^{\alpha}(T_n^\dagger)_{\beta}^{\beta'} = \frac{1}{4}(\mathcal{J})_{\beta}^{\alpha}(\mathcal{J})_{\alpha'}^{\beta'} + \frac{1}{4}(\tau^\mu\mathcal{J})_{\alpha'}^{\beta'}\Lambda_n^{\mu\nu}(\mathcal{J}\tau^\nu)_{\beta}^{\alpha} . \tag{5.6}$$

Here the adjoint representation Λ_n of T_n is defined by

$$\Lambda_n^{\mu\nu} = \frac{1}{4}\mathrm{Tr}(T_n\tau^\mu T_n^\dagger\tau^\nu) , \tag{5.7}$$

being an 15×15 matrix that depends on the parameters of the model at site n of both chains.

It is then straightforward to get the average over four equivalent substitutions of the base pairs in the random chain

$$\langle\Lambda\rangle = \frac{1}{4}\left(\Lambda_{AT} + \Lambda_{TA} + \Lambda_{CG} + \Lambda_{GC}\right) . \tag{5.8}$$

The Landauer exponents are the nonnegative eigenvalues of $\frac{1}{2}\log\langle\Lambda\rangle$[a].

The condition of the existence of an extended state is equivalent to $\det|\langle\Lambda\rangle - \mathcal{I}| = 0$. In order to elucidate if this condition can be met, we solve the eigenvalue problem associated with the matrix $\langle\Lambda\rangle$, namely $\det|\langle\Lambda\rangle - z\mathcal{I}| = 0$. We prove that for a reasonable set of

[a]This theoretical formalism was entirely developed in Refs. [136, 142, 143]

hopping parameters there is no solution $z = 1$ and then, no extended states. For the sake of clarity Fig. 5.2 shows the magnitude $|z - 1|$ for the eigenvalues of the problem when considering the hoppings used by Caetano and Schulz [131]. In view of this figure it is clear that none of them is equal to unity. Therefore, we come to the conclusion that the system studied by Caetano and Schulz [131] cannot support truly extended states. Consequently, a LDT is not to be observed since all states are spatially localized.

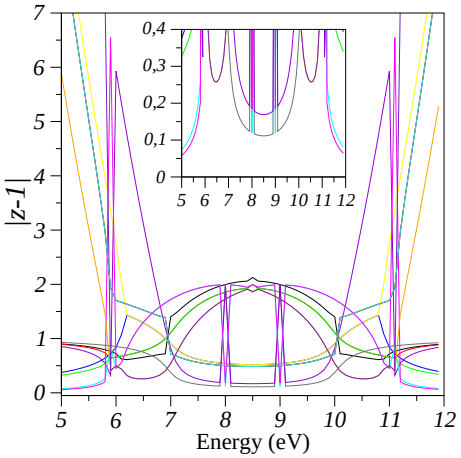

Figure 5.2. *Euclidean distance to unity of all eigenvalues of the matrix* $\langle\Lambda\rangle$ *within the energy spectrum of the system, indicated by different colors, for* $t_\perp = 0.5\,\text{eV}$ *and* $t_\parallel = 1.0\,\text{eV}$.

5.4.2. Lyapunov exponent

So far we have proven that no LDT arises in the considered DNA-ladder model. However, the results of transport experiments [114–123] might be consistent with the existence of localized states whose localization length is larger then the typical size of the system. In order to estimate this localization length we numerically calculate the Lyapunov exponents by way of the discrete QR algorithm [141]. We perform this calculations in a system of size $N = 4000$ considering those hoppings used by Caetano and Schulz [131], $t_\perp = 0.5\,\text{eV}$ and $t_\parallel = 1.0\,\text{eV}$. Notice that these parameters are larger than those usually considered in the literature [144–146] but our first objective is to test the conclusions of Ref. [131].

From Fig. 5.3 it becomes clear that neither the largest Lyapunov exponent nor the

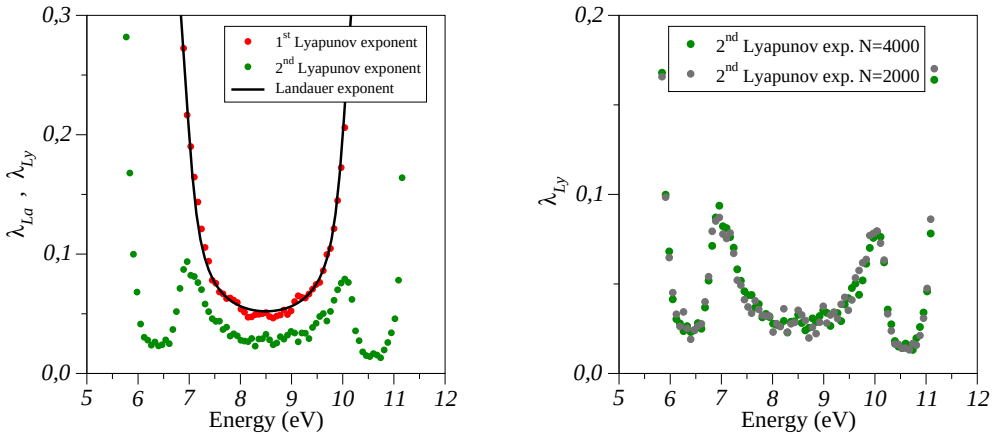

Figure 5.3. 2/3 *of Landauer exponent* λ_{La} *(solid line) and the Lyapunov exponents* λ_{Ly}*, as a function of energy, for* $N = 4000$*,* $t_{\perp} = 0.5\,eV$ *and* $t_{\parallel} = 1.0\,eV$ *are shown in the left panel. The second and smaller Lyapunov exponent* λ_{Ly} *as a function of energy for a different system size* $N = 2000$ *is also displayed in the right panel for* $N = 2000$ *and* $N = 4000$*.*

Landauer one vanishes over the whole energy spectrum. Furthermore, taking the inverse of the minimum value of the Lyapunov exponents, we come to a maximum localization length of the order of ≈ 80 base pairs. It is worth mentioning that this value does not depend on the system size as it is shown in the right panel of Fig. 5.3. This reveals a clear signature of the true localization of the states and indicates that the base pairing effects cannot lead to long-range transport at low temperature.

In order to elucidate the influence of the base pairing on the localization properties, we perform the calculation for the Landauer and the Lyapunov exponents in an artificial model where base pairing is not considered. In such a case both strands are completely random and therefore, new pairs and new transfer matrices are allowed, (e.g. AC or AA). By switching off the base pairing correlations our system becomes even more disordered and even smaller localization lengths are expected. However, this is not revealed by our calculations shown in Fig. 5.4. In this case we plot the inverse of the second Lyapunov exponent which provides the largest possible value for the localization length. Contrary to what we expected the localization length seems not to depend on base pairing correlations over almost the whole energy spectrum. Indeed it seems to be reduced only close to the two resonances around 6.4 eV and 10.6 eV. Nevertheless, these resonances appear for

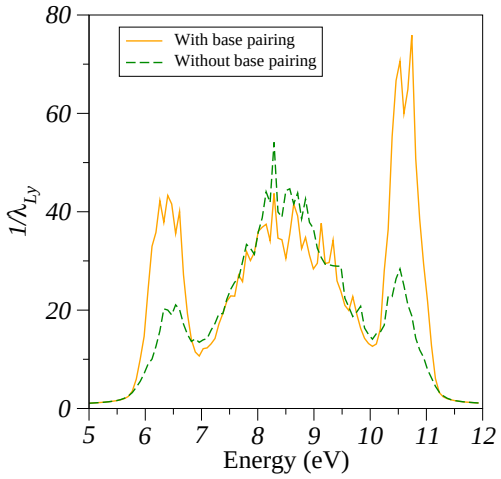

Figure 5.4. *Inverse of the second Lyapunov coefficient for* $N = 4000$ $t_\perp = 0.5\,eV$ *and* $t_\parallel = 1.0\,eV$*, when the base pairing is present (solid line) and absent (dashed line).*

the uncorrelated and the paired system so they cannot originate from the base pairing correlations. In view of all these results our claim is that the base pairing does not significatively affect the localization properties of the considered DNA-ladder model.

5.5. Hopping parameters effects

5.5.1. Lyapunov exponent

In this section we analyze the dependence of the localization length of the states on the hopping parameters $t_\perp$ and $t_\parallel$. In this sense we calculate the inverse of the second Lyapunov exponent as in the previous section but using hoppings of the order of those found usually in the literature [144–146], see Fig. 5.5. In particular we take $t_\perp = 0.05\,\text{eV}$ and $t_\parallel = 0.5\,\text{eV}$ as representative parameters. It is worth mentioning that lower hoppings lead to a *more-effective* disorder and even smaller localization lengths are expected. This means that it might well be that the overestimation of the hoppings by Caetano and Schulz [131] gave rise to larger localization lengths than those of a realistic system.

Figure 5.5 shows a dramatic decrease of the localization length of the states by using lower hopping parameters in the DNA-ladder model. In particular the states at the center

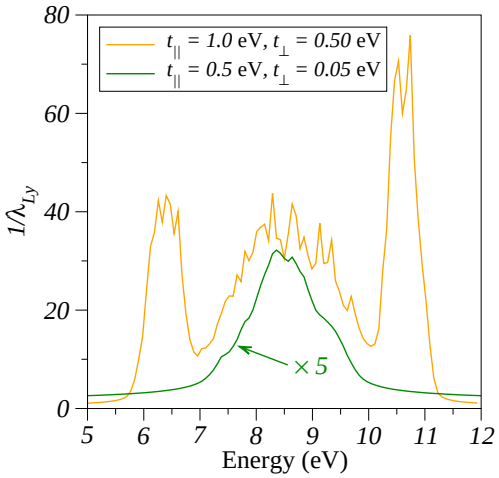

Figure 5.5. *Inverse of the second Lyapunov coefficient for $N = 4000$ and two sets of hopping parameters, indicated on the legend box. Notice the scaling factor indicated on the lower curve.*

of the band are five times more localized than in the system considered in Ref. [131]. This effect is even stronger at the mentioned resonances. Therefore, we come to the conclusion that hopping is a more important mechanism for delocalization than base pairing in this ladder model.

As a further step we have obtained the minimum Lyapunov exponent for realistic values of the hopping parameters, namely $\{t_\perp, t_\parallel\} \in [0, 1]\,\mathrm{eV}$ in order to reach a quantitative picture of the influence of them on the localization length. We summarize our results in Fig. 5.6 where the maximum localization length, in units of the lattice period, for different set of parameters $\{t_\perp, t_\parallel\}$ is plotted.

Though the localization length depends smoothly on the particular set of hoppings, in all considered cases it remains much smaller than the system size ($N = 4500$). Indeed, even in the most favorable situation of our simulations, the eigenstates would only cover a 3% of the system size.

5.5.2. Time-dependent participation ratio

Finally, we will analyze the time-evolution of an initially-localized wave packet. In this sense our interest is to check if the expected spread of the packet might give rise to

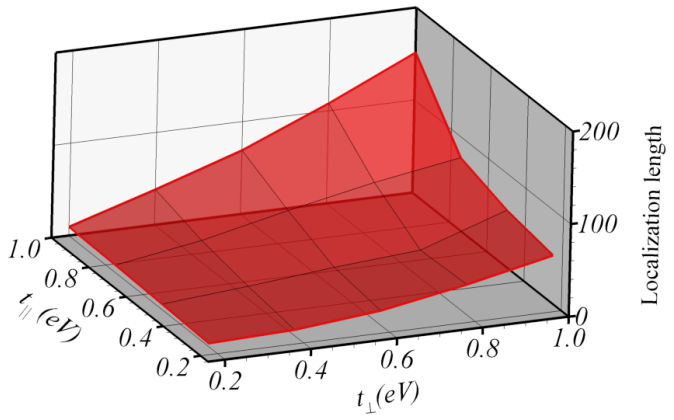

Figure 5.6. *Maximum localization length for $N = 4500$ as a function of the hopping parameters, $t_\perp$ and $t_\parallel$. Notice that the localization length is much smaller than the system size even for high values of the hopping parameters.*

a localization length larger than the system size. To compute the spread of an initially-localized wave packet we solve the time-dependent Schrödinger equation for the amplitudes at different bases which for this system read

$$i\hbar\frac{d\psi_n^{(1)}}{dt} = \varepsilon_n^{(1)}\psi_n^{(1)}(t) + t_\parallel\left(\psi_{n+1}^{(1)}(t) + \psi_{n-1}^{(1)}(t)\right) + t_\perp\psi_n^{(2)}(t)\ , \tag{5.9a}$$

$$i\hbar\frac{d\psi_n^{(2)}}{dt} = \varepsilon_n^{(2)}\psi_n^{(2)}(t) + t_\parallel\left(\psi_{n+1}^{(2)}(t) + \psi_{n-1}^{(2)}(t)\right) + t_\perp\psi_n^{(1)}(t)\ . \tag{5.9b}$$

The procedure is rather standard and the details can be found in Ref. [147]. Our simulation takes as the initial condition the following localized state $\psi_n^{(\sigma)}(t=0) = (1/\sqrt{2})\delta_{n,N/2}$ ($\sigma = 1, 2$) and the monitored magnitude is the time-dependent participation number, defined as

$$P(t) = \left(\sum_{n.\sigma}|\psi_n^{(\sigma)}(t)|^4\right)^{-1}\ . \tag{5.10}$$

In a similar way as in Sec. 2.3.1 $P(t)$ gives an estimation of the length over which the wave packet spreads but now its evolution in time is taken into account. For the sake of clarity $P(t)$ will be normalized to the number of sites, $2N = 60$, to provide a better description of the ratio between the state extension and the system size. Our simulations are performed for a wide range of hopping parameters $\{t_\perp, t_\parallel\}$. For all hooping parameters we find that $P(t)$ saturates at a value P_{sat} much smaller than the system size, even for

unrealistic and large hopping parameters. We plot this saturation value $P_{\rm sat}$ as a function of the hopping parameters in Fig. 5.7. In all cases the saturation value normalized to

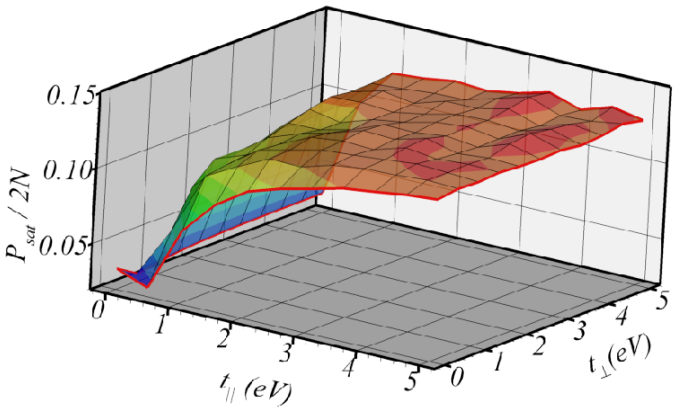

Figure 5.7. *Saturation value of the participation number P_{sat}, normalized to the number of sites $2N = 60$, as a function of the hopping parameters, $t_\perp$ and $t_\|$.*

the system size is much smaller than unity. Thus, even considering the time-dynamics of a localized wave-packet, the considered DNA-ladder model cannot support localization lengths larger than the system size.

5.6. Conclusions

In this chapter we considered a ladder model of DNA for describing electronic transport in a fully quantum-mechanical regime. In this model, a single orbital is assigned to each base, and the sugar-phosphate is excluded. Therefore, it is assumed that electronic conduction takes place through the orbital overlap at the bases. However it is to be noticed that the backbone effects can be easily included in this model by considering energy-dependent hoppings [45, 46]. We described this DNA-ladder model by means of a tight-binding Hamiltonian within the nearest-neighbor approximation. For the sake of simplicity we neglect the dependence of the hoppings on the bases, only considering two different parameters for the interstrand ($t_\perp$) and the interstrand ($t_\|$) interaction. Well established site energies for the four bases are considered, see Ref. [134, 135]. In order to describe a general DNA sequence, random energies are assigned for one of the DNA strands, while the other is defined according to the base complementarity (A-T, G-C).

By calculating the Landauer and the Lyapunov exponents we analytically and numerically demonstrated that the existence of intrinsic correlations due to the base pairing is not a sufficient condition for the occurrence of extended states in this system. Then, no LDT can take place, contrary to what was claimed in Ref. [131].

As a further step we analyzed the effects of the base pairing on the localization properties of the system by comparing the Lyapunov exponent for uncorrelated and paired systems. We observed that base pairing has negligible effects on the localization length except close to two resonant energies, located at 6.4 eV and 10.6 eV for $t_\perp = 0.5\,\text{eV}$ and $t_\parallel = 1.0\,\text{eV}$. Nevertheless, in all cases we obtained localization lengths much smaller than the system size.

The maximum localization length of the system was also calculated as a function of the hoppings $\{t_\perp, t_\parallel\}$ revealing its stronger dependence on these parameters. As expected, smaller hoppings give rise to more localized states in the system since they lead to a *more-effective* disorder. In particular, for hoppings of the order of those found in the literature, we obtained a maximum localization length which covers roughly a 3% of the system size.

Finally, to provide further support to the claim that the localization length remains finite for all values of the hopping parameters, we undertake the study of the time-evolution of electron wave packets. To this end, we solve the time-dependent Schrödinger equation to compute the spread of an initially-localized wave packet. In all numerical simulations we find that $P(t)$ saturates at a value P_{sat} much smaller than the system size even for unrealistic and large hopping parameters.

After our analysis we conclude that base pairing alone is unable to explain electronic transport at low temperature in random DNA-sequences. On the other hand, the magnitude of the hopping seems to have a stronger influence on the localization properties of the DNA-ladder model. So far parameters usually found in literature cannot support the idea of long-range transport either in this type of DNA. Nevertheless, in view of its important effects on the DNA properties, a better definition of the hopping parameters seems to be crucial to theoretically describe the conducting behavior of DNA molecules.

Chapter 6

Interband optical transitions in DNA-ladder models.

The underlying band structure of the semiconducting synthetic DNA, such as the poly(G)-poly(C), suggests the allowance of interband optical transitions. In this chapter we propose the study of such transitions as a complementary tool to understand contradictory experimental results about the conducting DNA properties. The influence of the backbone of DNA on these optical transitions, the static environment interactions and the helical conformation is also considered. Finally, we discuss a possible experimental set up to measure the optical absorption of poly(G)-poly(C) DNA molecules in the visible region.

6.1. Introduction

In the previous chapter it was already mentioned the variety of experimental results related to the conducting properties of DNA molecules found in the literature, see Sec. 5.1 for an overview. Due to its size in the nanometer scale range and its self-assembly properties as well as the molecular recognition, DNA becomes a new promising material for designing new nanostructures [29] for technological applications [23]. In particular those experiments which reveal a semiconducting behavior [118–123] for DNA molecules might open the possibility to develop a new electronics based on this affordable biomaterial. The main problem is that electrical experiments seem to be rather affected by the detailed sequence of nucleotides or the environment conditions such as contact, thermal or solution effects and it is difficult to come to a common conclusion about this topic.

However, in the case of dry synthetic DNA, such as the poly(G)-poly(C) (consistent of a G-homopolymer strand coupled to its complementary, namely a C-homopolymer one), theoretical calculations already predicted its semiconducting behavior in the sixties [148] while first experimental evidences appeared much later [118]. Since this crucial experimental goal, several theoretical models [44–46, 133, 149–154] have provided a reasonable description of the semiconductor gap observed in experiments. Despite most of them having been based on effective Hamiltonian models within the tight-binding approximation, there is no complete agreement about the parameters yet. In this sense, the influence of the hopping parameters on the localization properties of a DNA-ladder model and then, on the long-range transport along DNA molecules, was reported in Chap. 5.

Assuming the semiconducting behavior of synthetic DNA molecules, it seems reasonable to apply well established theoretical and experimental procedures frequently used for traditional semiconductors. Such materials support optical transitions between the valence and the conduction bands and its analysis provides relevant information to characterize the semiconductor under consideration.

Therefore in this chapter we get into the study of the interband optical transitions between the highest occupied molecular orbital (HOMO) and lowest unoccupied molecular orbital (LUMO) bands in DNA. This optical study facilitate an insight into the electronic band structure of DNA providing useful tools to define more realistic theoretical models. For instance, the relevance of the inclusion of the backbone in theoretical models might be established. In addition, this analysis might allow us to elucidate whether poly(G)-poly(C)

DNA behaves as a direct or indirect band gap semiconductor, what is also important for developing new optical devices.

In this chapter we use two different DNA models, previously introduced in Refs. [45] and [133], to describe the main features of the optically induced electronic transitions in the synthetic semiconducting DNA. We also focus on the effect of the environment on DNA properties, not only in vivo but mainly in experimental situations, by introducing a disorder contribution to the site energies of the DNA bases. Besides, we consider a more realistic helix conformation of DNA molecules, which is expected to be relevant when dealing with optical transitions. Finally, we discuss what kind of poly(G)-poly(C) samples are the most appropriate to measure the interband optical transitions in the visible region, as well as what experimental conditions are the optimal ones to enable us to observe these weak transitions.

6.2. DNA-ladder models

Our analysis proceeds as follows. We consider two ladder models of DNA [45, 133], referred to as the dangling backbone ladder (DBL) model and the simple ladder (SL) model hereafter. The former model considers both base and backbone molecules, while the latter describes only the π-stack of base pairs. Similar models have been previously introduced by several authors [44–46,133,149–154]. In order to study collective electronic properties of the whole DNA molecule, we restrict ourselves to one orbital per base within both models and therefore, intra-molecule transitions are excluded in this work. The nearest-neighbor approximation is used for inter-strand and intra-strand hoppings, defined as in Sec. 5.2.

6.2.1. Dangling backbone ladder model

The DBL model assumes that the value of intra-strand ($t_{\|}$) hoppings is the same for both strands since it takes into account interactions between two identical bases in both cases $t_{GG} = t_{CC} = t_{\|}$. In addition, since poly(G)-poly(C) DNA consists of a sequence of identical base pairs, a uniform value for the inter-strand ($t_{\perp}$) hopping is also considered. We neglect the conduction through the sugar-phosphate backbone but keep the coupling of the backbone to the stack of base pairs, describing it by the hopping t_q. Left panel of Fig. 6.1 shows a schematic view of a fragment of the poly(G)-poly(C) DNA within the

DBL model.

The tight-binding Hamiltonian for this model reads

$$\begin{aligned}\mathcal{H} &= \sum_{n=1}^{N}\Big[\sum_{s=G,C}\left(\varepsilon_n^s a_{s,n}^\dagger a_{s,n}+\gamma_n^s b_{s,n}^\dagger b_{s,n}+t_q a_{s,n}^\dagger b_{s,n}+t_q b_{s,n}^\dagger a_{s,n}\right)\\ &+ t_\perp a_{G,n}^\dagger a_{C,n}+t_\perp a_{C,n}^\dagger a_{G,n}+t_{GG}(a_{G,n}^\dagger a_{G,n+1}+a_{G,n+1}^\dagger a_{G,n})\\ &+ t_{CC}(a_{C,n}^\dagger a_{C,n+1}+a_{C,n+1}^\dagger a_{C,n})\Big]. \end{aligned} \tag{6.1}$$

Here $a_{s,n}^\dagger$ ($a_{s,n}$), $b_{s,n}^\dagger$ ($b_{s,n}$) denotes creation (annihilation) operators while ε_n^s and γ_n^s refer to site energies for basis and backbone respectively, being $s = G, C$.

Once the model has been established, we can write down the equation for the electronic amplitudes at the bases. Let us denote these amplitudes as ψ_n^s, where $n = 1, 2, \ldots N$ labels a base pair and the superscript $s = G, C$ labels the G and C strands, respectively. The total number of sites in the tight-binding model is $4N$. The equations for the amplitudes are given by

$$\left(E-\alpha_n^C\right)\psi_n^C = t_\parallel\left(\psi_{n+1}^C+\psi_{n-1}^C\right)+t_\perp\psi_n^G\ , \tag{6.2a}$$

$$\left(E-\alpha_n^G\right)\psi_n^G = t_\parallel\left(\psi_{n+1}^G+\psi_{n-1}^G\right)+t_\perp\psi_n^C\ , \tag{6.2b}$$

with renormalized site energy

$$\alpha_n^s = \varepsilon_n^s + \frac{t_q^2}{E-\gamma_n^s}\ . \tag{6.2c}$$

After solving the equations for the electronic amplitudes at the bases, the amplitudes at backbone sites can be obtained from

$$\phi_n^s = \frac{t_q}{E-\gamma_n^s}\,\psi_n^s\ . \tag{6.2d}$$

It should be stressed that the DBL model is equivalent to a SL model, in which the site energies of the bases (6.2c) are renormalized due to the coupling to the backbone [45, 46].

6.2.2. Simple ladder model

Because the backbone seems to have little effect on the DNA transport properties, it is neglected completely within the framework of the SL model. This is the case when the electronic bands arising from the hybridization of backbone levels (with energies γ_n^s, as shown in Fig. 6.1) lie at much higher energy than the levels of the bases [46, 155]. In this

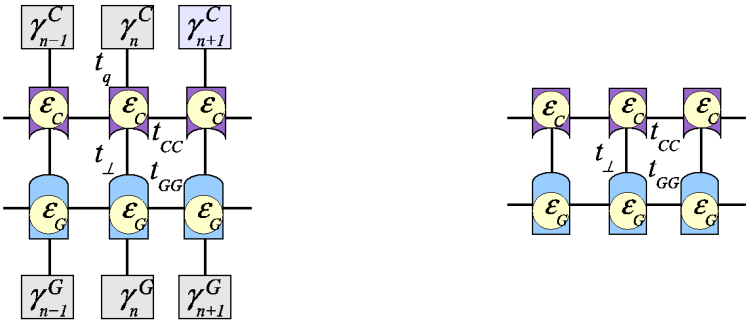

Figure 6.1. *Schematic view of a fragment of poly(G)-poly(C) DNA molecules, according to the DBL model (left panel) and the SL model (right panel). Only two different hoppings are considered: the inter-strand ($t_\perp$) and the intra-strand ($t_{GG} = t_{CC} = t_\parallel$) one. In addition, coupling between the backbone and the pair of bases is mediated through the hopping t_q in the DBL model.*

case, one could neglect the terms $t_q^2/(E - \gamma_n^s)$ in Eq. (6.2c) to describe the bands arising from the bases. Consequently, the Hamiltonian for this model becomes the following

$$\begin{aligned} \mathcal{H} &= \sum_{n=1}^{N} \Big[\sum_{s=G,C} \left(\varepsilon_n^s a_{s,n}^\dagger a_{s,n} + t_\perp a_{G,n}^\dagger a_{C,n} + t_\perp a_{C,n}^\dagger a_{G,n} \right) \\ &+ t_{GG}(a_{G,n}^\dagger a_{G,n+1} + a_{G,n+1}^\dagger a_{G,n}) \\ &+ t_{CC}(a_{C,n}^\dagger a_{C,n+1} + a_{C,n+1}^\dagger a_{C,n}) \Big], \end{aligned} \tag{6.3}$$

and the equations for the amplitudes reduce to

$$(E - \varepsilon_C)\,\psi_n^C = t_{CC}\left(\psi_{n+1}^C + \psi_{n-1}^C\right) + t_\perp \psi_n^G\,, \tag{6.4a}$$

$$(E - \varepsilon_G)\,\psi_n^G = t_{GG}\left(\psi_{n+1}^G + \psi_{n-1}^G\right) + t_\perp \psi_n^C\,. \tag{6.4b}$$

6.3. Electronic wave functions

6.3.1. DBL model: indirect band gap semiconductor

From now on we consider a uniform DBL model, in which all base energies take the same value. Although this model cannot describe any real DNA, it is very enlightening

and allows for understanding of the main features of the interband optical transitions. To this end, in this section we set $\gamma_n^s = \varepsilon_n^s = 0$. The discussion of the DBL model with different site energies on each strand is presented in Sec. 6.4 below.

Introducing the symmetric and antisymmetric combinations of amplitudes $\psi_n^{\pm} = \psi_n^C \pm \psi_n^G$ [156], we can decouple Eqs. (6.2) to obtain

$$\left(E \mp t_\perp - \frac{t_q^2}{E}\right) \psi_n^{\pm} = t_\parallel \left(\psi_{n+1}^{\pm} + \psi_{n-1}^{\pm}\right) \ . \tag{6.5}$$

The eigenfunctions of Eq. (6.5) with rigid boundary conditions are easily found since they correspond to two one-dimensional decoupled lattices. Inserting these solutions in Eqs. (6.2) we get the amplitudes at the bases. We notice that solutions of Eqs. (6.2) have well-defined symmetries not only along the base-stacking direction (hereafter referred to as parallel) but also in the transversal direction (hereafter referred to as perpendicular). We thus obtain four bands of electronic states of different symmetries:

Symmetric states

The unnormalized amplitudes at the base sites are given by $\psi_n^G = \psi_n^C = \sin(Kn)$ and the corresponding eigenenergies are

$$E(K) = \frac{1}{2} E_+(K) \pm \frac{1}{2} \sqrt{E_+^2(K) + 4t_q^2} \ , \tag{6.6a}$$

where $K = \pi k/(N+1)$ with $k = 1, 2, \ldots, N$ and $E_+(K) = t_\perp + 2t_\parallel \cos(K)$ is the electron dispersion relation in the one-dimensional lattice with on-site energies $t_\perp$ and hopping $t_\parallel$.

Antisymmetric states

In this case the unnormalized amplitudes are expressed as $\psi_n^G = -\psi_n^C = \sin(Kn)$ and the corresponding eigenenergies are

$$E(K) = \frac{1}{2} E_-(K) \pm \frac{1}{2} \sqrt{E_-^2(K) + 4t_q^2} \ , \tag{6.6b}$$

with $E_-(K) = -t_\perp + 2t_\parallel \cos(K)$.

Figure 6.2 shows HOMO and LUMO bands in the DBL model, according to Eqs. (6.6a) and (6.6b). Here we take $t_\perp = 0.037\,\text{eV}$, $t_\parallel = 0.37\,\text{eV}$, and $t_q = 0.74\,\text{eV}$. The first value was suggested by Klotsa *et al.* in Ref. [45] as a SPARTAN result taking into account the weak overlap across the hydrogen bonds within the Watson-Crick pairs. The rest

of hoppings were proposed by Cuniberti *et al.* in Ref. [44] to reproduce experimental I-V curves [118]. Furthermore, they are within the range of values obtained by chemical quantum calculations [135, 145].

The electronic amplitudes at the backbone and base sites are also indicated on Fig. 6.2. Note that Eq. (6.2d) reduces to $\phi_n^s = (t_q/E)\,\psi_n^s$ in the case of the uniform DNA. Therefore, the amplitudes ψ_n^s and ϕ_n^s have the same sign for the LUMO band states, because $E > 0$, and opposite signs for the HOMO band states, since $E < 0$.

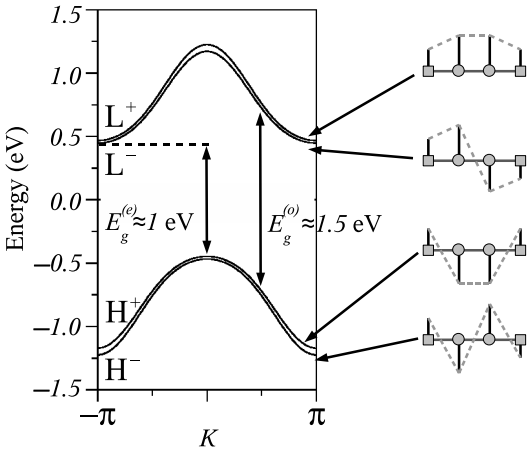

Figure 6.2. *HOMO ($H^{\pm}$) and LUMO ($L^{\pm}$) bands within the uniform ladder DBL model. The right plot shows schematically the symmetries of the wave-functions in the perpendicular direction. The squares and circles represent the backbone and bases sites, respectively. Electronic and optical gaps are indicated by vertical arrows.*

In view of these results, since the electronic gap and the direct optical gap do not coincide, the band structure within the DBL model might lead to an indirect band semiconducting behavior for DNA molecules.

6.3.2. SL model: direct band gap semiconductor

In contrast to the uniform case, the symmetry of wave functions along the perpendicular direction is broken if hoppings are different along the two strands, which is the case we consider within the SL model. Nevertheless, a closed expression for the dispersion relation

can also be obtained analytically:

$$E(K) = \overline{E}_+(K) \pm \sqrt{\overline{E}_-^2(K) + t_\perp^2} \ , \tag{6.7}$$

where for brevity we have now defined

$$\overline{E}_\pm(K) = \frac{1}{2}\left[E_G(K) \pm E_C(K)\right] \ ,$$

with $E_G(K) = \varepsilon_G + 2t_{GG}\cos(K)$ and $E_C(K) = \varepsilon_C + 2t_{CC}\cos(K)$.

Parameters of the SL model are chosen to fit *ab-initio* band structure calculations. To this end, we compare density functional calculations from Ref. [157] and the band structure obtained from Eq. (6.7). The best fitting parameters are: $\varepsilon_C = -0.75\,\text{eV}$, $\varepsilon_G = -1.85\,\text{eV}$, $t_{CC} = -0.105\,\text{eV}$, $t_{GG} = 0.047\,\text{eV}$, and $t_\perp = 0.917\,\text{eV}$. Figure 6.3 shows the obtained band structure for poly(G)-poly(C) DNA. In this case hoppings along the two strands, t_{CC} and t_{GG}, have opposite signs which results in a direct band gap.

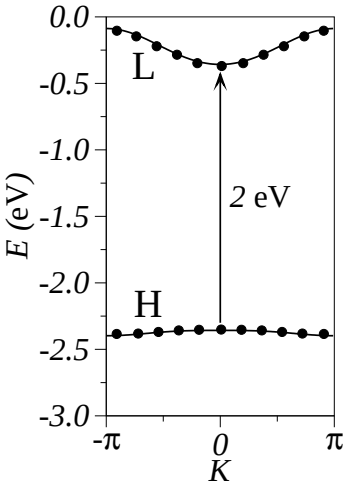

Figure 6.3. *HOMO (H) and LUMO (L) bands in poly(G)-poly(C) DNA. Solid lines correspond to Eq. (6.7) within SL model and solid circles are the energy values taken from density functional calculations in Ref. [157].*

6.4. Interband optical transitions

The solutions presented in the previous section will be the starting point to calculate the optical absorption coefficient due to interband transitions in DNA molecules. To

simplify the calculations, we will restrict ourselves to zero temperature and assume that the lower (HOMO) band is full and the higher (LUMO) band is empty. Under these assumptions, the absorption coefficient due to interband transitions is given by the Fermi golden rule as

$$A(\hbar\omega) \propto \sum_i \sum_f |\langle i|\widehat{e}\cdot\vec{r}|f\rangle|^2 \delta(E_f - E_i - \hbar\omega) \ , \tag{6.8}$$

where i and f run over the states of the HOMO and LUMO bands, respectively. Here $\widehat{e}$ is the unit vector along the polarization direction of the incoming electromagnetic plane wave.

We then focus on the square of the optical transition matrix elements $F_{ij} = |\langle i|\widehat{e}\cdot\vec{r}|f\rangle|^2$ as it determines the selection rules for the optical transitions. The δ-function in Eq. (6.8) is replaced by a square-box function of width 10 meV to take into account the spectral resolution. For the sake of clarity, we now discuss separately the two independent polarizations of the incoming field: perpendicular and parallel polarization with respect to the stacking direction of the molecule.

6.4.1. DBL model

Perpendicular polarization

The optical transition matrix elements reduce to

$$F_{if} \propto \left| \sum_{n=1}^{N} \left(\psi^+_{n,i}\,\psi^-_{n,f} + \psi^-_{n,i}\,\psi^+_{n,f} \right) \right|^2 \ . \tag{6.9a}$$

Thus we come to the conclusion that the symmetry in the perpendicular direction of the initial and final electron states should be different. As a consequence, only $H^+ \rightarrow L^-$ and $H^- \rightarrow L^+$ transitions are allowed. Moreover, it is a matter of simple algebra to demonstrate that

$$F_{if} \propto \delta(K_i - K_f) \ , \tag{6.9b}$$

namely only vertical transitions in K-space are allowed. We will discuss this issue in more detail below.

Parallel polarization

A similar calculation for parallel polarization yields

$$F_{if} \propto \left| \sum_{n=1}^{N} \left(\psi_{n,i}^{+} \psi_{n,f}^{+} + \psi_{n,i}^{-} \psi_{n,f}^{-} \right) n \right|^2 . \tag{6.9c}$$

In this case the initial and final electron states should have the same symmetry to give rise to an allowed transition. There is no simple closed expression for the optical transition matrix elements when polarization is parallel to the direction of base stacking, but it is not difficult to demonstrate that

$$\begin{aligned} F_{if} &\propto \left| \sum_{n=1}^{N} n \sin\left(K_i n\right) \sin\left(K_f n\right) \right|^2 \\ &\propto \left| \sum_{n=1}^{N} n \left[\cos\left[\left(K_i + K_f\right) n\right] - \sum_{n=1}^{N} \cos\left[\left(K_i - K_f\right) n\right] \right] \right|^2 \\ &\propto \left| \frac{1}{2} \left(\frac{1-(-1)^{k_i - k_f}}{\sin^2\left(\frac{K_i - K_f}{2}\right)} - \frac{1-(-1)^{k_i + k_f}}{\sin^2\left(\frac{K_i + K_f}{2}\right)} \right) \right. \\ &- \left. (N+1) \left[(-1)^{1+k_i-k_f} - (-1)^{1+k_i+k_f} \right] \right|^2 , \end{aligned} \tag{6.9d}$$

where again $K_{i,f} = \pi k_{i,f}/(N+1)$ with $k_{i,f} = 1, 2, \ldots, N$.

The previous expression is nonzero only if $k_i \pm k_f$ is odd. Then,

$$F_{if} \propto \left| \sin^{-2}\left(\frac{K_i + K_f}{2}\right) - \sin^{-2}\left(\frac{K_i - K_f}{2}\right) \right|^2 . \tag{6.9e}$$

Numerically it can be demonstrated that by increasing $|K_f - K_i|$ the optical transition matrix elements decrease rapidly. Therefore, the allowed optical transitions are almost vertical in K-space.

The fact that only vertical or almost vertical transitions in K-space are allowed has a strong impact on optical properties of DNA. In transport measurements (e.g, current-voltage experiments [118]) the electronic gap, which is given by the difference of the closest band edges, can be revealed (see Fig. 6.2 for illustration). In poly(G)-poly(C) DNA this gap is found to be of the order of 1 eV, and it is well described by the parameters set used above. However, the optical gap is larger due to exact or almost exact conservation of the quasi-momentum requirement (interaction with phonons is not considered here). This difference is clearly observed in Fig. 6.4(a), where we show the absorption spectra for

parallel and perpendicular polarizations. Results correspond to the uniform DBL model for a system of size $N = 500$, in which all site energies are set to zero, $t_{\parallel} = 0.37\,\text{eV}$, $t_{\perp} = 0.037\,\text{eV}$ and $t_q = 0.74\,\text{eV}$ (see Sec. 6.3.1). Note that the optical gap is about 1.45 eV for both polarizations, while the electronic gap is about 1.0 eV.

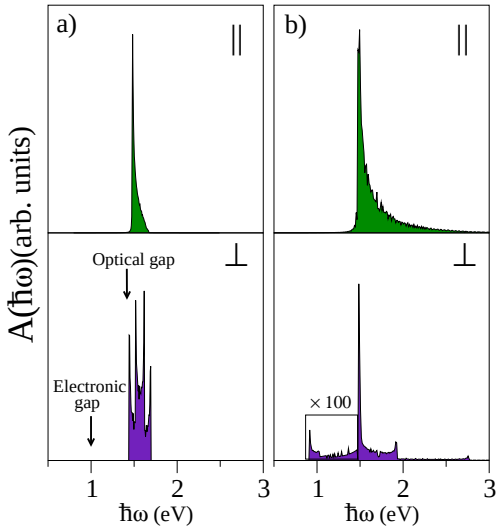

Figure 6.4. *Absorption spectra in (a) uniform and (b) nonuniform DBL models for $N = 500$ and parallel (upper panels) and perpendicular (lower panels) polarizations. The parameter used in (b) are reported in Sec. 6.4.1*

The width of the absorption band can be calculated exactly in the case of the perpendicular polarization. The energy of the lower absorption edge is obtained as the difference between L^- and H^+ bands at $K = \pi/2$. This difference is found to be 1.45 eV, in agreement with Fig. 6.4. Similarly, the energy of the upper absorption band edge is obtained as the difference of L^+ and H^- bands at $K = 0$, which gives 1.69 eV. The width of the absorption band due to interband optical transitions within the uniform model is about 250 meV.

As mentioned above, the uniform DBL model is not realistic, in the sense that all site energies are set to zero (see Sec. 6.3.1). To ascertain whether the results obtained for the uniform DBL model are relevant to understand optical transitions in real DNA, we have also considered a nonuniform DBL model by setting $\epsilon_G = 7.75\,\text{eV}$, $\epsilon_C = 8.87\,\text{eV}$ and the backbone site energy $\gamma_{BB} = (\epsilon_G + \epsilon_C)/2$ [45]. Note that these base energies are the base ionization potentials well established by molecular orbital calculations [134, 135]. On

the other hand $t_\perp$ and t_q were kept the same while two different intra-strand hoppings are considered now. Thus we keep the previous value $t_{GG} = t_\parallel = 0.37\,\text{eV}$ and we choose $t_{CC} = 4t_{GG}$ in order to take into account the different widths of the HOMO and LUMO bands obtained in Ref. [157]. In this situation, the site energy of the two strands are different and the symmetries of the states are broken. The corresponding absorption spectra for parallel and perpendicular polarizations are shown in Fig. 6.4(b). As expected, the absence of symmetric and antisymmetric states relaxes the selection rules and new interband optical transitions appear. However, the new absorption band below 1.45 eV (the optical gap in the uniform DBL) are several orders of magnitude weaker than the main band and it can therefore be neglected. As a consequence, the difference between the optical and electronic gap remains in the nonuniform DBL model.

6.4.2. SL model

As previously mentioned, the symmetry along the perpendicular direction is undefined if hoppings along the two strands are different. Therefore, any electronic transition from the HOMO band to the LUMO band is optically allowed for both polarizations. Figure 6.5 shows the absorption spectra in SL model for parallel (upper panel) and perpendicular (lower panel) polarizations. The optical gap is about 2.0 eV in both cases and coincides with the electronic gap (see Fig. 6.3).

6.5. Effects of disorder

In this section we consider the effects of the environment on the interband optical transitions described above. The disorder can originate from interactions with a random environment of solute ions around the DNA molecule. We restrict ourselves to static disorder as we consider the $T = 0\,\text{K}$ case and the molecule is supposed to be embedded into a glassy host.

6.5.1. Disorder in backbone energies

In the case of the DBL model we propose to include the environment effects in the outer part of the molecule, the backbone. Therefore we vary the backbone site energies

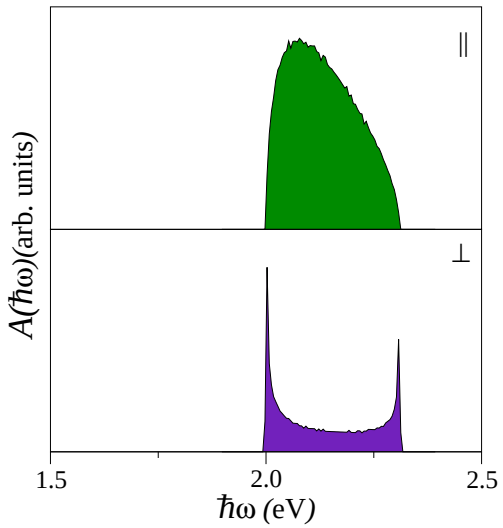

Figure 6.5. *Absorption spectra within the SL model for parallel (upper panel) and perpendicular (lower panel) polarizations for* $N = 1000$ *and parameter set given in Section 6.3.2. In both cases the optical gap of* 2.0 eV *is equal to the electronic gap.*

γ_n^s in the DBL model as (see Fig. 6.1):

$$\gamma_n^s = \gamma_{BB} + \Delta\gamma_n^s$$

where γ_{BB} is the unperturbed value of the backbone energy while $\Delta\gamma_n^s$ are stochastic variables generated by a box probability distribution with zero mean value:

$$\mathcal{P}(\Delta\gamma_n^s) = \frac{1}{2w}\,\theta\left(w - |\Delta\gamma_n^s|\right) \ , \tag{6.10}$$

where θ is the Heaviside step function and the parameter w is the halfwidth of the uniform probability distribution. Despite having defined the standard deviation σ as the magnitude of disorder in Chap. 2, hereafter we will use this term referring to w when dealing with the uniform probability distribution. Notice the proportionality between this two parameters $\sigma = w/\sqrt{3}$.

Figure 6.6 shows the absorption spectra for two different magnitudes of the backbone disorder: $w = 0.25$ eV and $w = 0.50$ eV in the nonuniform DBL model. The left panel shows the corresponding density of states (DOS). At moderate disorder ($w = 0.25$ eV) the electronic gap is still open and the corresponding absorption spectrum broadens as

compared to the case of the homogeneous DNA discussed in the previous section. Note that the absorption edge for perpendicular polarization is not sharp, reflecting the relaxation of the optical selection rules. As the magnitude of disorder increases ($w = 0.5\,\mathrm{eV}$) the electronic gap closes, as the left panel of Fig. 6.6 demonstrates. The effect is much more pronounced for the parallel polarization.

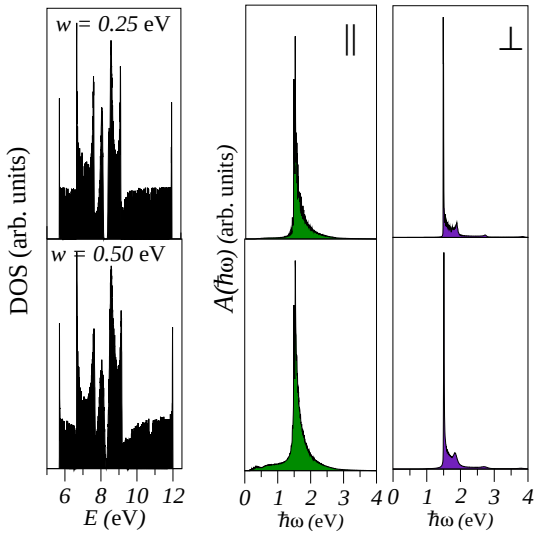

Figure 6.6. *Left panels show the* DOS *for two different magnitudes of backbone disorder indicated on each plot. The corresponding absorption spectra for parallel (middle panels) and perpendicular (right panels) polarizations are also shown. Each curve comprises the average over* 200 *realizations of disorder for* $N = 200$.

6.5.2. Disorder in base energies

Random interactions with solute ions and water molecules can affect not only the backbone but also the base molecules. In a similar way as we already did with the backbone energies, we account for these interactions by considering random base energies uniformly distributed within a box of halfwidth w and centered around ε_G or ε_C, depending on the strand [see Eq. 6.10]. Figure 6.7 shows the absorption spectra for synthetic poly(G)-poly(C) DNA within the SL model. The figure demonstrates that the absorption band edge remains almost unchanged for perpendicularly polarized light.

We stress that absorption spectra for the parallel polarization are qualitatively different

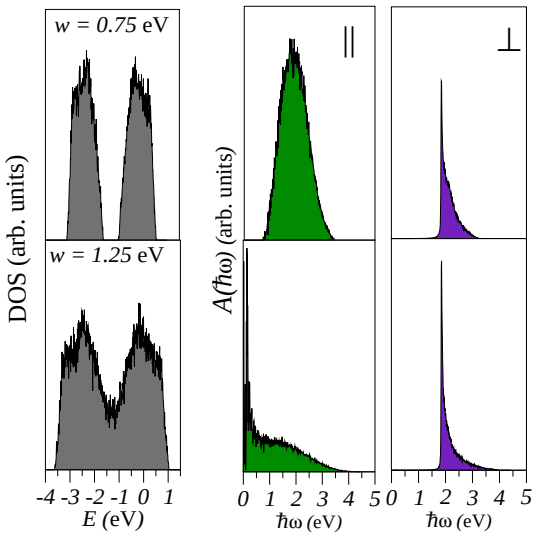

Figure 6.7. *Left panels show the* DOS *for two different magnitudes of disorder in the base energies indicated on each plot. The corresponding absorption spectra for* $N = 50$ *and parallel (middle panels) and perpendicular (right panels) polarizations are also shown. Each curve comprises averages over* 1000 *realizations of base disorder.*

for disorder introduced in the backbone or the base energies. In the former case the lower energy edge of the spectrum remains rather sharp by increasing the magnitude of disorder (see Fig. 6.6), while in the latter this feature disappears, giving rise to highly contributing optical transitions at very low energies (see Fig. 6.7).

6.6. DNA-helix conformation

Both considered models neglect the double helix geometry of the DNA molecule. However, the spatial arrangement of bases has been demonstrated to be crucial for transport properties in the presence of the perpendicular electric field [24]. In addition it can also be relevant when dealing with optical dipole moments of the electronic transitions. To improve the analysis, we consider the double helix structure of DNA molecules in both models.

In the case of the DBL model we propose the twisted DBL model as a set of four helices. The inner layer is composed by the traditional double helix structure of DNA bases and

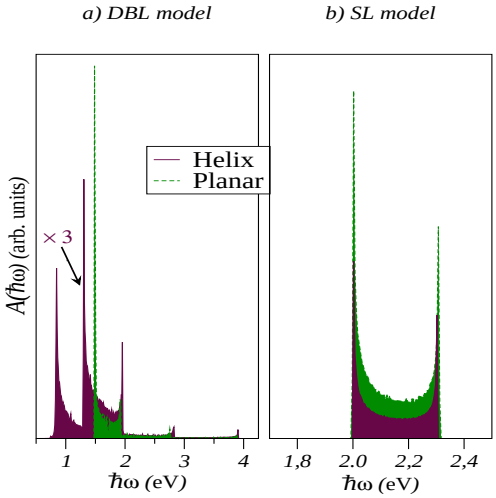

Figure 6.8. *Absorption spectra for perpendicular polarizations within the planar ladder (dashed line) and the twisted ladder (solid line) in (a) DBL ($N = 500$) and (b) SL ($N = 1000$) models.*

the outer one, corresponding to the backbone sites, arranged in the same geometry. The coordinates of the bases along both strands can be set then as

$$x_n^s = R\cos\left(\tfrac{2\pi}{T}n + \beta_s\phi_0\right),\ y_n^s = R\sin\left(\tfrac{2\pi}{T}n + \beta_s\phi_0\right),\ \ z_n^s = vn\ , \tag{6.11}$$

where $n = 1, \ldots, N$ and $s = C, G$. Here $\beta_C = +1$ and $\beta_G = -1$. We consider the B-form of the DNA with the following parameters of the double helix: radius $R = 1\,\text{nm}$, distance between the bases along the stacking direction $v = 0.34\,\text{nm}$ and full twist period of 10 base pairs, *i.e.* $T = 10$. Finally, we set $\phi_0 = \pi/3$, so that the relative phase difference between the helices is $2\phi_0 = 2\pi/3$, and the minor groove is one half of the major one. The backbone sites coordinates are set in the same way used for the bases but assuming a larger radius, $3R$. Needless to say that in the case of the twisted SL model the outer layer containing the backbone sites is neglected.

Despite the differences between both models, the helical conformation of the DNA strands results in the same unusual selection rules for interband optical transitions in the case of perpendicular polarization [158]. Assuming for simplicity the uniform case of both models, the wave functions have well-defined symmetries not only along the base-stacking direction but also in the perpendicular direction. These symmetries give rise to selection rules for the electron momentum. It is then a matter of simple algebra to demonstrate

that [158]

$$F_{if} \propto \frac{\sin^2(\,|K_i \pm K_f| - 2\pi/T\,)}{(\,|K_i \pm K_f| - 2\pi/T\,)^2} \sim \pi\,\delta(\,|K_i \pm K_f| - 2\pi/T\,)\;. \tag{6.12}$$

Thus, the harmonic modulation of dipole moments brings in the additional effective momentum $2\pi/T$, which changes the selection rule from that conserving the true total momentum [see Eq. (6.9b)] to the conservation of the sum of the total and the effective momenta.

The main difference between the two considered models occurs for perpendicular polarization, while the absorption spectrum for parallel polarization remains unchanged. In the latter case the height of the absorption spectrum is reduced by considering the helix conformation as compared to the planar case. The reduction is due to the fact that dipole moments are rotating around the molecule axis as one moves along this axis, so roughly half of them are perpendicular to the field and do not interact with it. Therefore we will focus on the impact of the helix conformation on the optical absorption under perpendicular polarization. In such a situation the strongest transitions appear to be indirect in K-space for both models. However, due to the dependence of selection rules on the energy dispersion of the bands, the absorption band width is modified in a different way for each model, see Fig. 6.8. In particular the absorption band broadens because of the energy structure being indirect for the DBL model, while for the SL model the opposite effect is found. Moreover the amount of broadening(shrinking) also depends on the model parameters: the smaller are the effective masses at the bottoms (tops) of the bands the larger it is. Figure 6.8 shows the results for the nonuniform DBL and SL models, with the same set of parameters used in previous sections.

6.7. Experimental challenge

In this section we get into the experimental challenge of measuring the absorption coefficient in the visible region of poly(G)-poly(C) chains. We also point out the steps to be followed in the procedure, as well as the difficulties that should be taken under consideration. First of all, we discuss the quality of the commercial poly(G)-poly(C) DNA product used in conductivity experiments, and propose a single-stranded DNA sequence specifically designed to conform a segment of double poly(G)-poly(C) DNA helix. In order to assure that our designed sequence conforms the desired structure, we will be dealing with

two other DNA sequences used as compositional and structural controls. The sample of interest, in comparison with the control sequences, will be characterized by means of polyacrylamide gel electrophoresis (PAGE). The composition of the samples will be studied in denaturing gels while their structure will be described by their migration in native gels. Different annealing and solution conditions, as well as DNA concentration of the samples, will be considered since these might affect their folding properties. After this characterization we will theoretically estimate the most favorable samples and experimental conditions to observe the optical transitions predicted in previous sections.

6.7.1. Sample design

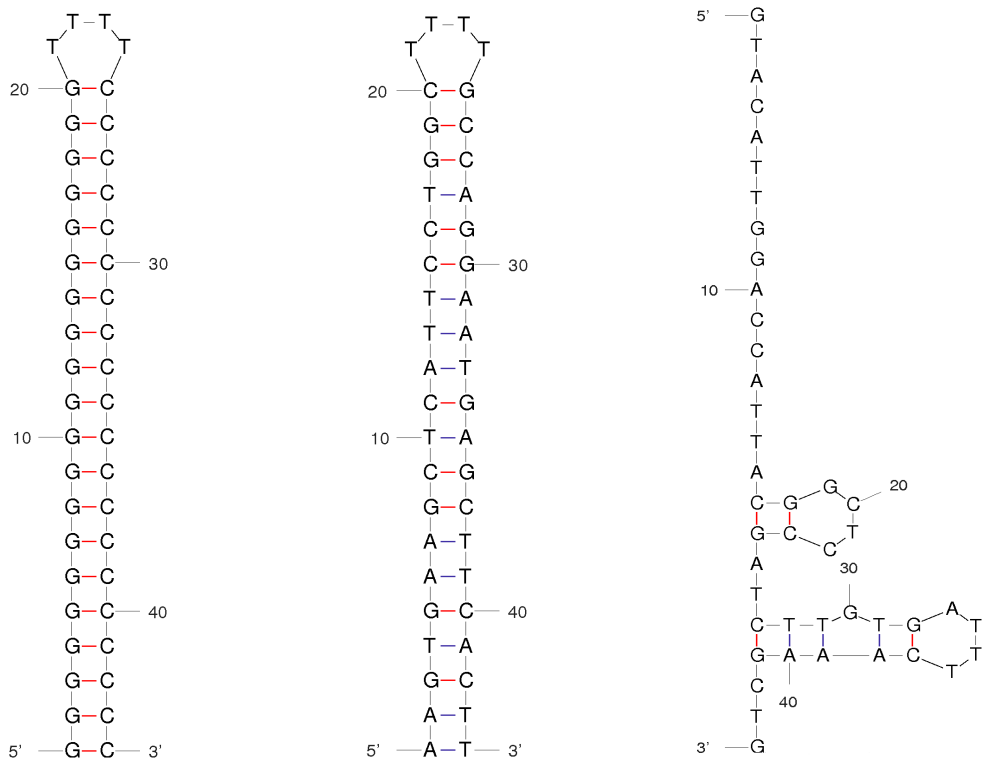

Figure 6.9. *Schematic figure of the most probable conformation of the DNA sequences (GC), (R) and (P) displayed in this order from left to right.*

In order to perform an experimental study of the already theoretically predicted optical absorption coefficient, the first point to be considered is the DNA samples to be used. As we previously mentioned, reviewing the electrical measurements on DNA molecules,

different results are found [114–127]. The reasons to explain these contradictory evidences are usually related to the specific DNA sequence, environment conditions and also contact effects [159]. However, the characterization of the DNA samples used in the experiments, which hardly ever appear explicity in the references, is another important issue to think about. This seems to be a crucial question, in particular when dealing with uniform poly(G)-poly(C) because of the difficulty to synthesize long homogeneous DNA strands, specially consistent of guanine [160–162]. In this sense, it was already probed the existence of structural defects in the commercial preparation of poly(G)-poly(C) used in electrical conductivity studies [163]. Due to these synthesis problems it is important to deal with specific experimental tools to allow for a proper control of the characterization of the poly(G)-poly(C) DNA samples. As already mentioned, in our case we use two DNA sequences designed as compositional and structural controls whose properties are to be compared to those of the one of interest, denoted hereafter as (GC).

The three initial samples under consideration are single-stranded DNA chains consistent of 44 nucleotides and they were provided by *Integrated DNA Technologies* (IDT) after a standard desalting procedure but no purification (see the IDT website for further details [164]). The longest G-homopolymer the company accepted to synthesize to get relevant yield was 20 nucleotides long. Therefore, our main sample will be designed to contain 20 stacked GC base pairs. This will be revealed later as a limiting factor for the optical absorption coefficient observation. In particular these are the samples which we will be considering hereafter:

- *GC sample* (GC):

  5'GGGGGGGGGGGGGGGGGGGGTTTTCCCCCCCCCCCCCCCCCCCC3'.

  This sample will be the one of our interest. It is consistent of a sequence of bases G, C, and T arranged in the above given order. Due to the GC complementarity, this single-stranded DNA sequence is expected to conform a hairpin structure with high probability. In such a case, the T segment forms a loop while the GC stacked pairs conform a segment of double poly(G)-poly(C) DNA helix. Since the loop contains only 4 bases, its effects on the absorption spectrum might be negligible as compared to those produced by the paired GC-segment.

- *Random sample* (R):

  5' AAGTGAAGCTCATTCCAGGCTTTTGCCTGGAATGAGCTTCACTT 3'.

  This will be the structural control sample. It is consistent of a sequence of the four bases G, C, T, and A arranged in the above shown order. As in (GC), a T loop is included at the center of the sequence, while the initial and the final segments are designed to be complementary and contain a random sequence of the four DNA bases. Due to this design, the most stable structure for (R) is also a hairpin and therefore, it will behave similarly to (GC) in a structural study. Nevertheless, when dealing with optical absorption measurements only (GC) is expected to give rise to relevant results regarding collective excitations.

- *Permuted sample* (P):

  5' GTACATTGGACCATTACGGCTCCGATCTTGTGATTTCAAAGCTG 3'.

  This will be the compositional control sample. It is consistent of a sequence of the four bases G, C, T, and A arranged in the above given order. As such a control, it is designed with the same base composition than (R) but with no order specification in the sequence. This means that *a priori* no T loop and no complementary segments are included in the sequence. For this reason, (P) is not expected to conform any specially stable structure so that it can be differentiated of a hairpin in a structural study. However, in a compositional study, and due to the great similarity of the four bases molecular weight, (P) should behave in the same way than (R) and (GC). This will be useful to assure the right synthesis of the sequence (GC).

Figure 6.9 shows the most stable structures for these sequences according to the DNA/RNA folding algorithm implemented by the *Mfold* web-server [165].

6.7.2. Sample characterization

The sample characterization consists of two different analyses, the compositional and the structural one [a].

[a] The sample characterization was carried out by the author in the *DNA NanoTech* laboratory at Duke University (NC-USA).

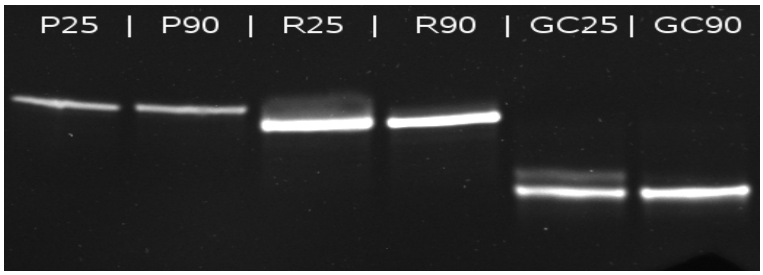

Figure 6.10. *Autoradiograph of a formamide-urea denaturing gel, where mobility is expected to depend on the sequence length (molecular mass). The lanes considered in the gel are labeled according to the loaded sample (P), (R) or (GC) and the temperature at which they were loaded 25° C or 90° C.*

Compositional study

Once we get the three DNA samples provided by IDT, we proceed with its purification in order to separate the full length sequences of the whole synthesis. To this end, we use a standard denaturing procedure based on urea-polyacrylamide gel electrophoresis [166]. In these gels all kinds of structure have tendency to disappear in such a way that DNA samples are expected to behave as random coils and to migrate as single, discrete bands with mobilities depending only on the molecular mass. Thus, in our case the three samples should get the same final position in the gel due to their same sequence length and the highly similar molecular weight of the four DNA bases.

Figure 6.10 shows an analytical denaturing gel where 6 lanes have been considered, two for every type of sequence. One is loaded directly with the sample at room temperature 25°C and the other is loaded after heating it up to 90°C. The heating process should enhance the DNA melting of all base pairing or DNA folding. After running this gel we find single bright bands in all cases. Keep in mind that the appearance of bright discrete bands in the gel can only be produced by a unique product of every sample, while broader bands are typical when molecules of different length or conforming different structures coexist in the same sample. This latter situation seems to be revealed by the shadowed regions in the lanes where the samples (R) and (GC) were loaded directly at room temperature. However, they disappear after the heating process. Therefore, in view of Fig. 6.10, we claim that every DNA sample behaves as a unique DNA product.

On the other hand, and contrary to what expected, we observe that every sample behaves differently in the denaturing gel, see the different heights which the bands of every sample appear at in Fig. 6.10. Our explanation for the different mobilities of the three samples is that the most probable folding of (R) and (GC), being a hairpin (see Fig. 6.9), is such a highly stable structure that it is inclined to be partially conformed due to the high bases complementarity even in a denaturing gel. Assuming that the hairpin structures expected for (R) and (GC) are fully or partially folded, their long helical stems could move along the gel matrix easier than the unstructured (P) sample [167] and therefore, they would reach a lower final position in the gel. Moreover, being the GC pairs much more stable than the AT ones, the complementary bases recognition in (GC) is easier and even longer helical stems can be conformed. Thus, (GC), with the highest mobility in the gel, gives rise to the lowest band in the autoradiograph.

The same behavior of the three DNA samples was also observed even in a more denaturing gel (not shown here for brevity) with a higher urea concentration [168]. This confirms the high and unusual stability of the structures conformed by (R) and (GC).

Finally, since the compositional analysis by way of denaturing PAGE has not confirmed the length of the sequences we are dealing with, and due to the problematic synthesis of DNA-homopolymers already reported [160–162], we use a mass spectrophotometer (Voyager-DE PRO Biospectrometry Workstation by Applied Biosystems) to determine if the DNA product provided by IDT actually contains DNA molecules of 44 nucleotides. If the synthesis failed, the molecules might be shorter and therefore its molecular weight would be lower. It is to be mentioned that previously to this mass measurement, it is neccesary to perform a carefully desalting of the samples in order to avoid the salt contribution in the determination of the molecular weight of the DNA molecules. Figure 6.11 shows the mass spectra of the three DNA samples which clearly reveal a well defined peak close to the calculated molecular weight for all of them ($M_{(GC)} = 13552.7\,\text{amu}$ and $M_{(R)} = M_{(P)} = 13512.8\,\text{amu}$) confirming that our samples contain DNA molecules 44 nucleotides long.

Structural study

So far we have proven that our three samples are 44 nucleotides long and (GC) and (R) seem to spontaneously collapse to unusually stable conformations in view of their behavior in denaturing gels. In particular, according to the DNA/RNA folding algorithm *mfold*,

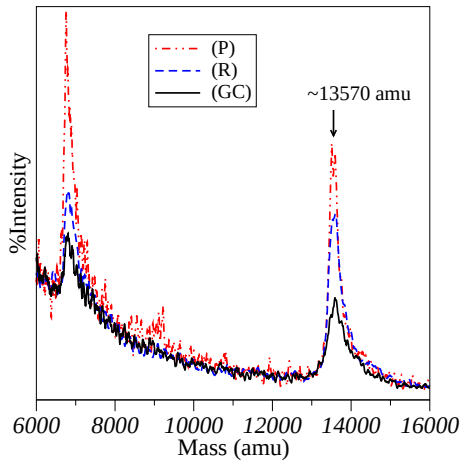

Figure 6.11. *Mass spectra of the three DNA samples under consideration. All spectra reveal a well defined peak close to the calculated molecular weight for all samples* $M_{(GC)} = 13552.7\,\text{amu}$ *and* $M_{(R)} = M_{(P)} = 13512.8\,\text{amu}$.

these stable foldings might well be hairpin structures for both sequences. Our interest now is to elucidate if the sample of main interest (GC) actually conforms the expected GC-hairpin and if it can conform other different structures depending on the type of annealing, the surrounding solvent or the DNA concentration. For this structural study we use native or nondenaturing PAGE [169]. The native gels of this procedure allow for the formation of DNA structures in such a way that the distribution of DNA mobilities is influenced by the conformational collapse unique to each sequence, with compactly folding molecules tending to migrate faster in the gel. Therefore, we do not expect now any different behavior between (GC) and (R), which are expected to conform hairpin structures but both, being long helical stems, should migrate faster than (P).

Firstly we study the effect of the annealing conditions on the folding properties of our samples. We start describing the types of annealing we will be considering in our experiments:

- *Quenching* (Q): the sample is heated up to 100°C in boiling water and cooled abruptly in ice. Thus, it will conform the more accessible structure since the annealing is almost instantaneous.

- *Slow annealing* (S): the sample is heated up to 100°C in boiling water and afterwards

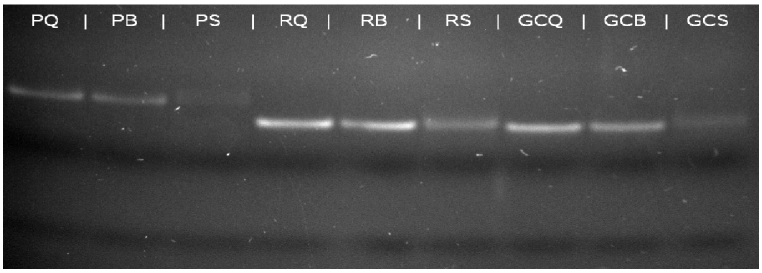

Figure 6.12. *Autoradiograph of a nondenaturing gel at 2mM Mg^{2+} concentration. Every lane is loaded with* $10\mu l$ *of a DNA solution* $1\mu M$ *DNA and no* Mg^{2+}*. Every label denotes the loaded sample in each lane (P), (R) or (GC) and the type of annealing applied in each case (Q), (S) or (B).*

it is cooled simultaneously with the heated water at room temperature till both of them reach 25°C. This process can take one hour and several complicated structures can appear.

- *Intermediate annealing* (B): the sample at 100°C is let on the laboratory bench at room temperature during 4 min. This annealing takes such a time that nontrivial structures can be conformed but not as complicated as in the procedure (S).

Our first experiment is focused on studying the influence of the annealing procedure on the structure conformation of the DNA samples. In particular we consider a native gel at 2mM Mg^{2+} concentration, and we run 9 lanes, three for every sample at which a different kind of the above reported annealings is applied. In Fig. 6.12 it is shown the resulting gel after running these 9 lanes which were loaded with 10μl of a solution of 1μM DNA and no Mg^{2+}. Figure 6.12 shows well defined bright discrete bands for the three DNA samples revealing that all of them are conforming a single structure. As expected, there is a difference in the position of the band for (P) respect to the others which were designed to conform hairpin structures. It is worth mentioning that in the native gels (GC) and (R) behave identically because of conforming the same structure. As a last remark, notice that in all samples the slow annealing seems to produce much less brilliant bands which might be a consequence of some kind of DNA degradation.

After demonstrating that different annealing procedures do not give rise to new structures for our samples, we analyze the effect of the presence of Mg^{2+} in the solution of the

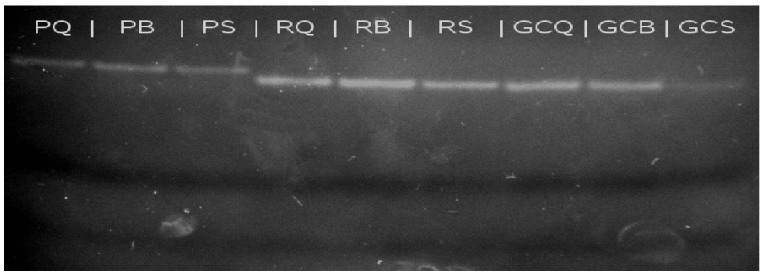

Figure 6.13. *Autoradiograph of a nondenaturing gel at 10mM Mg^{2+} concentration. Every lane is loaded with* $10\mu l$ *of a DNA solution* $1\mu M$ *DNA and* $10mM$ *Mg^{2+} Mg. Every label denotes the loaded sample in each lane (P), (R) or (GC) and the type of annealing applied in each case (Q), (S) or (B).*

DNA samples. In this regard, it is proven that this might enhance a variety of possible DNA foldings depending on the Mg^{2+} concentration [170]. Therefore, we consider now another native gel at 10mM Mg^{2+} concentration, and in the same way as before we run 9 lanes, three for every sample annealed through a different process. In particular, every lane contains 10μl of a solution of 1μM DNA and 10mM Mg^{2+}. In Fig. 6.13 the resulting gel is displayed. The bands appearing in the gel of Fig. 6.13 behave very similarly to those of Fig. 6.12 and the conclusions discussed in the preceding paragraph are confirmed by this new experiment. This means that the presence of Mg^{2+} in the DNA solution does not affect their structural properties, though it indeed reduces the DNA degradation produced by the slow annealing process.

According to all these data, it seems that our sequence of interest (GC) is conforming a well behaving structure with a well defined length and which hardly depends on the solution or annealing conditions. Moreover, in a structural study it behaves similarly to (R) but different from (P) which means that, keeping in mind the expected structures for the three samples (see Fig. 6.9), (GC) and (R) conform stable hairpin structures with higher mobilities inside the gel matrix than the unstructured (P) folding. Therefore, our claim is that our GC-hairpin, containing 20 stacked base pairs of a double poly(G)-poly(C) DNA helix, is a proper sample to test experimentally our theoretical calculations of the optical absorption coefficient of poly(G)-poly(C) DNA.

Respect to the optical measurements it is well established that optical transitions are more intense when considering more concentrated DNA samples [171]. Thus, an analysis

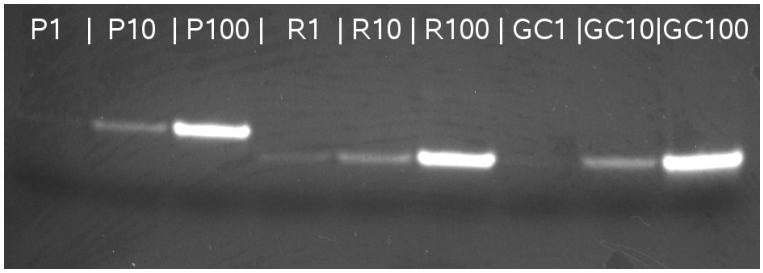

Figure 6.14. *Autoradiograph of a nondenaturing gel at 2mM Mg^{2+} concentration. Every lane is loaded with* $10\mu l$ *of a DNA solution of* $1\mu M$*, and* $10\mu M$ *and* $100\mu M$ *DNA and* $10mM$ *Mg^{2+}. Every label denotes the loaded sample in each lane (P), (R) or (GC) and its DNA concentration* $1\mu M$*,* $10\mu M$ *and* $100\mu M$*. The intensity of the discrete bands increase by considering higher concentrated DNA samples as expected*

of the structural stability of increasing DNA concentrated samples in a native gel is in order. We consider then another native gel at 2mM Mg^{2+} concentration, and we load our DNA samples after an intermediate annealing procedure. In this case we run 9 lanes, three for every sample with a different DNA concentration 1μM, 10μM and 100μM respectively. The Mg^{2+} concentration in all samples is 10 mM. In Fig. 6.14 the resulting gel is displayed. Once again we find well defined discrete bands even for a high concentration of DNA so the hairpin structure is very stable even in a highly concentrated sample. Indeed, we confirmed this result even for a (GC) sample with a DNA concentration of 400μM. Therefore the optical absorption coefficient might be measured at least in (GC) samples with $400\,\mu$M concentration of DNA.

6.7.3. Experimental proposal to measure the optical absorption coefficient

Once we have demonstrated that our designed (GC) sample conforms a very stable structure, and according to our structural control, it is a hairpin structure, we make a measurement of its absorption spectrum in the visible region with the Varian Cary 100 UV-Vis spectrophotometer. Notice that despite the fact this spectrophotometer takes excellent static and dynamic measurements of sample concentrations with a resolution at

zero level of absorbance of 10^{-4} AU, it may occur that for our current objective such a resolution is not enough to detect the optical transition we are searching for. In particular our measurement is performed on a DNA solution of 180μl of our highest concentrated (GC) sample containing a $400\,\mu$M concentration of DNA and no other buffer in the solution, since the presence of Mg^{2+} seems not to affect this sample's folding properties. We load the cuvette of the spectrophotometer with such a solution after an intermediate annealing process and we compare the results with the blank provided by H_2O. Under these conditions no signal was observed in the visible region.

This experimental result can be understood by estimating our theoretical predictions for the optical absorption coefficient of the particularly considered poly(G)-poly(C) sample.

To this end, first of all, we should keep in mind the Beer's law to calculate this coefficient in a solution of DNA molecules [171]:

$$I(z) = I(0)\; e^{-Az}, \tag{6.13}$$

where z represents the light incident direction and A is the absorption coefficient of the sample. The exact expression to calculate this coefficient in S.I. units reads [171]

$$A(\hbar\omega) = \frac{4\pi^2\omega n_{\rm mol}}{c}\sum_i\sum_f |\langle i|\widehat{e}\cdot\vec{r}|f\rangle|^2\delta(E_f - E_i - \hbar\omega)\,. \tag{6.14}$$

Here n_{mol} is the volume density of the absorbing DNA molecules and c is the speed of light in vacuum. Spectrophotometric measurements of the absorption coefficient are usually expressed in absorbance units defined as $A_{AU} = -\log I(z)/I(0)$. Notice that, as we already mentioned in the previous section, Eq. (6.14) confirms that the higher concentrated the DNA solution is, the stronger the visible optical transitions are expected to be. On the other hand it is worth mentioning that the intensity of these optical transitions is also directly proportional to the length of the DNA molecules according to our numerical calculations (not shown here for brevity).

In order to compare our theoretical estimations with the measurement performed by the Varian Cary 100 UV-Vis spectrophotometer, we should take into account that this instrument deals with unpolarized light beams which is not the case considered by our theoretical calculations so far. Thus, the polarization of the light is also a factor to be taken into account in the experiment. The optical absorption of polarized light was already analyzed in Sec. 6.6 for the helicoidal conformation typical of DNA. For the case

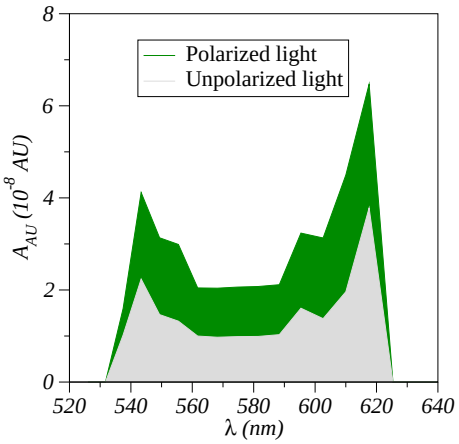

Figure 6.15. *Theoretical absorption coefficient for unpolarized and polarized light in the perpendicular direction within the twisted DNA-ladder model for a DNA solution of 180μl of poly(G)-poly(C) molecules 20 base pairs long and concentration 400μM.*

of unpolarized light the optical absorption coefficient can be calculated using the unitary vector for the electric field as $\widehat{e} = (\cos\theta, \sin\theta\cos\phi, \sin\theta\sin\phi)$ and averaging the matrix elements of the optical transitions over all possible directions of the field, namely $\theta \in [0, \pi]$ and $\phi \in [0, 2\pi]$.

We check our theoretical predictions for a sample of 180μl of a DNA solution of poly(G)-poly(C) molecules 20 base pairs long and concentration 400μM to be directly compared with the measurement reported above. In Fig. 6.15 the absorption coefficient for the case of unpolarized and polarized light in the perpendicular direction is shown. The case of polarized light in the parallel direction gives rise to coefficient 6 orders of magnitude smaller and therefore, it is not relevant in our current study. In view of Fig. 6.15 we find that the intensity of the optical transitions we are dealing with is in the range of 10^{-8}AU for this kind of samples, which is four orders of magnitude lower than the accuracy of conventional spectrophotometers as the one used in the measurement. The polarization of the light only affects this order of magnitude in a factor smaller than two so it does not seem a crucial factor in this experiment, though it can indeed be taken into account. However, the main conclusion of these estimations is that harder efforts should be devoted to the preparation of the (GC) sample trying to get longer molecules and to

the study of its structural properties at higher concentrations. For example, if it could be managed to conform well behaving GC-hairpins containing 100 base pairs in a DNA concentration of 10mM DNA, the intensity of its interband transitions would theoretically reach values of 10^{-5}AU which could be experimentally detected. In any case, it is to be mentioned that, apart from the traditional spectrophotometers, these weak transitions might be detectable by modern *diode laser absorption spectrophotometry* technics where the signal to noise ratio is higher [172]. These set ups might manage accuracy levels of the order of $10^{-7} - 10^{-8}$AU which would be high enough to detect the absorbance produced by the DNA solutions under consideration.

6.8. Conclusions

We considered interband optical transitions in semiconducting synthetic DNA, such as the poly(G)-poly(C) DNA. In order to study the optical properties we used two different tight-binding models and parameter sets. We have demonstrated that both of them, which reproduced transport experiments [118] (DBL) or sophisticated *ab-initio* calculations [157] (SL) present different optical behaviors. Note that the fact of considering the backbone sites within a theoretical model is not the most important point. Indeed it can be demonstrated that the DBL model can be transformed to the SL model renormalizing the sites energies of the bases in a proper way [45, 46]. The crucial point then is the tight-binding parameters set and mainly, the signs of the intra-strand hoppings. In the literature the values for these hoppings are usually positive [135, 145]. However they should have opposite signs in order to reproduce the typical curvatures of the HOMO and LUMO bands obtained by *ab initio* calculations [157]. Because of this inconsistence we have shown how, by means of the analysis of interband optical transitions, it can be distinguished whether the synthetic poly(G)-poly(C) DNA behaves as a direct or indirect semiconductor and thus, which is the best theoretical description.

Furthermore, environment effects on the DNA molecules can be included by introducing disorder in both base and backbone levels. Thus, our study might be relevant in many different experimental situations but mostly in natural DNA which is always in liquid solution. Indeed there are two issues which could be modified to reproduce natural conditions, namely the distribution and the magnitude of disorder. Disorder reduces both optical and electronic gaps which, in principle, might provide a reasonable explanation of the observed

ohmic behavior of DNA conductivity in disordered aqueous environment [117].

We show that the helical confirmation of the DNA strands results in unusual selection rules for interband optical transitions in the case of perpendicular polarization of incoming light. Such transitions appear to be indirect in K-space. On these grounds, we demonstrate that the analysis of absorption spectra for parallel and perpendicular polarizations can provide valuable information on the DNA energy structure, the effective masses at the top and bottom of the bands and the value of the tight-binding parameters.

Although matrix elements of intra-molecule excitations are several orders of magnitude larger than those involving collective states [173,174], the intra-molecule transition energy of about 3.7 eV [174] observed in wet DNA is probably well above the absorption band edge for interband transitions. Thus, low-energy features in the absorption spectra due to interband transitions are relatively weak but well separated from the strong intra-molecule excitations, which suggests that they can be observed, although this could be challenging from the experimental point of view. In this regard, we discussed the most favorable conditions to experimentally observe the interband transitions theoretically studied in this chapter. We proposed the GC-hairpin as a promising poly(G)-poly(C) DNA sample to perform the optical experiment, see Sec. 6.7. However, the intensity of such transitions, which is under the accuracy of conventional spectrophotometers, must be enhanced by taking long DNA sequences or highly concentrated DNA samples.

Chapter 7

Current across DNA molecules assisted by molecular vibrations

In this chapter we study the incoherent transport in a DNA-ladder model at room temperature. While the static environment interactions are modeled by introducing a disorder perturbation in the base energies, its fluctuations are considered within a master equation approach based on a phonon-assisted hopping formalism. Experimental $I-V$ characteristics performed over dry DNA are reproduced, revealing a semiconducting behavior for synthetic DNA-homopolymers like the poly(G)-poly(C).

7.1. Introduction

As we already mentioned in Chaps. 5 and 6 electronic transport through DNA molecules attached to leads is an exciting topic. Biologists even claim the possibility of revealing and controlling damages in DNA by means of electrical currents (for an overview see Ref. [175, 176] and references therein). Far from this genetic interest, the efforts of this chapter will be focused on theoretically describing the variety of results on electrical transport through dry and wet DNA molecules [114–125,127]. The most promising experiments on this topic are those revealing the semiconducting behavior of DNA-homopolymers like the synthetic poly(G)-poly(C). Moreover it seems that solid theoretical arguments support this claim [44–46, 133, 148–153].

Our interest in this chapter is to get into a problem not so frequently studied: the effects of molecular vibrations of the environment on the electric current through DNA. In this regard it was reported in Ref. [177] that charge-hopping between the sites of G-traps in presence of charge-phonon interactions, results in a staircase structure of the $I-V$ characteristics. Moreover, the height of the steps of such a structure might provide relevant information about the strength of the electron-phonon coupling and the temperature of the system. A different work was performed in Ref. [178] where charge transport was studied considering electron-phonon coupling, as well as the fact that DNA vibrational modes are also coupled to the surrounding environment. In this reference two different DNA sequences were considered: the homogeneous ones such us the synthetic poly(G)-poly(C) DNA and a inhomogeneous (natural) sequences. For the former case, the main result is that the charge-vibration coupling enhance the zero-bias conductance at low temperatures, while its effects at large bias are very weak due to the quasiballistic transport through the extended states. For natural DNA however, all states are strongly localized and transport is dominated by inelastic processes by way of phonon-assisted hoppings which highly influence the conductance. These dissipative effects, comprising counter-ions and hydration shells, were investigated also in Ref. [179] by means of embedding the DNA molecule in a collection of harmonic oscillators. By allowing for electron-bath interaction, the electronic gap becomes temperature dependent. In this sense a crossover from tunneling to activated behavior at low voltages is observed by increasing the temperature in the strong electron-bath coupling limit. As a further step, in Ref. [47] these authors get into the analysis of the quality of the molecule-electrode coupling, claiming that it can modify

the order of magnitude of the current along DNA molecules. This is a well established claim in molecular electronics [180].

In order to model these clearly relevant environment effects on the charge transport of DNA molecules we will take two complementary approaches. On the one hand, a tight-binding ladder model [133] with disordered base energies is considered to describe the DNA electronic states arising when static environment interactions are present [45]. On the other hand, to take into account the fluctuating counterpart of these interactions, we propose a nonlinear master equation formalism [107, 181]. Temperature effects are included in this approach by means of phonon-assisted hopping between localized states.

7.2. DNA model

7.2.1. Hamiltonian description

We consider a ladder-like model [133] of the poly(G)-poly(C) DNA based on a tight-binding Hamiltonian within the nearest-neighbor approximation. This model was already studied in Chap. 6 where it was referred as simple ladder model. As before we assume that values of inter-base hopping parameters depend on the bases, describing it by the hoppings t_{GG}, t_{CC} and $t_{\perp}$. In the absence of disorder, site energies are ε_C and ε_G. Figure 7.1 represents a sketch of the DNA molecule attached to ideal contacts at both ends of the DNA molecule.

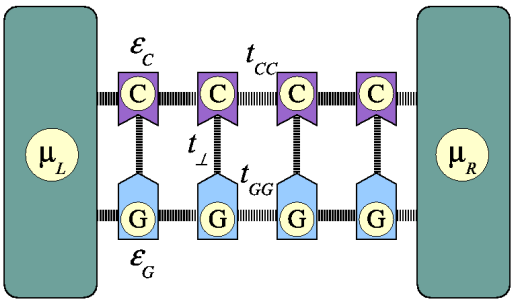

Figure 7.1. *Schematic view of a fragment of poly(G)-poly(C) DNA molecules, excluding the sugar-phosphate backbone, coupled to ideal leads.*

As we already did in Chap. 6 we can write down the equations for the electronic

amplitudes at the bases of this model as follows:

$$\begin{aligned}(E-\varepsilon_C)\,\psi_n^C &= t_{CC}\left(\psi_{n+1}^C+\psi_{n-1}^C\right)+t_\perp\psi_n^G\ ,\\ (E-\varepsilon_G)\,\psi_n^G &= t_{GG}\left(\psi_{n+1}^G+\psi_{n-1}^G\right)+t_\perp\psi_n^C\ .\end{aligned}\tag{7.1}$$

Here ψ_n^s denotes the electronic amplitudes, where $n=1,2,\dots N$ labels a base pair and the superscript $s=G,C$ refers to the two strands. In a poly(G)-poly(C) DNA molecule all base energies along each strand take the same value. In such a case closed expressions for the dispersion relation arising from Eq. (7.1) can also be obtained analytically with rigid boundary conditions, see Sec. 6.3.2:

$$E(K)=\overline{E}_+(K)\pm\sqrt{\overline{E}_-^2(K)+t_\perp^2}\ .\tag{7.2}$$

where the upper and lower signs correspond to the HOMO and LUMO states. For brevity we define $\overline{E}_\pm(K)$ in terms of the dispersion relations in each strand $E_G(K)=\varepsilon_G+2t_{GG}\cos(K)$ and $E_C(K)=\varepsilon_C+2t_{CC}\cos(K)$ as follows: $\overline{E}_\pm(K)=(1/2)\left[E_G(K)\pm E_C(K)\right]$, where $K=\pi k/(N+1)$ with $k=1,2,\dots,N$.

7.2.2. Nonlinear Pauli master equation

In vivo as well as in most of the experimental situations, environment effects on DNA properties seem to be crucial in view of the wide range of experimental results on DNA conductivity [159]. The static interactions of the surrounding solute molecules and ions with DNA molecule can be modeled by a random perturbation of the DNA base energies [45]: i. e. a uniform disorder distribution (see Sec. 6.5):

$$\mathcal{P}(\Delta\gamma_n^s)=\frac{1}{2w}\,\theta\left(w-|\Delta\gamma_n^s|\right)\ ,\tag{7.3}$$

where θ is the Heaviside step function and w is the halfwidth of the uniform probability distribution. This parameter will be referred to as magnitude of disorder hereafter, see Sec. 6.5

Notice that, in a similar way that for a 1D lattice, the localization properties of a DNA-ladder model strongly depend on the distribution and magnitude of disorder. It is well known that strong disorder localizes the electronic states in regions shorter than the system size suppressing the coherent transport along the lattice. However, there also exist environment fluctuations which cannot be captured by the static approach. In such a case

electron-phonon coupling can result in phonon-assisted hoppings between these localized states of different energy giving rise to an incoherent transport along the system. In the same way that in Sec. 4.2.2, we describe this incoherent mechanism by means of the following transition rates from the state ψ_μ (with energy E_μ) to the state ψ_ν (with energy E_ν) [107]:

$$W_{\mu\nu} = W_0\, S(|\Delta E_{\mu\nu}|)\, F(\Delta E_{\mu\nu}, T)\, \mathcal{I}_{\mu\nu} \ , \tag{7.4}$$

with $\Delta E_{\mu\nu} \equiv E_\mu - E_\nu$ and $\mu = 1, 2, \ldots, 2N$. The discussion about all contributions appearing in these transition rates can be found in Sec. 4.2.2, but notice that the spectral density function reads for our DNA-ladder model $S(|\Delta E|) = |\Delta E|/t_{GG}$ [107, 108].

Taking advantage of these expressions the process of charge transport through the DNA molecule can be modeled by way of a nonlinear Pauli master equation expressed in terms of the population P_μ of the eigenstate μ

$$\frac{dP_\mu}{dt}\Big|_{\text{DNA}} = \sum_{\nu=1}^{2N} [W_{\nu\mu}\, P_\nu\, (1 - P_\mu) - W_{\mu\nu}\, P_\mu\, (1 - P_\nu)] \ . \tag{7.5}$$

It is worth mentioning that to account for the Pauli exclusion principle a nonlinear term in the populations P_μ arises.

In order to calculate the electric current along the DNA molecule as a function of the applied bias to compare our results directly with experiments [118], new terms should be included in the previous master equation. They will take into account the transition probability between states associated to the DNA molecule and the contacts. The contribution of these transitions to the master equation are assumed to be of the form:

$$\frac{dP_\mu}{dt}\Big|_{\text{Leads}} = \Gamma_\mu^L (f_\mu^L - P_\mu) + \Gamma_\mu^R (f_\mu^R - P_\mu) \ , \tag{7.6}$$

being $f_\mu^{L,R}$ the Fermi distribution functions for the left and right leads:

$$f_\mu^{L,R} = \Big[1 + \exp\Big(\frac{E_\mu - \eta_{L,R}}{k_B T}\Big)\Big]^{-1} \ , \tag{7.7}$$

where k_B is the Boltzmann constant, and $\eta_L = E_F + eV$ and $\eta_R = E_F$ are the chemical potentials of the left and right contacts. E_F is the Fermi energy at equilibrium, taken to be in the middle of the homogeneous DNA band gap, which is the case for Au contacts [182]. The magnitudes $\Gamma_\mu^L = \gamma(|\psi_1^G|^2 + |\psi_1^C|^2)$ and $\Gamma_\mu^R = \gamma(|\psi_N^G|^2 + |\psi_N^C|^2)$ measure the coupling between leads and the eigenstate μ, the parameter γ being the amplitude of the coupling.

Our interest focuses on the system consisting of a biased DNA molecule coupled to ideal contacts in order to estimate the current passing through it. Therefore we search the steady solution of the following master equation:

$$\frac{dP_\mu}{dt} = \frac{dP_\mu}{dt}\Big|_{\text{DNA}} + \frac{dP_\mu}{dt}\Big|_{\text{Leads}} = 0 \ . \tag{7.8}$$

The corresponding system of nonlinear algebraic equations is solved by an iterative method that guarantees the condition $0 \leq P_\mu \leq 1$ [183]:

$$P_\mu^{(j+1)} = \frac{\sum_{\nu=1}^{2N} W_{\nu\mu}\, P_\nu^{(j)} + \Gamma_\mu^L (f_\mu^L - P_\mu^{(j)}) + \Gamma_\mu^R (f_\mu^R - P_\mu^{(j)})}{\sum_{\nu=1}^{2N} W_{\nu\mu}\, P_\nu^{(j)} + \sum_{\nu=1}^{2N} W_{\nu\mu}\, (1 - P_\nu^{(j)}) + \Gamma_\mu^L + \Gamma_\mu^R}, \tag{7.9}$$

where the initial solution to start iterating arises from the charge-current continuity condition applied to every state μ:

$$P_\mu^{(0)} = \frac{\Gamma_\mu^L f_\mu^L + \Gamma_\mu^R f_\mu^R}{\Gamma_\mu^L + \Gamma_\mu^R}. \tag{7.10}$$

The convergence of this iterative method was set to $|P_\mu^{(j+1)} - P_\mu^{(j)}| \leq 10^{-4} \quad \forall \mu$ in our calculations.

Once we get the solution within the specific tolerance, the current along the DNA molecule can be obtained also due to the current conservation condition as follows:

$$I(V) = \sum_{\mu=1}^{2N} \Gamma_\mu^R (f_\mu^R - P_\mu) = -\sum_{\mu=1}^{2N} \Gamma_\mu^L (f_\mu^L - P_\mu). \tag{7.11}$$

7.3. Numerical results: $I - V$ characteristics.

7.3.1. Ordered system

The input tight-binding parameters which define the DNA electronic structure are chosen to fit experimental $I-V$ characteristics of Ref. [118]. In such a experimental situation dry DNA is under consideration and thus, disorder effects are expected to be negligible. According to this experimental setup our calculations are performed over poly(G)-poly(C) DNA molecules of 30 base pairs. The best fitting parameters are $\varepsilon_G = -1.16\,\text{eV}$ and $\varepsilon_C = 1.00\,\text{eV}$, while hopping integrals are $t_{GG} = 0.4\text{eV}$, $t_{CC} = -0.5\,\text{eV}$, $t_\perp = 0.95\,\text{eV}$ and $E_F = -0.13\,\text{eV}$. This value for the Fermi level is in good agreement with the expected one in the middle of the uniform DNA band gap [182]. We assume room temperature and

we consider only interaction with the phonons of the thermal bath. The parameter γ was found to only influence the amplitude of the current and was taken to be $\gamma = W_0$ in all calculations.

Figure 7.2 shows the $I - V$ characteristics for poly(G)-poly(C) DNA at room temperature in the absence of static disorder ($w = 0$). As deduced from Eq. (7.2), a gap of the order of 2.0 eV appears in the $I - V$ characteristics for the chosen set of parameters. In Fig. 7.2 the experimental curve from Ref. [118] is also shown, revealing a good agreement with the predictions of our model.

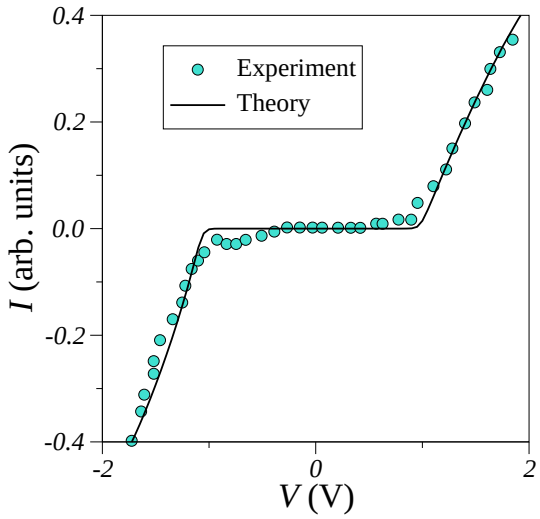

Figure 7.2. *Current-voltage characteristics for a 30 base pair poly(G)-poly(C) DNA at room temperature obtained when $W_0 = \gamma$. Numerical results (solid line) are compared to experimental values (circles) from Ref. [118].*

7.3.2. Disordered system

Uniform disorder distribution

So far we have theoretically supported the experimentally observed semiconducting behavior of dry DNA molecules [118]. Nevertheless, other experiments did no find the existence of a semiconducting gap [117]. In this sense it is well established that disorder gives rise to new eigenstates inside the electronic gap producing its closure [184]. This is also revealed in Fig. 7.3 where the density of states of the system (DOS) is shown for a

single realization of disorder and different magnitudes of it. Thus, it seems reasonable that,

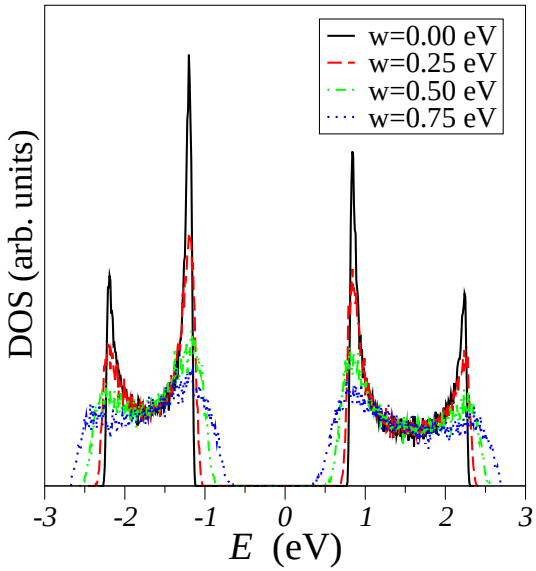

Figure 7.3. *Density of states for a single realization of the disordered DNA-ladder model. The value of the magnitude of the disorder is also indicated.*

by introducing disorder in the site energies of the DNA-ladder model, $I-V$ characteristics presenting smaller voltage gap might arise. For the case of strong enough disorder even a metallic behavior might be found for the system of interest. Therefore, by varying the magnitude of disorder introduced in the system, our model might reproduce a wide range of experimental results. However, our calculations do not agree with these reasonings as shown in Fig. 7.4.

Figure 7.3 shows the DOS while Fig. 7.4 presents the $I-V$ characteristics calculated for the DNA-ladder model considering different magnitudes of disorder of the uniform disorder distribution introduced in Sec. 6.5.1. In the former figure it is clear the appearance of disorder-induced states in the bare band gap which form the tails of DOS by increasing the magnitude of disorder. On the contrary, there is no relevant change in the voltage gap of the characteristics due to the contribution of these new states inside the electronic gap. One of the major differences of these curves by considering a higher magnitude of disorder is a shrinking conductance at high voltages. This effect is reasonable due to the larger localization of the states produced by the strong disorder affecting the system.

On the other hand, the curves in Fig. 7.4 also show a slight increase of the voltage

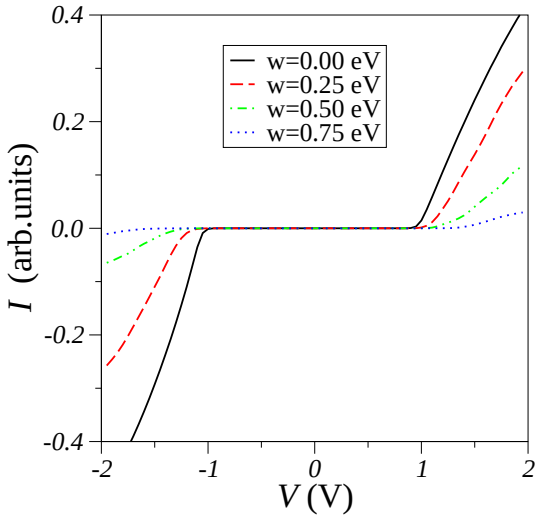

Figure 7.4. *Current-voltage characteristics for a* 30 *base pair poly(G)-poly(C) DNA molecule at room temperature obtained when* $W_0 = \gamma$. *The results were averaged over* 100 *realizations of disorder, whose magnitude is also indicated.*

gap when higher magnitudes of disorder are taken into account. At low voltages, the new disorder-induced states inside the electronic gap are also strongly localized so that the probability of coherent tunneling between them is vanishingly small. Then, transport can only be supported by an incoherent mechanism. In such a case, the most relevant parameter is the averaged level spacing in the tails of DOS which enters directly in the transition rate between these states via the phonon occupation number, see Sec. 4.2.2. According to Refs. [84–87] this magnitude is well established and it can be estimated for the G-band states as [185]:

$$\delta E \approx (432\pi^2)^{-1/3} \, |t_{GG}| \, \left| \frac{2w}{t_{GG}} \right|^{4/3} . \tag{7.12}$$

For instance for $w = 0.5\,\text{eV}$, which was used in our calculations, the level spacing is expected to be approximately 80 meV according to the previous formula. Notice that at room temperature only phonons of 25 meV, much lower than the level spacing of the band-gap states, can be activated. Therefore, they cannot assist incoherent transitions between these states at the tails of the bands. In such a scenario, carrier transfer between both leads can only take place via well-overlapped states appearing above the bare energy band edges [103]. In Ref. [186] it was demonstrated that the energy region where this kind of

states appear, the diffusion mobility edge, is pushed up to the band center when disorder is increased in the system. Thus, for a larger disorder, the appearance of conducting states at higher energies is revealed by the higher voltage gap obtained in the $I-V$ characteristics of Fig. 7.4.

Long-range correlated disorder distribution

Long-range correlations in the energy landscape of DNA sequences have been reported in several references to affect its transport properties [54–56, 128–130]. At this point we want to study if, within the model under consideration in this chapter, a long-range correlated disorder distribution might produce new features in the $I-V$ characteristics of a DNA-ladder model. To this end we will use the disorder distribution already studied in Chaps. 2, 3 and 4 which gives rise to extended states provided that the correlation exponent is larger than a critical one $\alpha_c \approx 2$. In particular, site energies of both DNA strands will be independently generated according to the distribution Eq. (2.2). The mean value of this distribution in one strand will be set to ε_G while in the complementary one will be ε_C.

In order to compare the results provided by the uniform and the correlated disorder models our calculations should be performed for the same standard deviation of the disorder distributions σ. In this respect, notice that we already mentioned in Sec. 6.5.1 that the actual magnitude of disorder of the uniform distribution is proportional to w: $\sigma = w/\sqrt{3}$. Despite having referred w to this concept so far, for the sake of clarity the standard deviation σ is chosen to represent the common magnitude of disorder for both models in this section.

Figure 7.5 compares the $I-V$ characteristics for both models of disorder, the uniform distributed and the one provided by the long-range correlated distribution Eq. (2.2) considering a correlation exponent $\alpha = 5 > \alpha_c \approx 2$. It is shown that the long-range correlations in the disorder model does not produce any change in the voltage gap of the characteristics but only an increase of the conductance at high voltages. This quantitative difference between both models becomes more significative by considering higher magnitudes of disorder.

Notice that the effect of disorder in the case of the uniform distribution is to strongly localize the states of the system. This also affects the states of the long-range correlated system out of the center of the band. However this correlated model supports extended

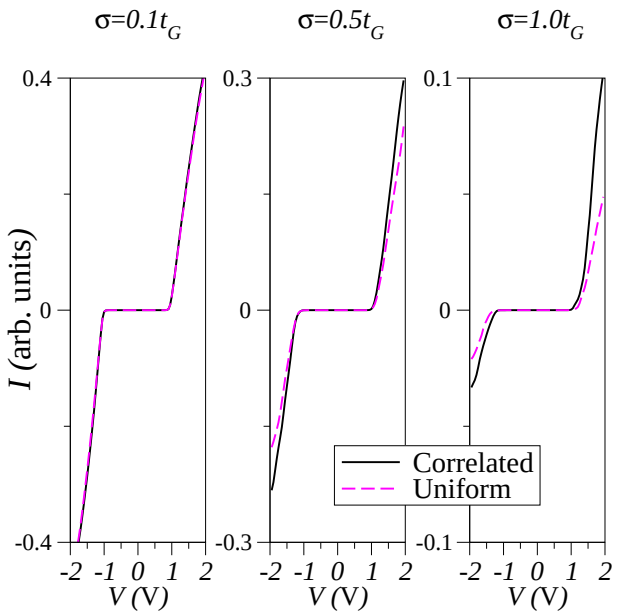

Figure 7.5. *Current-voltage characteristics for a* 30 *base pair poly(G)-poly(C) DNA molecule at room temperature obtained when* $W_0 = \gamma$*. Two disorder distribution are considered: the uniform and the long-range correlated Eq. (2.2) with correlation exponent* $\alpha = 5$*. The results were averaged over* 100 *realizations of disorder, whose magnitude is also indicated.*

states at the center of the poly(G) and poly(C) bands for a correlation exponent $\alpha > \alpha_c$. Thus, the contribution of these extended states to the conductance at high voltages will always be more favorable than the one provided by the localized states of the uniform disorder distribution. However, it is to be mentioned that at low magnitudes of disorder, $\sigma = 0.1t_{GG}$, the localization is still weak to observe differences between both disordered models.

All these considerations are consistent with the discussion previously given in Sec. 7.3.2 to explain the $I-V$ characteristics of Fig. 7.4. The anomalous extended states appear at the center of the poly(G) and poly(C) bands contributing to the conductance only at high voltages. However, the properties of the disorder-induced states inside the electronic gap are similar for both considered models of disorder. Since these are the main responsible for the transport activation at low voltages, no change in the voltage gap is expected to occur by switching on the correlations.

7.4. Conclusions

Electronic transport through a double-stranded DNA molecule attached to two ideal leads was studied. The electronic structure was described by a tight-binding ladder model [133] with random molecular energies. Static disorder localizes the states, and the coupling to the vibrational degrees of freedom of the environment cause transitions between electronic states. A nonlinear master equation for level populations allowed us to obtain the electronic current as a function of the applied voltage.

When the magnitude of disorder is vanishingly small, the $I-V$ characteristics agree with those observed in semiconducting poly(G)-poly(C) DNA [118] for some particular fitting parameters, see Sec. 7.3.1.

The same set of parameters was used to obtain the $I-V$ characteristics at a moderate magnitude of disorder $\sigma = w/\sqrt{3}$ by considering firstly a uniform disorder distribution. As a major result we found that the smearing of the electronic gap by introducing a higher disorder in the DNA base energies is not a sufficient condition to reproduce the shrinking of the voltage gap in $I-V$ characteristics. Contrary to expected, the disorder-induced states inside the electronic gap do not contribute to the incoherent hopping due to their strongly localized character and high energy separation. In such a case, and according to the proposed formalism, only phonon-assisted transport might occur. The efficiency of this mechanism is defined basically by the level spacing and the overlapping of the band tails states which contributes to the electronic transition rates $W_{\mu\nu}$, see Sec. 7.2.2. For the considered DNA-ladder model this spacing results of the order of 80 meV, unaccessible for phonons which are activated at room temperature of energy 25 meV. Therefore, at least within the proposed formalism, the disorder effects cannot reproduce the closure of the voltage gap found in some experiments where DNA is claimed to behave as a metal [114–117].

We also considered a long-range correlated disorder distribution which is reported to support extended states for strong enough correlations [50]. In such a case transport along the system is expected to be enhanced. However, since these favorable conducting states arise deep inside the poly(G) and poly(C) bands, they do not participate in activating the conduction process at low voltages. Therefore, this correlated disorder model can neither reproduce experimental results which establish a narrowing or even a closure of the voltage gap in the $I-V$ characteristics.

Chapter 8

Polaron dynamics in biased DNA molecules

The nucleotide sequence in synthetic homopolymer DNA molecules is periodic. Consequently they can carry electric current when they are subjected to an external bias as studied in the previous chapter. On the other hand, electrons in periodic potentials subjected to an applied electric field present dynamic localization and may undergo coherent oscillations known as Bloch oscillations (BOs) at shorter time-scales than the one related to scattering processes. Our aim now is to investigate whether the carrier, coupled to the deformations of the DNA lattice, might perform sustainable BOs under electric fields within the Peyrard-Bishop-Holstein model (PBH).

8.1. Introduction

In the last chapters the conducting properties of DNA have been studied. In particular we have focused on the case of synthetic DNA-homopolymers as poly(G)-poly(C) where, due to the sequence periodicity, charge transport is expected to occur. We have dedicated a special interest to theoretically support the promising semiconducting properties of such DNA molecules which has been experimentally established [118–122]. Bear in mind that other experiments reveal different conducting behavior for DNA [114–117, 124, 125, 127]. These different observations seem to be caused by environment and contacts effects [159].

In Chap. 7 we took into account the static counterpart of these effects by considering a disordered contribution to the base energies of the DNA molecule. As a further analysis, their fluctuations were described by a nonlinear master equation formalism based on a phonon-assisted hopping mechanism. In this sense, it is well established that structural deformations of DNA are very important in the charge transport process [187]. Indeed, the charge-coupling with such DNA distortions can create a polaron and enhance its mobility. Similarly as what happens in 1D-systems, the polaron behaves as a Brownian particle that collides with environment excitations resulting in a diffusive behavior for the polaronic state. This process reminds the multiple-step hopping mechanism also proposed to explain charge transport in DNA [188,189]. Thus, the behavior of the incoherent charge-hopping can be understood as polaron diffusion. In this regard a variety of works have been dedicated to the description of the polaron dynamics in DNA molecules [190–193].

In this chapter we will take advantage of the accurate description of the nucleotide dynamics and its effects on electric transport provided by the Peyrard-Bishop-Holstein (PBH) model [195–199]. In this model the lattice dynamics is nonlinear, beyond the harmonic approximation, and it allows for a better description of large-amplitude vibrations of nucleotides coupled along each strand. It is worth noticing however that the most remarkable success of the PBH model is focused on the DNA denaturation occurring in the transcription process [195, 196].

On the other hand, due to the periodicity of the nucleotide sequence of some synthetic DNA molecules, the polaron states might behave under electric fields as electrons in periodic potentials subjected to an external bias. As we already mentioned in Chap. 3, in such a case quasiparticles present dynamic localization [65] and may undergo coherent oscillations [63, 64]. They perform a periodic motion, in real and in k space, known

as BOs [66, 67], whose characterizing parameters can be established from semiclassical arguments, see Chap 3. These oscillations are related to the wave dynamics of particles, and therefore they can be observed in almost any coherent motion of waves in tilted periodic potentials [68–77]. The major problem is that BOs persist until the particles lose their phase coherence through scattering processes. In particular DNA molecules largely differs from inorganic solids because vibrations of nucleotides are significant and could rapidly degrade the electron quantum coherence. Nevertheless, Lakhno and Fialko found that homogeneous nucleotide sequences display BOs under electric fields, even if the electron-lattice coupling is taken into account, provided the temperature is low [193]. Their model, however, considers uncoupled nucleotides and small (harmonic) vibrations. More recently this phenomenon was also studied by considering the helical conformation of DNA molecules [194].

In this sense our aim here is to investigate whether the polaron performs sustainable BOs in biased DNA molecules, described by a more realistic model as the PBH model.

8.2. Model

The Hamiltonian of the PBH formalism consists of three contributions:

$$\mathcal{H} = \mathcal{H}_{lat} + \mathcal{H}_{ch} + \mathcal{H}_{int}\,. \tag{8.1}$$

The first term, describing the lattice $\mathcal{H}_{lat}$, arises from the Peyrard-Bishop model which maps the double stranded DNA helix onto a 1D lattice where every node represents a base pair [195]. A single degree of freedom is assigned to every site, y_n, and it represents the stretching of the H-bonds within the two complementary bases. It is worth noticing that, according to this mapping, all inhomogeneities in the sequence, as well as the existing asymmetries in the complementary strands, are beyond the scope of this model. Under these considerations $\mathcal{H}_{lat}$ reads:

$$\mathcal{H}_{lat} = \sum_{n}^{N} \left[\frac{1}{2} m \dot{y}_n^2 + V(y_n) + W(y_n, y_{n-1})\right], \tag{8.2}$$

where m is the nucleotide mass and $n = 1, 2, \ldots N$ labels the base pairs of the DNA molecule.

Apart from the kinetic energy there exist two other potential terms in this Hamiltonian: a local Morse Potential $V(y_n)$ and a nonlinear stacking interaction $W(y_n, y_{n-1})$ whose

particular definitions are the following:

$$V_M(y_n) = V_0 \left(e^{-\alpha y_n} - 1\right)^2 , \tag{8.3a}$$

$$W(y_n, y_{n-1}) = \frac{k}{4}\left(2 + e^{-\beta(y_n + y_{n-1})}\right)(y_n - y_{n-1})^2 \ . \tag{8.3b}$$

The former takes into account the interaction between complementary bases within a base pair, as well as the repulsion between backbone phosphates and other surrounding solvent. The latter represents the nonlinear anharmonic coupling between nearest-neighbor nucleotides which gives rise to long-range interactions. Both potential terms depend on fitting parameters which were chosen to reproduce experimental DNA melting curves. Hereafter we will use the following set of optimized parameters: $m = 300\,\text{amu}$, $V_0 = 0.04\,\text{eV}$, $\alpha = 4.45\,\text{Å}^{-1}$, $k = 0.04\,\text{eV/Å}^2$, $\beta = 0.35\,\text{Å}^{-1}$ and $T = 0.1\,\text{eV}$ [196].

The charge Hamiltonian $\mathcal{H}_{ch}$ is expressed in terms of a tight-binding approach within the nearest-neighbor approximation [197].

$$\mathcal{H}_{ch} = -T\sum_{n}^{N}(a_n^\dagger a_{n+1} + a_{n+1}^\dagger a_n)\,, \tag{8.4}$$

where T describes the nearest-neighbor hopping and $a_n^\dagger(a_n)$ denotes the carrier creation (annihilation) operators. Since there is not a common parameter T in the literature, we will take $T = 0.1\text{eV}$ hereafter as a good representative value [144–146].

The last term in the Hamiltonian, $\mathcal{H}_{int}$, takes into account the charge-lattice interaction and it was proposed by Holstein by introducing an on-site energy correction as follows [197]:

$$\mathcal{H}_{int} = -\chi\sum_{n}^{N} y_n a_n^\dagger a_n\,. \tag{8.5}$$

Here χ denotes the charge-lattice coupling constant. It should be noted that *ab-initio* estimations of this coupling χ are scarce and the results are strongly dependent on the sequence and number of nucleotides [200]. Therefore, we will vary its magnitude in our numerical simulations to study its effects on the carrier dynamics.

The equations of motion for the PBH model can be derived by treating the bases as classical oscillators, while the carrier is described by quantum mechanics. This semiclassical approach is justified by the different time-scales of the charge and the lattice dynamics. For the former, the nearest-neighbor hopping gives rise to time-scales of the order of femtoseconds. On the contrary, the typical phonon frequency of the lattice is in the range of

terahertzs so that the lattice dynamics is three orders of magnitude slower than the one of the carrier [198].

According to this formalism, the dynamics of the carrier in the specific system of interest in this chapter, a biased DNA molecule, can be studied by way of the following Schrödinger equation [199]

$$i\hbar \frac{d\psi_n}{dt} = -Un\psi_n - T(\psi_{n+1} + \psi_{n-1}) + \chi y_n \psi_n \ , \tag{8.6}$$

where ψ_n is the probability amplitude for the charge carrier located a the nth nucleotide. The parameter $U = eFa$ is the potential energy drop across the period of the lattice ($a = 3.4\,\text{Å}$ in DNA) due to the applied bias, which was not considered in the original PBH model. The last term in Eq. (8.6) describes the carrier-vibration coupling through the constant χ and the displacement y_n of the nth nucleotide from its equilibrium position. Newton's equations of motion for the displacement y_n become

$$m \frac{d^2 y_n}{dt^2} = -V_M'(y_n) - W'(y_n, y_{n-1}) - W'(y_n, y_{n+1}) - \chi|\psi_n|^2 \ , \tag{8.7}$$

where the prime indicates differentiation with respect to y_n.

These are the equations we will be using along this chapter to study the dynamics of a charge coupled to the lattice of DNA molecules within the PBH model.

8.3. Stationary polaronic solution

The first step before studying the time evolution of the polaron in the biased lattice is to get the proper stationary polaronic solution of minimum energy of the Hamiltonian Eq. (8.1). To this end, we take advantage of the procedure given in Ref. [197] in an unbiased lattice ($U = 0$), including a dissipative term of the form $-\gamma m dy_n/dt$ in Eq. (8.7) with $\gamma = 50\,\text{THz}$. We solve the nonlinear equations (8.6) and (8.7) using a Runge-Kutta method of 4th order under rigid boundary conditions in a DNA-homopolymer. Gaussian-like packets are used as initial conditions for the lattice distortion as well as for the carrier wave packet. Due to the friction term, the extra energy of this artificial condition will be removed in the energy minimization process. After a long enough time we will get the minimal energy conformation of the charge-lattice system, which is the stationary polaronic solution, to start our dynamical study of the biased DNA molecules.

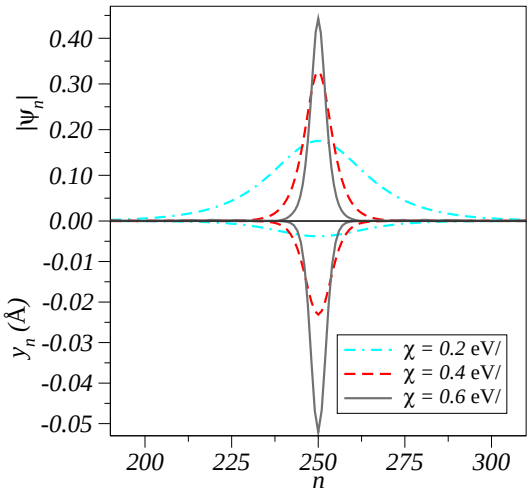

Figure 8.1. *Carrier wave function (upper panel) and lattice displacement (lower panel) at $t = 0$ for different values of χ and $N = 500$.*

In Fig. 8.1, the stationary polarons for different values of χ in a system of $N = 500$ are shown. It is to be noticed that by increasing the strength of the charge-lattice coupling the localization of the stationary states becomes larger.

8.4. Ordered system

8.4.1. Motion of the polaron in a biased system

Once we obtained the stationary polaron of the system under consideration, we use it as the initial condition to let it evolve according to the Eqs. (8.6) and (8.7) in a biased lattice with no dissipation. In this respect, it is worth mentioning that the motion of the polaron in a biased lattice with dissipation is uniform with constant speed [200, 201]. Therefore, dissipation destroys the quantum coherence required for the observation of BOs at very long times.

In order to analyze what happens after the initial excitation of the system, we monitor the time-domain evolution of the carrier wave packet, as well as the one of the lattice distortion.

Figure 8.2(a) displays the wave function while Fig. 8.2(b) shows the corresponding displacements in a lattice of $N = 1000$ sites as a function of position and time, for $\chi =$

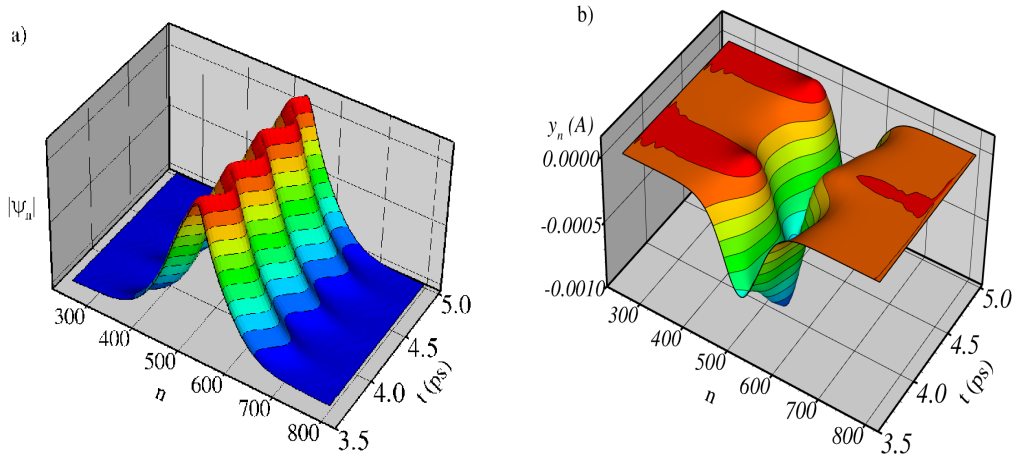

Figure 8.2. *a) Carrier wave function and b) lattice displacement as a function of position and time in a lattice of* $N = 1000$ *sites for* $\chi = 0.1\,\mathrm{eV/Å}$ *and* $F = 3.0\,\mathrm{mV/Å}$, *showing their oscillatory behavior.*

$0.1\,\mathrm{eV/Å}$ and $F = 3.0\,\mathrm{mV/Å}$. Both, the carrier and the lattice, display clear signatures of a coherent oscillation with small distortion of its initial shape.

These oscillations can be monitored in more detail by way of the centroid $c(t)$ of the carrier wave function

$$c(t) = x(t) - x(0)\ , \quad x(t) = \sum_{n=1}^{N} n|\psi_n(t)|^2\ . \tag{8.8a}$$

Similarly for the lattice displacements we define the dimensionless magnitude $l(t)$ as follows

$$l(t) = \xi(t) - \xi(0)\ , \quad \xi(t) = \sum_{n=1}^{N} n\, y_n(t)/a\ . \tag{8.8b}$$

For completeness we also study the Fourier transform of these magnitudes, see Fig. 8.3.

Figure 8.3 displays the calculated $c(t)$ and $l(t)$ in a lattice of $N = 1000$ sites for $\chi = 0.1\,\mathrm{eV/Å}$ and $F = 3.0\,\mathrm{mV/Å}$. The Fourier spectrum of $c(t)$ shows that the centroid of the carrier wave packet performs a harmonic motion with frequency equal to $\omega_B = eFa/\hbar = 15.52\,\mathrm{THz}$, fairly close to the semiclassical value for the Bloch frequency $\omega_B = eFa/\hbar = 15.502\,\mathrm{THz}$ within the numerical uncertainty [see the inset in Fig. 8.3(a)]. However, the lattice displacements display a more complex motion, as seen in Fig. 8.3(b). The main frequency is about $7.22\,\mathrm{THz}$ which is not related to the Bloch frequency ω_B. On the

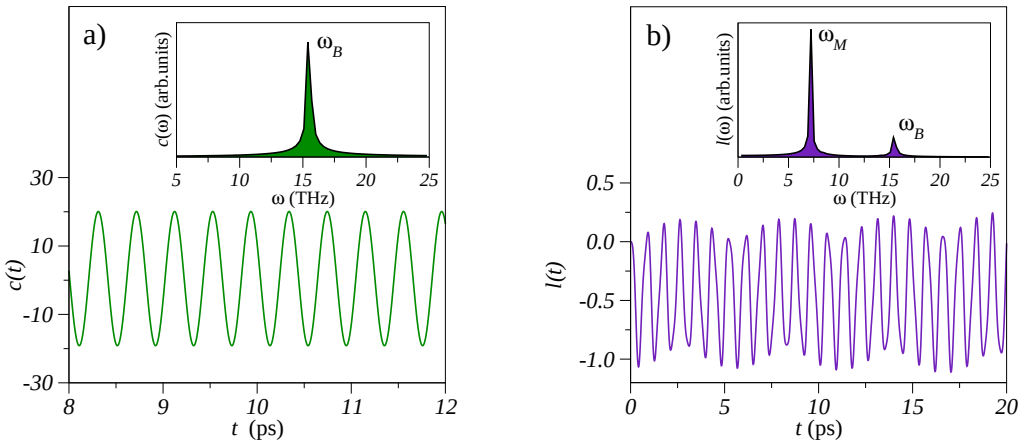

Figure 8.3. *a) Centroid of the carrier wave function and b) $l(t)$ as a function of time in a lattice of $N = 1000$ sites for $\chi = 0.1\,\mathrm{eV/Å}$ and $F = 3.0\,\mathrm{mV/Å}$. The insets show the corresponding Fourier transform.*

contrary, it is close to the Morse frequency ω_M, namely the harmonic frequency of the small amplitude oscillations of a particle with mass m around the minimum of the Morse potential Eq. (8.3a). This frequency is found to be $\omega_M = \alpha\sqrt{2V_0/m} = 7.138\,\mathrm{THz}$ for the set of parameters used in the simulation. Therefore, we come to the conclusion that the oscillations of the lattice and the carrier are almost decoupled, at least at small applied fields. Furthermore, we observe the occurrence of a smaller peak at the Bloch frequency [see the inset in Fig. 8.3(b)]. In spite of the complex behavior of the lattice displacements in the frequency domain, let us stress that the carrier motion is characterized by a single frequency, namely the Bloch frequency.

8.4.2. Average current density

In view of the oscillating behavior of the wave packet of the carrier, it seems reasonable to expect that the current along the DNA molecule behaves in a similar way. Therefore, and since the current is a macroscopic parameter which can be directly observed in experiments, we calculate the current density $J(t)$ through the one-dimensional base stacking. To this end, we firstly consider the local current density at the n-th base pair which is [199]

$$J_n(t) = \frac{i\hbar e}{2m_e a^2}[\psi_n(\psi^*_{n+1} - \psi^*_{n-1}) - \psi^*_n(\psi_{n+1} - \psi_{n-1})]\ , \tag{8.9}$$

where m_e is the mass of the carrier. Then, the average current density over the whole lattice is given by

$$J(t) = \frac{1}{N}\sum_{n=1}^{N} J_n(t) = \frac{\hbar e}{m_e N a^2}\sum_{n=1}^{N} \mathrm{Im}[\psi_n^*(\psi_{n+1} - \psi_{n-1})] \ . \tag{8.10}$$

Our analysis will consider different magnitudes of the applied bias, as well as the charge-lattice coupling. Typical results of our simulations are collected in Fig. 8.4. The left panels show the time-dependent current density over a short time interval when $F = 3.0\,\mathrm{mV/Å}$ and several values of the coupling constant $\chi = 0.1,\ 0.2,\ 0.3\,\mathrm{eV/Å}$. The current density displays a well-defined oscillatory behavior, whose time period matches almost perfectly the semiclassical value $\tau_B = 2\pi\hbar/eFa = 0.405\,\mathrm{ps}$ in the rigid lattice for all shown cases in Fig. 8.4. The right panels display the envelope of the curve $J(t)$ over a much larger time interval, for the same values of the coupling constant. The increase of the coupling constant leads to a faster modulation of the current density but, remarkably, the oscillations do not decay on time. As we already did in the case of the centroid, the Fourier

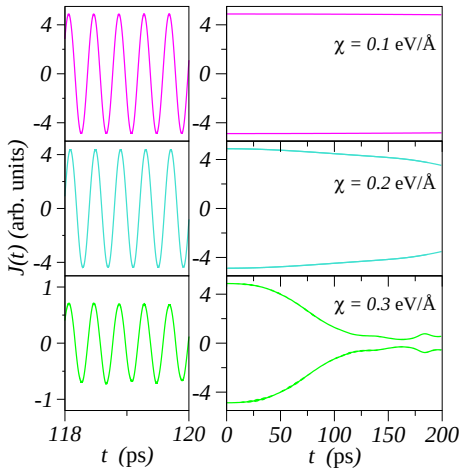

Figure 8.4. *Current density as a function of time when* $F = 3.0\,\mathrm{mV/Å}$ *for different values of the coupling constant, namely* $\chi = 0.1, 0.2, 0.3\,\mathrm{eV/Å}$ *from top to bottom. The left panels show the oscillatory behavior over a short time interval. The right panels only show the envelope of the current over a much longer time interval.*

transform of the average current density is calculated in order to clarify which frequencies

are playing a major role in the polaron dynamics for several values of the coupling constant χ and electric field F, see Fig. 8.5.

For all considered coupling constants the Fourier spectrum transforms in a single peak at the semiclassical value of the Bloch frequency $\omega_B = eFa/\hbar$ ($\omega_B = 1.55\,\mathrm{THz}$ and $\omega_B = 15.50\,\mathrm{THz}$ for $F = 0.3\,\mathrm{mV/Å}$ and $F = 3.0\,\mathrm{mV/Å}$, respectively) as expected.

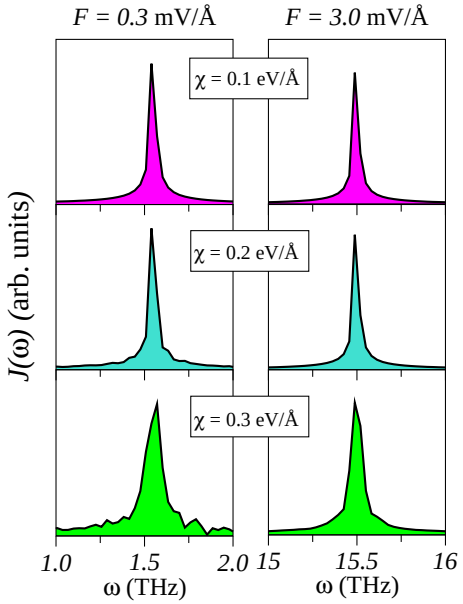

Figure 8.5. *Fourier transform of the current density $J(t)$ for $F = 0.3\,\mathrm{mV/Å}$ (left panels) and $F = 3.0\,\mathrm{mV/Å}$ (right panels) and three different values of the coupling constant, namely $\chi = 0.1$, 0.2, $0.3\,\mathrm{eV/Å}$ from top to bottom.*

However, it is worth mentioning that for higher electric fields, the modulation of the current density becomes even faster on increasing the coupling constant χ. This gives rise to side peaks around ω_B in the Fourier spectrum but even in the case of a broad Fourier spectrum, quasi-harmonics oscillations are observed over time intervals larger than τ_B [202].

8.5. Disordered system

As it was already discussed along this Thesis, it seems that long-range correlations in DNA sequences may play an important role on its properties [54–56, 128–130]. An

example of a long-range correlated disorder distribution and its effects on optical and transport properties of 1D systems was deeply studied in Chaps. 2, 3, and 4. The main issue which attracts our attention in this chapter is that systems, whose energy sites are generated according to the disorder distribution Eq. (2.2), might support BOs in the case of strong correlations, see [78]. However, in this study no particle-lattice interaction was considered. Our interest now is to study if BOs might arise in DNA molecules with a long-range correlated energy landscape within the PBH model.

In order to analyze the effect of this specific model of disorder on our study, a new diagonal term is included in Eq. (8.6) in the following way:

$$i\hbar \frac{d\psi_n}{dt} = \mathcal{E}_n\psi_n - Un\psi_n - T(\psi_{n+1} + \psi_{n-1}) + \chi y_n\psi_n \ , \tag{8.11}$$

where the sequence of site energies $\mathcal{E}_n = \bar{\mathcal{E}} + \varepsilon_n$ is generated according to Eq. (2.2) and setting $\bar{\mathcal{E}} = 0$ without loss of generality.

8.5.1. Motion of the polaron in biased disordered systems

Similarly as in Sec. 8.4.1, we calculate the time-evolution of the stationary polaronic solution obtained in Sec. 8.3. To this end, we integrate Eq. (8.7) and Eq. (8.11) including disorder in the site energies of a biased lattice without dissipation. The numerical integration method, as well as the boundary conditions used in this case are the same that those previously considered in this chapter. Our interest is to monitor the motion of the polaron in a biased disordered DNA molecule in two limiting cases: the strongly correlated (i.e. $\alpha = 5$) and the weakly correlated disorder (i.e. $\alpha = 1$), see previous chapters. To this end, the modulus of the carrier wave function $|\psi_n|$ and the local lattice distortion y_n are displayed by means of density plots.

Figures 8.6 and 8.7 show the amplitudes associated to the carrier wave function (right panels) and the corresponding local lattice displacement (left panels) in a lattice of $N = 750$ sites as a function of position and time for a single realization of disorder. The parameters considered are $\chi = 0.3\,\mathrm{eV/Å}$, $F = 3.0\,\mathrm{mV/Å}$, and magnitude of disorder $\sigma = 0.1\,\mathrm{eV}$. Notice that this magnitude of disorder is of the order of the nearest-neighbor hopping T. The correlation exponent is $\alpha = 1$ in Fig. 8.6 (weak correlations) while $\alpha = 5$ in Fig. 8.7 (strong correlations).

No signatures of BOs are revealed in the carrier wave packet motion in Fig. 8.6(b), as a clear indication of disorder-induced dephasing effects, expected in the weakly correlated

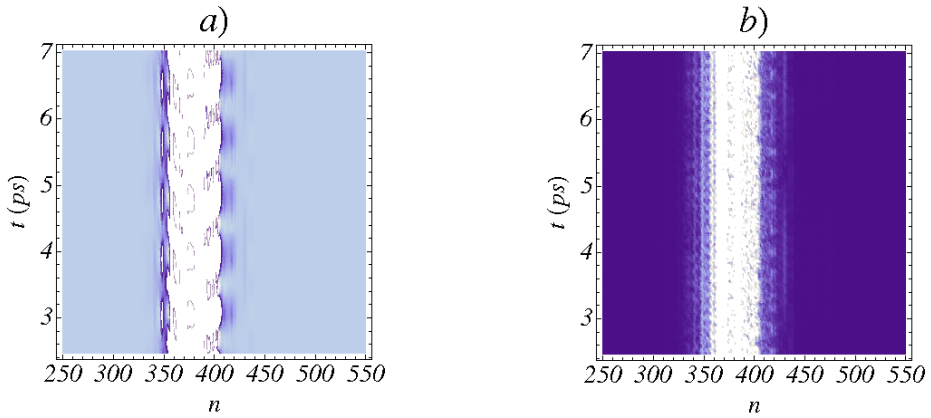

Figure 8.6. *a) Local lattice displacement and b) modulus of the carrier wave function in a lattice of* $N = 750$ *sites as a function of position and time for a single realization of disorder. The parameters considered are* $\chi = 0.3\,\mathrm{eV/Å}$, $F = 3.0\,\mathrm{mV/Å}$, *magnitude of disorder* $\sigma = 0.1\,\mathrm{eV}$ *and correlation exponent* $\alpha = 1$. *Light and dark regions indicate nonzero and zero values, respectively.*

regime. However, the lattice dynamics seems to present weak traces of a periodic time-evolution, as seen in Fig. 8.6(a). On the contrary, at $\alpha = 5$ in Fig. 8.7, the density plots show well behaving oscillations for the carrier and the lattice dynamics, demonstrating that strong correlations enhance the coherence neccesary for BOs to arise.

As in Sec. 8.4.1 we calculate the Fourier spectrum of the time-dependent magnitudes $c(t)$ and $l(t)$ [defined in Eqs. (8.8a) and (8.8b)] to make clear which frequencies are exactly involved in the carrier and the lattice time-evolution, see Fig. 8.8. The lower panel of Fig. 8.8(a) confirms that in the case of weakly correlated systems, no well defined oscillations are performed by the wave packet of the carrier and therefore, a variety of several peaks arise in the Fourier spectrum of its centroid, $c(t)$. On the contrary, in the upper panel the analogous magnitude for the lattice distortion, $l(t)$, reveals a clear oscillatory behavior, as we already presumed in the preceding paragraph. Similarly to what happens in the case of the ordered lattice (see Sec. 8.4.1), $l(t)$ oscillates with a main frequency of 7.22 THz close to the Morse frequency of the system $\omega_M = 7.138\,\mathrm{THz}$ according to its Fourier spectrum. Nevertheless, in the disordered situation there is no other peak related to the Bloch frequency contribution which indeed appears in the ordered lattice. Therefore, our claim is that the dynamics of the disordered lattice is basically determined by

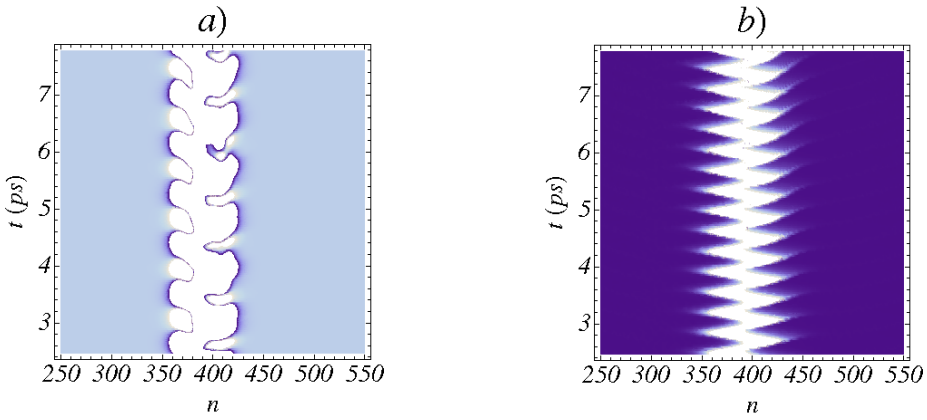

Figure 8.7. *Same as in Fig. 8.6 but considering the correlation exponent* $\alpha = 5$.

the Morse potential and it is even more decoupled of the carrier one than in the ordered case.

On the other hand, Fig. 8.8(b) confirms the results observed in Fig. 8.7 for the strongly correlated regime. Thus, well behaving BOs appear in the time-evolution of the magnitudes $c(t)$ and $l(t)$. The Fourier spectrum for $l(t)$ turns out to be single-peaked again at the Morse frequency as in the weakly correlated regime, while that associated to $c(t)$ reveals now a well defined peak at 17.0 THz. Notice that, contrary to what happens in the uniform lattice, this frequency does not coincide with the expected semiclassical value of the Bloch frequency $\omega_B = 15.502\,\mathrm{THz}$ but it is blue-shifted respect to this value.

This deviation can be understood looking at the particular energy landscape of the considered realization of disorder and taking advantage of the simplification proposed in Sec. 2.4 for strongly correlated systems (see Fig. 8.9). According to that approach, in the case of strong correlations the whole distribution Eq. (2.2) can be substituted by the first term of the sum:

$$\varepsilon_n \approx \sigma C_\alpha \cos\left(\frac{2\pi n}{N} + \phi_1\right) . \tag{8.12}$$

In such a case, this is the dominant term in Eq. (2.2) which is determined by the random phase ϕ_1. The phase randomly generated in our simulation was $\phi_1 = 5.28\,\mathrm{rad}$. Figure 8.9 shows the actual energy landscape of the single realization used in our calculations as well as the simplified one Eq. (8.12). Notice that such an energy landscape gives rise to a new tilted potential at the center of the lattice which is to be added to the linear applied bias.

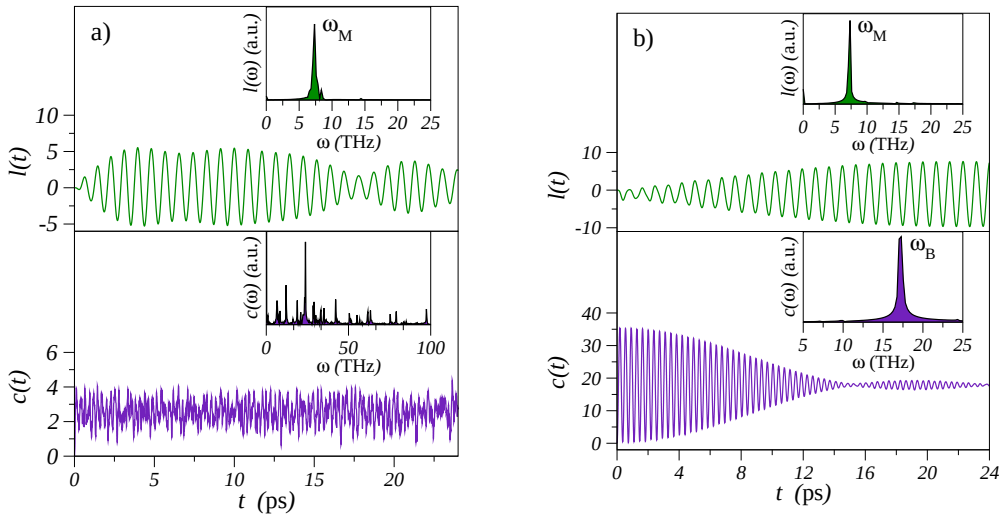

Figure 8.8. *Centroid of the carrier wave function, $c(t)$, and $l(t)$ as a function of time in a disordered lattice of $N = 750$ sites for $\chi = 0.3\,\mathrm{eV/Å}$, and $F = 3.0\,\mathrm{mV/Å}$. The magnitude of disorder is set to $\sigma = 0.1\mathrm{eV}$ and the correlation exponents are a) $\alpha = 1$ and b) $\alpha = 5$. The insets show the corresponding Fourier transforms.*

According to the Taylor expansion of Eq. (8.12):

$$\varepsilon_n = \varepsilon_{N/2} + (n - N/2)\left.\frac{d\varepsilon_n}{dn}\right|_{N/2} + O(n^2), \tag{8.13}$$

the effective potential drop across one lattice period due to disorder effects at the initial position of the polaron is $U_{\mathrm{eff}} = \xi_\alpha \sin\phi_1$, with $\xi_\alpha = 2\pi\sigma C_\alpha/Na$. In the case of our random realization ($\phi_1 = 5.28\,\mathrm{rad}$) it results in an effective bias of $U_{\mathrm{eff}} \approx -1.0\,\mathrm{meV/Å}$. The term $U_{\mathrm{eff}}\, n$ is to be included in Eq. (8.6) in such a way that the potential energy drop across one period of the lattice becomes now $-(U - U_{\mathrm{eff}})$. Thus, the semiclassical Bloch frequency under such conditions is $\omega_B^* = (U - U_{\mathrm{eff}})/\hbar \approx 17.0\,\mathrm{THz}$, which is in prefect agreement with the position of the single peak revealed by the Fourier spectrum of the centroid $c(t)$, see Fig. 8.8(b). It is worth mentioning that the energy landscape of the particular considered realization of disorder (see Fig. 8.9) can be well approximated by a linear profile at the center of the molecule, which leads to the definition of the effective bias U_{eff}. In those realizations of disorder where this is not the case, the previously introduced effective potential U_{eff} is actually not well defined. Thus, despite finding well behaving oscillations of the wave function, the Fourier spectrum of $c(t)$ becomes more complex,

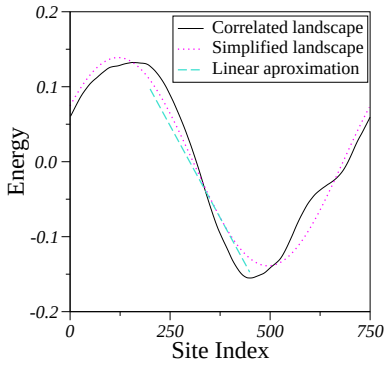

Figure 8.9. *Energy landscape of a single realization of the disorder distribution Eq. (2.2) for a correlation exponent $\alpha = 5$ and a system of $N = 750$ sites. The simplified energy landscape defined by the first term of the distribution is also displayed.*

presenting several peaks around the semiclassical value of the Bloch frequency.

For completeness we also study the dynamics of the wave packet for different values of the carrier-lattice coupling and the applied bias in the strongly correlated situation. Bear in mind that the lattice dynamics is defined in all cases by the Morse potential, not depending on the remaining model parameters as we already demonstrated. Our calculations, summarized in Fig. (8.10), show that for all considered parameters the carrier wave packet performs well behaving oscillations, whose amplitude and period depend on the bias strength as expected for BOs, namely $L_B \propto 1/F$ and $\tau_B \propto 1/F$ [63, 64], see Figs. 8.7 and 8.10. On the other hand, these oscillations behave similarly for different values of the carrier-lattice coupling. In this respect notice that for a small coupling (i. e. $\chi = 0.1\,\mathrm{eV/Å}$) the polaron extends over a larger number of nucleotides and therefore, it is more easily affected by disorder effects, leading to a faster transformation of the initial shape of the wave packet, see Figs. 8.10(b) and 8.10(c).

Figure 8.10 shows the above mentioned density plots associated to the carrier wave packet dynamics for different values of the applied bias and charge-lattice coupling. We stress that, since the amplitude of the BOs increases by decreasing the applied bias, the system size should be larger to support the oscillating carrier dynamics at low fields.

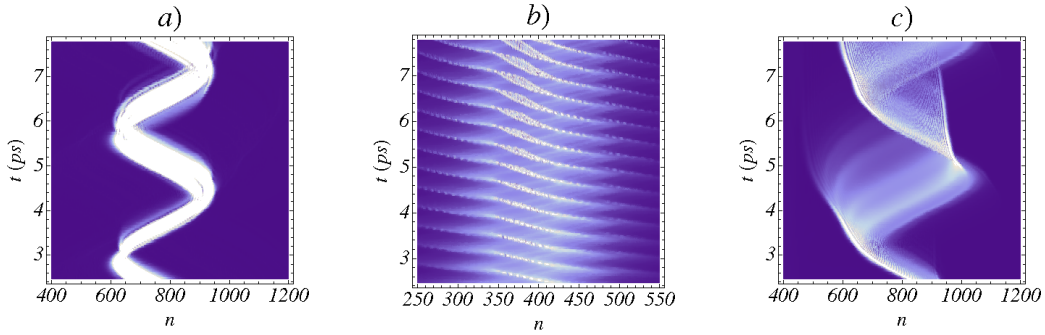

Figure 8.10. *Modulus of the carrier wave packet as a function of position and time for a single realization of disorder ($\sigma = 0.1\,eV$ and $\alpha = 5$). The considered parameters for the biased lattice are the following: a) $N = 750$ sites, $\chi = 0.3\,\mathrm{eV/Å}$ and $F = 0.3\,\mathrm{mV/Å}$, b) $N = 1250$ sites, $\chi = 0.1\,\mathrm{eV/Å}$ and $F = 3.0\,\mathrm{mV/Å}$, and c) $N = 1250$ sites, $\chi = 0.1\,\mathrm{eV/Å}$ and $F = 0.3\,\mathrm{mV/Å}$.*

8.5.2. Average current density

In view of the oscillatory motion performed by the wave packet of the carrier in the strongly correlated regime, a similar time-dependent dynamics can be demonstrated for the average current density defined in Eq. (8.10). Indeed, according to the results of Sec. 8.5.1, the oscillation frequency of $J(t)$ is expected to be slightly shifted respect to the predicted Bloch frequency in disordered lattices. Moreover, this shift was proved to depend on the particular realization of disorder in the previous section. Therefore, by considering the Fourier transform $J(\omega)$ of an ensemble of disordered sequences, one can obtain the frequency probability distribution of $J(t)$ centered at the semiclassical Bloch frequency. The width of this distribution, σ_ω, might be estimated within the same argument that in the preceding section: the effective disorder-induced bias U_{eff} is proportional to the frequency shift of the Fourier peak of $J(\omega)$ with respect to the semiclassical value ω_B. Thus, its probability distribution coincides with the one of the shifted frequencies of $J(t)$ for different realizations of disordered sequences.

This probability distribution can be analytically calculated keeping in mind that the randomness of Eq. (2.2) arises from the set of $N/2$ independent random phases $\phi_1, \ldots, \phi_{N/2}$ uniformly distributed within the interval $[0, 2\pi]$. Therefore, one can write $\mathcal{P}(U_{\text{eff}})dU_{\text{eff}} =$

$\mathcal{P}(\phi)d\phi$ and the following distribution for the effective bias can be obtained

$$\mathcal{P}(U_{\text{eff}}) = \frac{1}{\pi\sqrt{\xi_\alpha^2 - U_{\text{eff}}^2}}\,. \tag{8.14}$$

This probability distribution diverges at the edges and its width is given by $\sigma_\omega = 2\xi_\alpha = 4\pi\sigma C_\alpha/Na$. Thus, σ_ω is inversely proportional to the number of base pairs N.

Our numerical calculations prove the validity of the above approach. To this end, we calculate $J(t)$ and the average Fourier spectrum $\langle J(\omega)\rangle$ for an ensemble of disorder realizations. We repeat this procedure for four different sizes of the system $N = 750$, $N = 1000$, $N = 1250$, and $N = 1500$ and display simultaneously our results in Fig. 8.11. This figure clearly demonstrates that the width of $\langle J(\omega)\rangle$ decreases upon increasing the number of nucleotides. This means that disorder effects are less relevant in longer chains and therefore, the average current density oscillates with a frequency closer to the Bloch frequency.

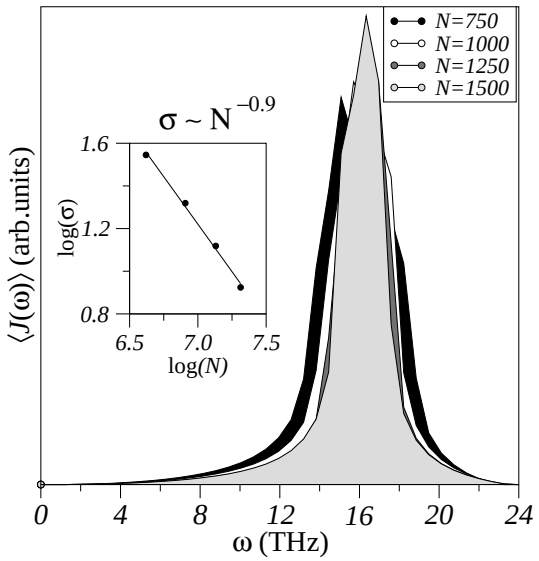

Figure 8.11. *Average Fourier transform of the current density $J(t)$ of* 100 *different realizations of disorder. The parameters used in the calculations are:* $\chi = 0.1\,\text{eV/Å}$ *and* $F = 3.0\,\text{mV/Å}$, $\sigma = 0.1$ *eV and* $\alpha = 5$. *Four different sizes of the system are considered. The inset displays* $\log(\sigma_\omega)$ *vs.* $\log(N)$ *as well as the fitting of these data.*

On the other hand, our calculations are in good agreement with the above proposed

approach to describe the dispersion of the oscillation frequencies of $J(t)$ in disordered systems. Indeed, we find a size-dependence $\sigma_\omega \propto 1/N^{0.90}$, close to that predicted by our simplified model $\sigma_\omega \propto 1/N$. Needless to say, the divergences in this respect come from the approximations considered in our approach: i.e. the simplification of the energy landscape by a harmonic-like shape, and the absence of the charge-lattice coupling in our arguments or the definition of U_{eff} as the derivative of the energy landscape at a single site of the system.

8.6. Conclusions

The polaron dynamics was studied in synthetic biased DNA molecules within the Peyrard-Bishop-Holstein model, which accurately describes the charge dynamics in DNA [195–199]. It is well known that, neglecting the charge-lattice interaction, the electron undergoes coherent and harmonic oscillations in biased uniform lattices, known as Bloch oscillations [63,64]. In this chapter it was firstly demonstrated that these oscillations might even occur when dealing with polaron states within the PBH model in DNA-homopolymers. In particular, we found that the lattice dynamics is mainly defined by the Morse potential included in the model, while the carrier wave packet oscillates with a well defined frequency coinciding with the semiclassical value for the Bloch frequency.

As a further study, we also considered the effects of a nonuniform nucleotide sequence, as well as the environment conditions of DNA, which locally modify the base energy levels, on the polaron dynamics. In this regard, it is well established the existence of long-range correlations in the energy landscape of natural DNA sequences [54–56,128–130]. Therefore, we used the energy distribution used in Ref. [50], which models long-range correlations, to generate the base-energy sequence of DNA molecules.

Such correlated distribution allows for BOs despite disorder-induced dephasing effects when correlations are strong enough and the charge-lattice coupling is neglected [78]. In this chapter we proved that this also occurs when considering polaron states within the PBH model. Thus, even when charge and lattice are coupled, we still found an oscillatory carrier dynamics for the strongly correlated regime. However, its frequency turned out to be shifted with respect to the semiclassical value of the Bloch frequency. We theoretically explained this shift by extending a simplified approach formerly proposed in Chap. 2.

In DNA-homopolymers, as well as in DNA sequences whose energy landscape presents

long-range correlations, the oscillatory carrier dynamics leads to alternating currents across the DNA molecule whose frequency lies in the THz range, which might be useful in nanoelectronic applications. In the nonuniform case, we also calculated the averaged Fourier transform of the electric current in an ensemble of disordered DNA sequences. The frequency dispersion around the Bloch frequency decreases by considering larger systems, where disorder effects seem to be less relevant in this regard. We were able to explain this claim by means of the previously mentioned simplified analytical approach.

It is to be noticed that, apart from the disorder-induced effects, scattering by phonons also destroys the phase coherence at times larger than the scattering time τ and therefore, BOs can hardly be observed at such time-scales. Lakhno and Fialko [193] estimated that the temperature $T_{\max}$ below which BOs take place at a given magnitude of the electric field is $T_{\max} \simeq 0.45 T_0 (\omega_B \tau_0)^{1/2.3}$, where $\tau_0 \sim 6.4 \cdot 10^{-15}\,\mathrm{s}$ is the relaxation time at $T_0 = 300\,\mathrm{K}$. This means that for instance at a field magnitude of $F = 3.0\,\mathrm{mV/Å}$, BOs might be observed at $T < T_{\max} = 50\,\mathrm{K}$. Larger electric fields are applied in the charge transport experiments on DNA what raise this threshold temperature.

Chapter 9

Conclusions and perspectives

9.1. Anomalous properties of a 1D model with long-range correlated disorder

In **Chaps. 2, 3,** and **4** we have studied transport and optical properties of the 1D model of disorder proposed in Ref. [50] by means of a Frenkel Hamiltonian. This model supports long-range correlations whose strength depends on the correlation exponent α such that, for $\alpha > \alpha_c$, anomalous properties arise in the system. Recent research already established a LDT for this model which takes place for a correlation exponent larger than a critical one $\alpha > \alpha_c \approx 2$ [50–52]. In this Thesis new evidences of this LDT transition have been revealed. Firstly, we calculated the IPR and the transmission properties of the states, and by averaging over an ensemble of disorder realizations, we obtained a phase diagram related to the localization properties of the system. Thus, we demonstrated the existence of a phase of extended states at the center of the energy spectrum for $\alpha > 2$ which besides, presents perfect transmission. Our results should be taken into account for completeness and they are consistent with those of previous works obtained for a single realization of disorder [50, 51]. Looking at the linear optical absorption spectra of this kind of systems, we found that the single absorption line typical for the Frenkel model with uncorrelated disorder transforms into a double-peaked lineshape for $\alpha > \alpha_c$ as a new anomaly of the

model. We proposed a simplification of the original distribution of disorder in the case of strong enough correlations which explains perfectly our numerical results [203].

Due to the existence of the mentioned extended phase when $\alpha > \alpha_c$, it was claimed in Ref. [78] that the quasiparticle might perform coherent BOs within this model of disorder. In this regard, **Chap. 3** was dedicated to the study of such oscillations in the frequency domain looking for signatures of the Wannier-Stark quantization. We demonstrated that due to the interplay of disorder and bias effects, strong correlations or strong bias enhance the appearance of this periodic pattern in the optical absorption spectra. In particular, for strong enough bias we found a periodic double-peak structure reminding the absorption properties of the unbiased system [204].

In view of the linear optical absorption of these biased lattices, the intraband relaxation of excitonic states was considered in **Chap. 4**. We used a Pauli master equation formalism to study the fluorescence decay after broadband pulse excitation. We claim that there is a full correspondence between the appearance of the WSL in the absorption spectra and the exponential time-dependent decay of the fluorescence. We evaluated the relevance of finite-size effects in our study and we demonstrated that our main conclusions are not a consequence of such effects [205].

9.2. Optical and transport properties of DNA

Our study starts considering the importance of the base pairing correlations in random DNA molecules in **Chap. 5**. The Landauer and the Lyapunov exponents calculated for a DNA-ladder model reveal that the correlations appearing in DNA due to the base complementarity do not allow for the existence of extended states or states localized in regions larger than the system size, in contrast to what was claimed in Ref. [131]. Therefore, these correlations cannot explain DNA transport at zero temperature. We used the same exponents, as well as the time-evolution of the participation number of a localized wave packet, to demonstrate that, by varying the tight-binding hopping parameters within the range considered in the literature, no extended state can arise in the system either [206].

In the case of DNA-homopolymers such as poly(G)-poly(C) DNA, the situation is completely different. Due to the periodicity of these nucleotide sequences, it is to be noticed that two well separated bands of extended states might arise in these systems [148]. Some experimental current-voltage curves, revealing a semiconducting behavior for these

molecules [118], also confirm this theoretical prediction. There exist however other contradictory results in this respect, justified by different environment and contact effects. In **Chap. 6** we proposed to characterize the predicted semiconducting behavior for poly(G)-poly(C) by studying the interband optical transitions between the HOMO and the LUMO bands. Our study shows the importance of a proper definition of the value and the sign of the hopping parameters and how they can be estimated by way of experimental measurements of such transitions in the visible region [207, 208]. Unfortunately we experimentally showed that these transitions are very weak and it is important to design proper DNA samples or to use sofisticated experimental technics to detect them. The environment effects due to the surrounding solution around the DNA molecules must also be taken into account in this experiment. We theoretically modeled these effects by introducing static diagonal disorder in the site energies of the DNA-bases and we demonstrated that disorder-induced states appear inside the electronic gap. In such a case, the stronger the magnitude of disorder affecting the DNA samples is, the more difficult the detection of the predicted interband absorption spectra in the visible region becomes. This means that experiments over dry DNA are preferable.

In **Chap. 7** we proposed a Pauli master equation formalism to take into account these environment effects in a dynamical way by introducing thermal-activated hoppings. In the case of the ordered lattice our results are in perfect agreement with the experimental evidences of the semiconducting DNA behavior for some fitting parameters. When static disorder is included in the model, all states become localized according to the scaling theory [33]. Then, incoherent hopping processes were expected to be thermally activated and enhance the conductivity through disorder-induced states inside the semiconducting gap. In such a way, we tried to explain experimental results claiming that DNA can behave as a poor metal as well. However, according to our model, the typical energy of phonons at room temperature is much lower that the one needed by the carrier to hop between the midgap states. This is also the case when we include long-range correlations in the disorder distribution of the system. Therefore, according to our formalism, no incoherent transport at low voltages can be activated at room temperature when environment effects are relevant and thus, our model cannot explain simultaneously the semiconducting and the metallic DNA conductivity observed in experiments [209].

In **Chap. 8** the coupling between the carrier and the lattice dynamics is considered in DNA molecules in a different fashion, namely within the PBH formalism [196]. Thus, we

studied the polaron dynamics in biased uniform DNA molecules and we demonstrated that in absence of dissipative effects, BOs might arise in this model, giving rise to oscillating currents in the range of terahertzs [202]. We demonstrated that these results remain valid even for nonuniform DNA molecules provided that strong enough long-range correlations are present [210].

9.3. Perspectives

Regarding Chaps. 2, 3, and 4 it seems clear that the characterization of the 1D model of disorder proposed in Ref. [50], as well as its understanding by means of the simplification proposed in this Thesis is already satisfactory. As a further step on this topic the observation of our theoretical predictions in a experimental set up is in order. The Frenkel model we have been dealing with is established as a good description for J-aggregates properties [26]. However, it would be difficult to introduce a disorder affecting the aggregate molecules in such a specific way as that proposed by the distribution Eq.(2.2). Nevertheless, our results are also valid for other kind of systems described by similar tight-binding Hamiltonians. For instance ultracold atoms in optical lattices created by laser waves, which are more easily tunable, would be a promising scenario to experimentally test our predictions. On the other hand, despite the existence of long-range correlations in DNA sequences has been already experimentally demonstrated, the direct applicability of the model of Ref. [50] in this field is still missing. While the disorder distribution Eq.(2.2) is continuous, the DNA molecules are consistent of only four bases. Therefore, it is necessary to develop a variation of the considered model which is consistent with the discrete nature of DNA sequences. In this regard, there was already a dicotomic theoretical proposal based on the existence of two possible base pairs in DNA: GC or AT. This model, in spite of including long-range correlations on the sequences, failed to reproduce a localization-delocalization transition which could explain long-range transport in DNA [54].

On the other hand, regarding the conducting properties of DNA it is crucial to improve the experimental technics to avoid or, at least, to properly control environment or contact effects, as well as the quality of the samples to get a common description of the conducting DNA properties. Our claim is that DNA-homopolymers, as well as DNA sequences with long-range correlations, are good candidates to support long-range transport as long as environment effects are diminished, namely in case of dry DNA. We really think

that our proposal to study the optical absorption of DNA sequences in the visible region to elucidate the semiconducting behavior of DNA molecules is very promising due to the absence of contacts effects in this experiment. Therefore, it would be worth designing optimized periodic DNA samples and studying its structural properties in high concentrated solutions to intensify such optical transitions. On the other hand, it turns to be crucial a proper description of environment effects in this kind of biological systems since they are surrounded by many different solvent molecules with dynamics at different time-scales. In the same way, due to the softness of DNA molecules, the electron-phonon coupling must be considered and polaron models must be taken into account. In this regard, though the PBH model has been demonstrated as a powerful tool to describe melting processes of DNA [196], the polaron states which it describes are localized in regions too large compared to the DNA molecules commonly used in conducting experiments. In this sense small polaron models open another possibility to describe transport mediated by polarons in DNA [211].

List of acronyms

- **BO** Bloch oscillation.
- **DBL** Dangling backbone ladder.
- **DNA** Deoxyribonucleic acid.
- **DOS** Density of states.
- **HOMO** Highest occupied molecular orbital.
- **IDT** Integrated DNA technologies.
- **IPR** Inverse participation ratio.
- **LDT** Localization-delocalization transition.
- **LUMO** Lowest unoccupied molecular orbital.
- **OAS** Optical absorption spectrum.
- **PAGE** Polyacrylamide gel electrophoresis.
- **PBH** Peyrard-Bishop-Holstein.
- **PR** Participation ratio.
- **RNA** Ribonucleic acid.
- **SL** Simple ladder.
- **WSL** Wannier-Stark ladder.

Breve resumen de la Tesis

Introducción

¿Por qué sistemas moleculares? El estudio de los sistemas moleculares complejos es un campo altamente interdisciplinar donde la colaboración entre físicos, químicos y biólogos es crucial [1, 2]. La variedad de moléculas que se encuentran en la naturaleza ya es enorme si pensamos en las proteínas, ADNs o ARNs. Pero igualmente, sería difícil imaginarse nuestro día a día sin un gran número de macromoléculas sintéticas como por ejemplo el polietileno, el poliestireno o el Teflon [3]. En líneas generales, estos sistemas moleculares complejos están formados por un gran número de unidades moleculares idénticas o distintas que se unen por interacciones no covalentes, especialmente de tipo Van der Waals [4]. Estas fuerzas intermoleculares son de hecho la base de muchos procesos de regulación o de reconocimiento selectivo entre moléculas, así como de transporte en sistemas biológicos [5].

Inicialmente, las contribuciones de la física en este campo se centraron en la caracterización estructural de los sistemas moleculares por rayos X, difracción de neutrones o técnicas de resonancia magnética [6]. Sin embargo, el estudio de las propiedades físicas de estos sistemas, desde un punto de vista teórico o experimental, es también imprescindible para describir los principios que rigen la organización y conformación de estos sistemas moleculares.

Uno de los intereses principales de los físicos en este campo es debido a la obtención de sistemas orgánicos que presenten una alta conductividad eléctrica. Estos materiales han adquirido una gran importancia en los últimos años debido a su aplicación en electrónica molecular [7]. Por ejemplo, desde el descubrimiento del poliacetileno dopado $(CH)_n$ (ver Fig. 1.1) que presenta una alta conductividad [8], se han dedicado muchos esfuerzos ha caracterizar el comportamiento conductor de los polímeros.

Por otra parte el interés de los químicos por estos sistemas se centra en el reconocimiento selectivo que tiene lugar entre moléculas unidas por enlaces no covalentes, de manera que su estructura queda definida por su afinidad electrónica o geométrica [10]. De hecho, de acuerdo con los criterios de selección molecular, se pueden diseñar sistemas con una cierta forma, estructura o tamaño para que contribuyan de una manera específica en reacciones o procesos de transporte [11].

Algunos sistemas moleculares también son interesantes porque convierten la radiación óptica en energía química útil en ciertas reacciones. Normalmente en estos casos, la absorción de luz se da en un componente llamado donor y es transferida por interacciones moleculares hasta el centro de la reacción [12]. Dicha transferencia de energía puede darse a lo largo de grandes distancias y es un proceso de gran relevancia en sistemas moleculares que incluso, puede ser utilizado para redireccionar la energía a centros funcionales específicos [11]. Esto es lo que ocurre por ejemplo en lo que se conoce como complejos antena donde se capta la luz necesaria para la fotosíntesis u otros utilizados en fotografía [13]. Los ejemplos típicos de estos complejos en sistemas biológicos son la clorofila [12] y los carotenoides (ver Fig. 1.2) [13]. Vale la pena mencionar también que hay una gran variedad de agregados-J que realizan este tipo de funciones [14–17].

Siguiendo con el análisis de sistemas complejos, las proteínas así como las moléculas de ADN (ver Fig. 1.3) y ARN son el mejor ejemplo de sistemas moleculares que participan en procesos de almacenamiento y transferencia de información [12]. En particular, las proteínas, que son la base de los organismos vivos, son cadenas de aminoácidos cuya secuencia viene determinada por el código genético encriptado en el ADN que es descifrado con ayuda del ARN en el proceso de transcripción.

A la vista de todos estos ejemplos, parece claro que la gran variedad de sistemas complejos moleculares que aparecen en la naturaleza y otros, que han sido diseñados artificialmente, constituyen un campo de estudio muy rico y con grandes posibilidades de aplicaciones futuras[a].

Electrónica molecular Desde hace algunos años, tanto los químicos como los físicos moleculares han intentado dar forma a la idea de una electrónica basada en sistemas orgánicos y moleculares que pudiera sustituir, o al menos complementar, la electrónica actual basada en componentes de silicio [7]. El interés más práctico de esta propuesta es la

[a]Para más información sobre este tema, ver Ref. [18].

miniaturización de los dispositivos aunque el objetivo final es mucho más ambicioso, y trata de aprovechar la variedad de estructuras y funciones de sistemas moleculares para construir todos los elementos típicos de un circuito: conductores, interruptores, elementos lógicos y de almacenamiento. Gran parte de la investigación interdisciplinar actual está dedicada al desarrollo de esta idea desde un punto de vista teórico y también práctico.

Los sustitutos de los típicos conectores en la electrónica actual serían los llamados cables moleculares. Ciertos polímeros y polienos pueden de hecho conducir la corriente, presentando un comportamiento conductor que depende de sus características concretas [19]. Sin embargo, la complejidad estructural de estos materiales hace que en su fabricación aparezcan frecuentemente defectos no deseados que afectan su conductividad. Por el contrario, dentro del grupo de compuestos de carbono, los nanotubos de carbono se pueden sintetizar de manera mucho más controlada y también pueden comportarse como metales o semiconductores [21]. De hecho, se les puede inducir una transición metal-aislante o metal-semiconductor variando el campo eléctrico o magnético que se les aplique [22]. En esta discusión vale la pena comentar las propiedades conductoras de moléculas de ADN que, aunque contradictorias según las condiciones experimentales, son muy prometedoras, e incluso han dado lugar ya a varias propuestas específicas de dispositivos electrónicos basados en ADN [24].

En cuanto a los interruptores de un circuito opto-electrónico, las moléculas candidatas a realizar dicho papel son aquellas que presentan propiedades de biestabilidad en presencia de radiación óptica o campos eléctricos o magnéticos. Dicha biestabilidad aparece en moléculas como los fúlgidos y algunos agregados-J [26].

La interacción luz-materia también ha de ser tenida en cuenta en el diseño de elementos de almacenamiento de datos. En este sentido podría ser posible transformar de forma reversible el estado inicial molecular del sistema en otro diferente y distinguible del original por la acción de la luz. El efecto *hole-burning* [27] daría lugar a esta funcionalidad en sistemas cuyas lineas espectrales estén ensanchadas inhomogéneamente debido a interacciones con el entorno, como en el caso de agregados-J.

Otra posible aportación de los sistemas moleculares en electrónica es la transferencia de energía, que no de corriente eléctrica, como ya se planteó en la sección anterior cuando se discutieron las propiedades de los complejos antena típicos de la fotosíntesis y otros pertenecientes a la familia de los agregados-J [16, 17].

Por otra parte, las propiedades de reconocimiento selectivo y de autoensamblaje de

ciertos sistemas moleculares sería de enorme utilidad en el diseño y fabricación de componentes electrónicos moleculares [11], evitando así los problemas típicos de la litografía convencional. De hecho, el autoensamblaje de estos sistemas se determina básicamente por la estructura inicial de componentes individuales que actúan como patrón en el proceso e incluso, en algunos casos, se podrían usar moléculas biológicas ya existentes como la semilla inicial en el crecimiento. Este tipo de propiedades han sido claramente probadas en el caso del ADN por ejemplo [29, 30].

Efectos del desorden El desorden puede surgir en sólidos cristalinos debido a defectos no intencionados en forma de impurezas, vacantes o dislocaciones o también puede darse debido a la diferencia de entornos locales de distintos componentes del material, que es lo que ocurre normalmente en el caso de sistemas moleculares. Si el desorden que afecta al sistema en una dimensión es no correlacionado (que sería el caso análogo al modelo de Anderson en 3D [31]), entonces se puede demostrar que todos los autoestados del Hamiltoniano están completamente localizados [32, 33]. Por el contrario, se sabe que si el desorden presenta ciertos tipos de correlaciones, esto puede resultar en la delocalización de los estados en el límite termodinámico [34–37]. Por otro lado, se ha de tener en cuenta que en ciertos casos la longitud de localización del estado, aún no siendo infinita, puede alcanzar valores mayores que el tamaño del sistema y por tanto, dicho estado se comportará de manera análoga a estados estrictamente extendidos en cuanto al transporte se refiere. Las propiedades de localización determinarán, por tanto, los procesos de transporte de energía y carga de manera que puedan tener lugar procesos de transporte coherente, de transporte incoherente, o una superposición de ambos mecanismos dependiendo de las características particulares del sistema [38].

En agregados moleculares como los agregados-J, la principal fuente de desorden surge de la variedad de entornos locales que afectan a las moléculas del agregado, y que dan lugar a perturbaciones de los niveles moleculares dependiendo del entorno particular [39]. Esto da lugar a un ensanchamiento inhomogéneo del espectro de absorción que ha sido claramente observado en experimentos [40].

En el caso de biomoléculas, como los polímeros de ADN, la situación es mucho más complicada. En primer lugar el desorden aparece implícito en la secuencia de nucleótidos del ADN, lo que tiene una gran influencia en las propiedades de localización de los estados de la molécula [41]. Además, en vivo y en la mayoría de situaciones experimentales, el ADN

se ve expuesto a diversas condiciones ambientales que pueden alterar su estructura y sus propiedades. Por ejemplo, las moléculas de agua y otros iónes alcalinos que se encuentran en disolución con las moléculas de ADN, pueden interaccionar con los átomos de los azúcares y fosfatos que constituyen su esqueleto, induciendo fluctuaciones locales de las energías de sitio de las nucleobases. Dichos iones y moléculas además pueden introducir estados dentro del intervalo prohibido de energía electrónico de las moléculas de ADN similares a aquellos creados por impurezas en semiconductores convencionales, y a través de los cuales se puede activar térmicamente el transporte incoherente [42]. Es más, las fluctuaciones dinámicas de los iónes alcalinos también pueden dar lugar a configuraciones concretas del ADN que favorezcan o inhiban el transporte. En concreto, debido a la alta deformabilidad de algunas moléculas orgánicas como los polímeros de ADN, los efectos dinámicos del desorden pueden excitar modos de vibración de la cadena de nucleótidos de baja energía que se pueden acoplar al transporte coherente de carga. En este sentido, el estudio de las interacciones entre carga y fonones es imprescindible, teniendo en cuenta que incluso puede dar lugar a la formación de estados polarónicos [43].

A la vista de todos estos argumentos queda claro que los efectos del desorden han de ser considerados al estudiar las propiedades físicas de sistemas moleculares, los cuales se ven fuertemente afectados por las condiciones del entorno.

Principales objetivos de la Tesis

En secciones anteriores se ha discutido la relevancia de un estudio de los sistemas moleculares complejos en profundidad debido a su aplicabilidad en diferentes campos tales como la física, la química, la electrónica o la computación. La gran variedad de este tipo de sistemas, así como los diferentes entornos por los que se pueden ver afectados, hace que su descripción completa sea claramente no trivial. Por eso, es necesaria una intensa colaboración interdisciplinar para desarrollar modelos sencillos basados en interacciones efectivas cuya aplicación nos lleve a una comprensión básica de sus propiedades principales. Esta Tesis presenta el estudio de las propiedades ópticas y de transporte de sistemas uni- y quasiuni-dimensionales a través de modelos de enlace fuerte cuya efectividad ha sido ampliamente demostrada con anterioridad [44–47]. En concreto nuestro trabajo se centra en dos tipos de sistemas: agregados moleculares lineales y moléculas de ADN.

En el ***Capítulo 2*** se estudian las propiedades de localización de un Hamiltoniano

de Frenkel desordenado en una dimensión. La distribución de desorden, que se introduce directamente en las energías de sitio, presenta correlaciones de largo alcance. En el caso de sistemas con correlación fuerte, se exponen claras evidencias de una transición de Anderson en el centro de la banda. El efecto de dichas correlaciones sobre los espectros de absorción de agregados lineales se estudia en el ***Capítulo 3***. En concreto, se demuestra numéricamente la aparición de un patrón periódico en tales espectros cuando las correlaciones son suficientemente intensas y que es atribuido a la cuantización de Stark-Wannier. En el ***Capítulo 4*** establecemos una clara relación entre dicha periodicidad de las líneas de absorción y el decaimiento fluorescente de excitaciones excitónicas.

El ***Capítulo 5*** está dedicado al estudio de las propiedades de localización de un modelo en escalera de ADN a través del cálculo de los exponentes de Lyapunov y de Landauer. Se demuestra que las correlaciones intrínsecas al ADN debido a la complementariedad entre nucleobases, no pueden justificar en ningún caso la aparición de estados extendidos en este sistema. De hecho, se discute la poca relevancia que tienen éstas en la localización de los estados, al contrario de lo que sucede con las integrales de intercambio del Hamiltoniano.

El espectro de absorción de homopolímeros de ADN se analiza en el ***Capítulo 6*** utilizando diferentes modelos en escalera. Proponemos que la caracterización de estos espectros puede contribuir favorablemente a una mejor descripción de los parámetros efectivos del Hamiltoniano de enlace fuerte. En nuestro estudio consideramos también posibles efectos del desorden y de la geometría helicoidal del ADN. Además, se introduce brevemente una propuesta experimental al final de este capítulo, señalando las dificultades que han de ser consideradas en el diseño real del experimento de absorción óptica de estas moléculas de ADN.

Los ***Capítulos 7*** y **8** estan enfocados al estudio de propiedades de transporte de homopolímeros de ADN. En el ***Capítulo 7*** se propone un formalismo teórico basado en procesos de transporte incoherente que describe correctamente las curvas semiconductoras de corriente-voltaje observadas en algunos experimentos. Simulando los efectos del entorno como una contribución desordenada a las energías de las nucleobases, demostramos que el comportamiento metálico, también observado en algunos experimentos, no puede ser reproducido por el formalismo teórico propuesto. Por otra parte, el ***Capítulo 8*** se dedica al estudio de transporte coherente en presencia de campos eléctricos en el modelo de Peyrard-Bishop-Holstein para ADN, donde se incluye el acoplamiento entre la carga y la propia cadena de nucleobases. En este caso se demuestra que pueden aparecer corrientes

alternas en el rango de los terahercios en este modelo, tanto en el caso de cadenas uniformes como en el de aquellas que presenten correlaciones de largo alcance.

Conclusiones y perspectivas

Propiedades anómalas de un modelo de desorden con correlaciones de largo alcance en una dimensión En los Capítulos 2, 3 y 4 hemos estudiado a través de un Hamiltoniano de Frenkel las propiedades ópticas y de transporte del modelo unidimensional de desorden propuesto en la Ref. [50]. Este modelo presenta correlaciones de largo alcance cuya intensidad depende del exponente de correlación α, de manera que para $\alpha > \alpha_c$ el modelo presenta ciertas propiedades anómalas. La más destacada es la existencia de una transición localizado-deslocalizado en este modelo cuando $\alpha > \alpha_c \approx 2$ [50–52]. En la presente Tesis se han aportado nuevas y más generales evidencias de esta transición de Anderson basadas en el cálculo de la IPR y el coeficiente de transmisión de los autoestados del sistema. Con estos resultados se obtuvo un mapa de fases relacionado con las propiedades de localización del sistema y se demostró que aparece un fase de estados extendidos en el centro de la banda cuando $\alpha > 2$, que además presenta una transmisión perfecta. Nuestros resultados deben ser tenidos en consideración por completitud ya que se obtuvieron promediando sobre un amplio conjunto de realizaciones de desorden, y son consistentes con otros de trabajos previos donde sólo se tuvo en cuenta una única realización [50, 51]. Analizando los espectros de absorción lineales en este tipo de sistemas, encontramos que la línea de absorción típica del modelo de Frenkel ordenado se desdobla cuando $\alpha > \alpha_c$, constituyendo este hecho una nueva anomalía del modelo. Además, proponemos una simplificación de la distribución de desorden original en el caso de correlaciones suficientemente intensas que explica a la perfección nuestros resultados numéricos [203].

Debido a la existencia de dicha fase extendida cuando $\alpha > \alpha_c$, se demostró en la Ref. [78] que una cuasipartícula puede realizar oscilaciones de Bloch coherentes en una sistema generado a partir del modelo de desorden en estudio. En este sentido, el Capítulo 3 se ha dedicado al estudio de la cuantización de Stark-Wannier en el dominio de frecuencias, la cual es típica de sistemas donde aparece el fenómeno de oscilaciones de Bloch cuando se les aplica un campo eléctrico uniforme. Demostramos que en esta situación debido a la coexistencia de efectos relativos al campo y al desorden, la intensidad de las correlaciones y del campo facilitan la aparición de dicha discretización periódica. En concreto, cuando

el campo es lo suficientemente intenso, encontramos una estructura periódica de líneas espectrales con el mismo desdoblamiento que presenta la línea de absorción en el caso sin campo [204].

A la vista de la absorción óptica lineal de este tipo de sistemas, la relajación intrabanda de estados excitónicos se consideró en el Capítulo 4. Para ésto se hizo uso de un formalismo basado en la ecuación maestra de Pauli para estudiar el decaimiento fluorescente de una configuración inicialmente excitada por un pulso de banda ancha. Nuestros resultados muestran que existe una correspondencia biunívoca entre la cuantización de Stark-Wannier en los espectros de absorción y la dependencia exponencial del decaimiento de fluorescencia con el tiempo. Por último evaluamos la relevancia de los efectos de tamaño finito del sistema en nuestro estudio y demostramos que nuestras conclusiones mas relevantes no son consecuencia de dichos efectos, si no de las características particulares del modelo de desorden considerado [205].

Propiedades ópticas y de transporte de moléculas de ADN Nuestro estudio comienza en el Capítulo 5 evaluando la importancia de las correlaciones por la complementariedad de nucleobases en secuencias aleatorias de ADN. Calculando los exponentes de Landauer y Lyapunov en un modelo de escalera para el ADN, se demuestra que dichas correlaciones no pueden dar lugar a la existencia de estados extendidos, ni estados con longitud de localización mayor que el tamaño del sistema (contrario a lo que se afirmó en la Ref. [131]). Por tanto, estas correlaciones intrínsecas al ADN no pueden explicar el transporte a lo largo de moléculas de ADN a temperatura cero. Con estas mismos indicadores, y a través del estudio dinámico del numero de participación de un paquete de onda inicialmente localizado, demostramos que, aunque variemos los valores de las integrales de intercambio del Hamiltoniano dentro del rango considerado en la literatura, tampoco puede existir ningún estado extendido en el sistema.

En el caso de homopolímeros de ADN, como el poly(G)-poly(C), la situación es muy diferente. Debido a la periodicidad de estas secuencias aparecen dos bandas de estados separadas por un intervalo de energía prohibido bien definido, que se conocen como las bandas HOMO y LUMO [148]. Algunos curvas corriente-voltaje experimentales también confirman esta predicción teórica mostrando claramente un comportamiento semiconductor para este tipo de moléculas [118]. Sin embargo, existen otros datos experimentales que contradicen los anteriores, de manera que el comportamiento conductor de estas mues-

tras parece estar fuertemente definido por los efectos del entorno y de los contactos en la medida. En el Capítulo 6 proponemos otra posible caracterización del carácter semiconductor de moléculas de ADN poly(G)-poly(C) basada en el análisis de las transiciones ópticas entre las dos bandas mencionadas. Nuestro estudio muestra cuán importante es una correcta definición de los parámetros efectivos del modelo de enlace fuerte, tanto en valor como en signo, para el estudio del transporte y de la absorción de estas moléculas. De hecho, discutimos cómo sería posible obtener información directa sobre éstos a partir de las medidas experimentales de estas transiciones interbanda en la región del visible [207, 208]. Lamentablemente estas transiciones son muy débiles en general y es crucial diseñar muestras optimizadas, así como utilizar instrumentos de medidas sofisticados para poder detectarlas experimentalmente. Los efectos del entorno debido a la disolución en la que normalmente se encuentran las moléculas de ADN ha de ser tenido en cuenta también en el diseño del experimento. En este capítulo modelamos estos efectos introduciendo una perturbación desordenada en los niveles energéticos de las nucleobases y demostramos que estos dan lugar a la aparición de nuevos estados dentro del intervalo prohibido de energía electrónico original del sistema ordenado. Debido a esto, cuanto mayor sea la interacción con el entorno de la disolución, más difícil será la detección de tales transiciones ópticas en el visible. Esto implica que sean preferibles los experimentos sobre moléculas de ADN *secas*, es decir, que no se encuentren en disolución.

En el Capítulo 7 proponemos un formalismo basado en la ecuación maestra de Pauli que, permitiendo la activación térmica del transporte incoherente, tenga en cuenta efectos dinámicos del entorno. En el caso del sistema ordenado nuestros resultados confirman claramente las evidencias experimentales de un comportamiento semiconductor para el ADN para un conjunto particular de parámetros del Hamiltoniano de enlace fuerte. Cuando se incluyen en este formalismo los efectos estáticos del posible desorden presente en el sistema, todos los autoestados se localizan completamente de acuerdo con las teorías de escala [33]. Así, se esperaría que en esta situación el transporte incoherente se viera térmicamente activado por medio de la participación de los nuevos estados inducidos por efectos del desorden en el interior del intervalo prohibido de energía. Siguiendo este razonamiento, intentamos explicar aquellos resultados experimentales que demuestran que el ADN puede comportarse también como un metal. Sin embargo, de acuerdo con nuestro formalismo, la energía típica de los fonones activados a temperatura ambiente es mucho menor que aquella requerida para que el portador pudiera saltar incoherentemente entre los estados

internos al intervalo prohibido de energía. Lo mismo ocurre cuando introducimos correlaciones de largo alcance en la contribución estática del desorden. Por eso, según nuestro modelo teórico, el transporte incoherente cuando la caída de potencial en la cadena es pequeña, no puede ser activado por fonones a temperatura ambiente cuando los efectos del entorno son relevantes, y por tanto, nuestra propuesta no puede explicar simultáneamente el carácter semiconductor y metálico del ADN observado experimentalmente [209].

En el Capítulo 8 se considera la interacción entre la carga y las vibraciones de la red con un enfoque diferente, en particular, con el que fue usado por el modelo PBH para describir las curvas de desnaturalización de ADN [196]. Así, estudiamos la dinámica de estados polarónicos en moléculas homogéneas de ADN en presencia de campos eléctricos uniformes y demostramos que, en ausencia de efectos disipativos, pueden surgir oscilaciones de Bloch en el modelo, que además dan lugar a corrientes alternas en el rango de los terahercios [202]. Estos resultados se confirman también incluso en el caso de moléculas de ADN no uniformes, siempre que existan correlaciones de largo alcance en la secuencia energética de las moléculas [210].

Perspectivas Respecto a los Capítulos 2, 3 y 4 parece claro que tanto la caracterización del modelo de desorden propuesto en Ref. [50], como su comprensión a través de la simplificación argumentada en esta Tesis, son suficientemente satisfactorias. El próximo paso en este estudio sería comprobar experimentalmente nuestras predicciones teóricas. El modelo de Frenkel que hemos usado es considerado como una buena herramienta para describir las propiedades de agregados-J por ejemplo [26]. Sin embargo, sería muy difícil introducir el efecto de un desorden tan específico como el estudiado en las moléculas del agregado. Aún así, ha de tenerse en cuenta que nuestros resultados también son validos para otros sistemas cuyas propiedades puedan ser descritas por un Hamiltoniano de enlace fuerte similar. Por ejemplo, los átomos ultrafríos atrapados en redes ópticas creadas por láser, y que por tanto, son más fácilmente controlables, podrían ser uno de los escenarios más prometedores para comprobar experimentalmente nuestras predicciones. Por otra parte, a pesar de la probada existencia de correlaciones de largo alcance en secuencias de ADN, todavía no se ha establecido una directa aplicabilidad del modelo propuesto en la Ref. [50] en este respecto. De hecho, mientras que la distribución de desorden Eq. (2.2) aporta valores continuos de las variables, las moléculas de ADN están compuestas únicamente por cuatro nucleobases. Por tanto, sería necesario desarrollar una extrapolación del

modelo de desorden considerado que fuera consistente con la naturaleza discreta del ADN. En este sentido, ya se propuso un modelo de desorden dicotómico que tenía en cuenta los dos pares de bases posibles en secuencias de ADN: GC y AT. Esta propuesta, aunque incluía las correlaciones de largo alcance, no era capaz de reproducir una transición localizado-deslocalizado que pudiera ser la explicación al transporte de largo alcance en ADN [54].

En cuanto a las propiedades conductoras del ADN, la conclusión más obvia de nuestro estudio es que es fundamental mejorar la calidad de las muestras, así como la de las condiciones de medida, para obtener una descripción unificada de dichas propiedades. Por nuestra parte, creemos que los homopolímeros de ADN y también las secuencias de ADN en las que aparezcan correlaciones de largo alcance, son buenos candidatos para que tenga lugar transporte de larga alcance siempre que los efectos del entorno sean minimizados, como en el caso de ADN seco. Realmente creemos que nuestra propuesta para definir el carácter conductor del ADN a través de las transiciones interbandas es muy prometedora, puesto que evita efectos no deseados debido a los contactos eléctricos. Por eso, valdría la pena diseñar muestras periódicas de ADN de calidad y caracterizar cuidadosamente sus propiedades estructurales en disoluciones muy concentradas que darían lugar a una absorción más intensa y más fácilmente detectable. Por otra parte, resulta claro que es imprescindible describir rigurosamente los efectos del entorno en este tipo de sistemas que normalmente se ven embebidos en disoluciones con otras moléculas, cuyas dinámicas se definen en escalas temporales diferentes. De la misma manera, debido a la fácil deformabilidad de las moléculas de ADN, la interacción entre carga y fonones ha de considerarse necesariamente en el marco de modelos polarónicos. En este respecto, aunque el modelo PBH ha resultado una buena herramienta para describir procesos de desnaturalización del ADN [196], los estados de polaron que contempla están localizados en regiones demasiado grandes comparadas con el tamaño común de las muestras usadas en experimentos. De acuerdo con esto, los modelos de polaron pequeño ofrecen nuevas posibilidades para describir el transporte a lo largo de ADN [211].

Bibliography

[1] G. W. Gokel, *Advances in Supramolecular Chemistry*. Cerberus Press, (2002).

[2] F. Zhao and M. Zhao, Recent. Res. Devel. Physics **6**, 1 (2005).

[3] K. Ariga and T. Kunitake, *Supramolecular Chemistry-Fundaments and Applications*. Springer, (2006).

[4] J. M. Lehn. *Supramolecular Chemistry: Concepts and Perspectives*. WCH, Weinhein, (1995).

[5] G. R. Desiraju, Nature **412**, 397 (2001).

[6] C. A. Schalley, *Analytical Methods in Supramolecular Chemistry*. Wiley-VCH, (2007).

[7] M. C. Petty and M. Petty, *Molecular Electronics: From Principles to Practice*. Wiley-Interscience, (2007).

[8] C. K. Chiang, C. R. Fincher, Y. W. Park, A. J. Heeger, H. Shirakawa, E. J. Louis, S. C. Gau, and Alan G. MacDiarmidand, Phys. Rev. Lett **39**, 1098 (1977).

[9] M. Kyotani, S. Matsushita, T. Nagai, Y. Matsui, and K. Akagi, Synthetic Metals **157**, 546 (2007).

[10] D. E. Koshland, Angew. Chem. Int. Ed. **33**, 2375 (1994).

[11] O. Ikkala and G. ten Brinke, Science **295**, 2407 (2002).

[12] J. M. Berg, J. L. Tymozco, L. Stryer, and N. D. Clarke, *Biochemistry*. W. H. Freeman and Co., (2002).

[13] J. J. Wolken, *Light detector, photoreceptors and imagin in nature*. Oxford University Press US, (1995).

[14] T. H. James, *The theory of the photographic process*. Macmillan, New York, (1977).

[15] A. H. Hertz, Adv. Colloid Interface Sci. **8**, 237 (1977).

[16] S. Tretiak, C. Middleton, V. Chernyak, and S. Mukamel, J. Phys. Chem. B **104**, 4519 (2000).

[17] V. Sundström and R. van Grondelle, J. Opt. Soc. Am. B **7**, 1595 (1990).

[18] H. Haken and H. C. Wolf, *Molecular physics and Elements of Quantum Chemistry*. Springer-Verlag Berlin Heidelberg, (1995).

[19] M. S. Freund and R. H. Hall, *Self-doped conducting Polymers*. John Wiley and Sons, (2007).

[20] P. Dounis, W. J. Feast, and G. Widaski, J. Mol. Catal. A **115**, 51 (1997).

[21] C. Dekker, Phys. Today **52**, 22 (1999).

[22] W. Ch. Henk, T. Teepen, Z. Yao, M. Grifoni, and C. Dekker, Science **293**, 5527 (2001).

[23] M. Di Ventra and M. Zwolak, *DNA electronics*. Encyclopedia of Nanoscience and Nanotechnology, **X**, 1-19 (2004).

[24] A. V. Malyshev, Phys. Rev. Lett. **98**, 096801 (2007).

[25] Y. Yokoyama, Chem. Rev. **100**, 1717 (2000).

[26] T. Kobayashi, *J-Aggregates*. World Scientific, Singapore (1996).

[27] L. Johnson, The Laser Journal **7**, 1 (1986).

[28] H. Wendt and J. Friedrich, Chem. Phys. **210**, 101 (1996).

[29] N. C. Seeman, Nature **421**, 427 (2003).

[30] H. Yan, S. H. Park, G. Finkelstein,, J. H. Reif, and T. H. LaBean, Science **301**, 1882 (2003).

[31] P. W. Anderson, Phys. Rev. **109**, 1492 (1958).

[32] N. F. Mott and W. D. Twose, Adv. Phys. **10**, 107 (1961).

[33] E. Abrahams, P. W. Anderson, D. C. Licciardello, and V. Ramakrishnan, Phys. Rev. Lett. **42**, 673 (1979).

[34] J. C. Flores, Condens. Matter **1**, 8471 (1989).

[35] P. Phillips and H. L. Wu, Science **252**, 1805 (1991).

[36] J. C. Flores and M. Hilke, J. Phys. A **26**, L1255 (1993).

[37] F. Domínguez-Adame, E. Maciá, and A. Sánchez, Phys. Rev. B. **48**, 6054 (1993).

[38] R. Gutiérrez and G. Cuniberti, Proc. SPIE **5838**, 182 (2005).

[39] E. Gaizauskas and K. H. Feller, J. Mol. Struct. **598**, 45 (2001).

[40] P. Argyrakisb, D. M. Baskoa, M. A. Drobizheva, A. N. Lobanova, A. V. Pimenova, O. P. Varnavskya, M. Van der Auweraerc, and A. G. Vitukhnovskya, Chem. Phys. Lett. **268**, 372 (1997).

[41] S. Roche, Phys. Rev. Lett. **91**, 108101 (2003).

[42] J. Jortner, M. Bixon, T. Langenbacher, and M. E. Michel-Beyerle, Proc. Natl. Acad. Sci. USA, **95**, 12759 (1998).

[43] C. M. Chang, A. H. Castro, and A. R. Bishop, Chem. Phys. **303**, 189 (2004).

[44] G. Cuniberti, L. Craco, D. Porath, and C. Dekker, Phys. Rev. B **65**, 241314 (2002).

[45] D. Klotsa, R. A. Römer, and M. S. Turner, Biophys. J. **89**, 2187 (2005).

[46] E. Maciá and S. Roche, Nanotechnology **17**, 3002 (2006).

[47] R. Gutiérrez, S. Mohapatra, H. Cohen, D. Porath, and G. Cuniberti, Phys. Rev. B **74**, 235105 (2006).

[48] See http://www.nobel.se/physics/laureates/1977.

[49] V. Bellani, E. Díez, R. Hey, L. Toni, L. Tarricone, G. B. Parravicini, F. Domínguez-Adame, and R. Gómez-Alcalá, Phys. Rev. Lett. **82**, 2159 (1999).

[50] F. A. B. F. de Moura and M. L. Lyra, Phys. Rev. Lett. **81**, 3735 (1998).

[51] F. M. Izrailev and A. A. Krohin, Phys. Rev. Lett. **82**, 4062 (1999).

[52] H. Shima, T. Nomura, and T. Nakayama, Phys. Rev. B **70**, 075116 (2004).

[53] M. Paczuski, S. Maslov, and P. Bak, Phys. Rev. E **53**, 414 (1996).

[54] P. Carpena, P. Bernaola-Galván, P. Ch. Ivanov, and H. E. Stanley, Nature **418**, 955 (2002); *ibid* **421**, 764 (2003).

[55] P. Carpena, P. Bernaola-Galán, and Ch. Ivanov, Phys. Rev. Lett. **93**, 176804 (2004).

[56] H. Yamada, Phys. Lett. A **332**, 65 (2004).

[57] U. Kuhl, F. M. Izrailev, A. A. Krokhin, and H. J. Stoeckmann, Appl. Phys. Lett. **77**, 633 (2000).

[58] W. H. Press, S. A. Teukolsky, W. T. Vetterling, and B. P. Flannery, *Numerical Recipes in C*. Cambridge University Press, Cambridge (1989).

[59] E. Maciá and F. Domínguez-Adame, *Electron, phonons, and excitons in low-dimensional aperiodic systems*. Editorial Complutense, Madrid (2000).

[60] S. Russ, J. W. Kantelhardt, A. Bunde, S. Havlin, and I. Webman, Physica A **266**, 492 (1999).

[61] V. A. Malyshev, A. Rodríguez, and F. Domínguez-Adame, Phys. Rev. B **60**, 14140 (1999).

[62] W. A. Harrison, *Solid State Theory*. Dover Publications, (1980).

[63] F. Bloch, Z. Phys. **52**, 555 (1928).

[64] C. Zener, Proc. R. Soc. London, Ser. A **145**, 523 (1934).

[65] D. H. Dunlap and V. M. Kenkre, Phys. Lett. A **127**, 438 (1988).

[66] L. Esaki and R. Tsu, IBM J. Res. Div. **14**, 61 (1970).

[67] N. W. Ashcroft, and N. D. Mermin, *Solid State Physics*. Saunders Colledge Publishers, New York, (1976).

[68] J. Feldmann, K. Leo, J. Shah, D. A. B. Miller, J. E. Cunningham, T. Meier, G. von Plessen, A. Schulze, P. Thomas, and S. Schmitt-Rink, Phys. Rev. B **46**, R7252 (1992).

[69] K. Leo, P. Haring Bolivar, F. Brüggemann, R. Schwedler, and K. Köhler, Solid State Commun. **84**, 943 (1992).

[70] C. Waschke, H. G. Roskos, R. Schwedler, K. Leo, H. Kurz, and K. Köhler, Phys. Rev. Lett. **70**, 3319 (1993).

[71] T. Dekorsy, P. Leisching, K. Köhler, and H. Kurz, Phys. Rev. B **50**, R8106 (1994).

[72] R. Martini, G. Klose, H. G. Roskos, H. Kurz, H. T. Grahn, and R. Hey, Phys. Rev. B **54**, R14325 (1996).

[73] F. Löser, Yu. A. Kosevich, K. Köhler, and K. Leo, Phys. Rev. B **61**, R13373 (2000).

[74] K. Leo, Semicond. Sci. Technol. **13**, 249 (1998).

[75] M. BenDahan, E. Peik, J. Reichel, Y. Castin, and C. Salomon, Phys. Rev. Lett. **76**, 4508 (1996).

[76] S. R. Wilkinson, C. F. Bharucha, K. W. Madison, Q. Niu, and M. G. Raizen, Phys. Rev. Lett. **76**, 4512 (1996).

[77] B. P. Anderson and M. A. Kasevich, Science **282**, 1686 (1998).

[78] F. Domínguez-Adame, V. A. Malyshev, F. A. B. F. de Moura, and M. L. Lyra, Phys. Rev. Lett. **91**, 197402 (2003).

[79] G. H. Wannier, Phys. Rev. **117**, 432 (1960).

[80] M. C. Chang and Q. Niu, Phys. Rev. B **48**, 2215 (1993).

[81] E. E. Méndez, F. Agulló-Rueda, and J. M. Hong, Phys. Rev. Lett. **60**, 2426 (1988).

[82] F. Agulló-Rueda, E. E. Méndez, and J. M. Hong, Phys. Rev. B **40**, 1357 (1989).

[83] M. K. Saker, D. M. Whitteker, M. S. Skolnick, M. T. Emeny, and C. R. Whitehouse, Phys. Rev. B **43**, 4945 (1991).

[84] H. Fidder, J. Knoester, and D. A. Wiersma, J. Chem. Phys. **95**, 7880 (1991).

[85] V. Malyshev and P. Moreno, Phys. Rev. B **51**, 14587 (1995).

[86] A. V. Malyshev and V. A. Malyshev, Phys. Rev. B **63**, 195111 (2001).

[87] V. A. Malyshev, Opt. Spectrosk. **71**, 873 (1991) [Engl. Transl.: Opt. Spectrosc. **71**, 505 (1991)].

[88] E. W. Knapp, Chem. Phys. Lett. **85**, 73 (1984).

[89] D. H. Dunlap and V. M. Kenkre, Phys. Rev. B**34**, 3625 (1986).

[90] D. J. Heijs, V. M. Malyshev, and J. Knoester, J. Chem. Phys. **121**, 4884 (2004).

[91] S. Alexander, J. Bernasconi, W. R. Schneider, and R. Orbach, Rev. Mod. Phys. **53**, 175 (1981).

[92] J. W. Haus and K. W. Kehr, Phys. Rep. **150**, 263 (1987).

[93] V. M. Kenkre and Y. M. Wong, Phys. Rev. B **23**, 3748 (1981).

[94] R. M. Pearlstein, J. Chem. Phys. **56**, 2431 (1972).

[95] I. G. Scheblykin, Chem. Phys. Lett. **298**, 341 (1998).

[96] P. E. Parris, Phys. Rev. B **40**, 4928 (1989).

[97] D. L. Huber and W. Y. Ching, Chem. Phys. **146**, 409 (1990).

[98] D. L. Huber, Phys. Rev. B **45**, 8947 (1992).

[99] Z. G. Soos, and R. C. Powell, Phys. Rev. B **72**, 4035 (1972).

[100] H. Scher and C. H. Wu, Proc. Natl. Acad. Sci. USA. **78**, 22 (1981).

[101] J. W. Edwards and P. E. Parris, Phys. Rev. B **40**, 8045 (1989).

[102] A. Sánchez, F. Domínguez-Adame, and E. Maciá, Phys. Rev. B **51**, 173 (1995).

[103] A. V. Malyshev, V. A. Malyshev, and F. Domínguez-Adame, J. Phys. Chem. **107**, 4418 (2003).

[104] F. Domínguez-Adame and E. Maciá, Phys. Rev. B **53**, 13921 (1996).

[105] D. L. Huber and W. Y. Ching, Phys. Rev. B **42**, 7718 (1990).

[106] Th. Wagersreiter and H. F. Kauffmann, Phys. Rev. B **50**, 9102 (1994).

[107] M. Bednarz, V. A. Malyshev, and J. Knoester, J. Chem. Phys. **117**, 6200 (2002).

[108] M. Shimizu, S. Suto, and T. Goto, J. Chem. Phys. **114**, 2775 (2001).

[109] H. Fukuyama, R. A. Bari, and H. C. Fogedby, Phys. Rev. B **8**, 5579 (1973).

[110] C. Dekker and M.A. Ratner, *Electronic properties of DNA*. Physics World **14**, 29 (2001).

[111] V. R. P. Bajpai and L.M. Bharadwaj, European Mol. Biol. Rep. **4**, 442 (2003).

[112] R. G. Endres, D. L. Cox, and R. P. Singh, Rev. Mod. Phys. **76**, 195 (2004).

[113] D. Porath, G. Cuniberti, and R. Di Felice, Topics in Current Chemistry **237**, 183 (2004).

[114] Y. Okahata, T. Kobayashi, K. Tanaka, and M. J. Shimomura, J. Am. Chem. Soc. **120**, 6165 (1998).

[115] H. W. Fink and C. Schönenberger, Nature **398**, 407 (1999).

[116] A. Rakitin, P. Aich, C. Papadopoulos, Yu. Kobzar, A. S. Vedeneev, J. S. Lee, and J. M. Xu, Phys. Rev. Lett. **86**, 3670 (2001).

[117] O. Legrand, D. Côte, and U. Bockelmann, Phys. Rev. E **73**, 031925 (2006).

[118] D. Porath, A. Bezryadin, S. de Vries, and C. Dekker, Nature **403**, 635 (2000).

[119] K.-H. Yoo, D. H. Ha, J.-O. Lee, J. W. Park, J. Kim, J. J. Kim, H.-Y. Lee, T. Kawai, and H. Y. Choi, Phys. Rev. Lett. **87**, 198102 (2001).

[120] J. S. Hwang, K. J. Kong, D. Ahn, G. S. Lee, D. J. Ahn, and S. W. Hwang, Appl. Phys. Lett. **81**, 1134 (2002).

[121] B. Q. Xu, P. M. Zhang, X. L. Li, and N. J. Tao, NanoLett. **4**, 1105 (2004).

[122] H. Cohen, C. Nogues, R. Naaman, and D. Porath, Proc. Natl. Acad. Sci. **102**, 11589 (2005).

[123] S. Roy, H. Vedala, A. Datta Roy, D.-H. Kim, M. Doud, K. Mathee, H.-K. Shin, N. Shimamoto, V. Prasad, and W. Choi, NanoLett. **8**, 26 (2008).

[124] E. Braun, Y. Eichen, U. Sivan, and G. Ben-Yoseph, Nature **391**, 775 (1998).

[125] A. J. Storm, J. van Noort, S. de Vries, and C. Dekker, Appl. Phys. Lett. **79**, 3881 (2001).

[126] P. J. de Pablo, F. Moreno-Herrero, J. Colchero, J. Gómez Herrero, P. Herrero, A. M. Baró, P. Ordejón, J. M. Soler, E. Artacho, Phys. Rev. Lett. **85**, 4992 (2000).

[127] A. Yu. Kasumov, M. Kociak, S. Guéron, B. Reulet, V. T. Volkov, D. V. Klinov, and H. Bouchiat, Science **291**, 280 (2001).

[128] S. Roche, D. Bicout, E. Maciá, and E. Kats, Phys. Rev. Lett. **91**, 228101 (2003).

[129] M. Unge and S. Stafstrom, Nano Lett. **3**, 1417 (2003).

[130] S. Roche and E. Maciá, Mod. Phys. Lett. **18**, 847 (2004).

[131] R. A. Caetano and P. A. Schulz, Phys. Rev. Lett. **95**, 126601 (2005); *ibid.* **96**, 059704 (2006).

[132] A. Sedrakyan and F. Domínguez-Adame, Phys. Rev. Lett. **96**, 059703 (2006).

[133] K. Iguchi, Int. J. Mod. Phys. B **11**, 2405 (1997).

[134] H. Sugiyama and I. Saito J. Am. Chem. Soc. **118**, 7063 (1996).

[135] H. Zhang, X. Li, P. Han, X. Yang Yu, and Y. Jan J. Chem. Phys. **117**, 9 (2002).

[136] T. Sedrakyan and A. Ossipov, Phys. Rev. B **70**, 214206 (2004).

[137] B. Kramer and A. Mckinnon, Rep. Prog. Phys. **56**, 1469 (1993).

[138] A. Crisanti, G. Paladin, M. Serva, and A. Vulpiani, Phys. Rev. Lett. **71**, 789 (1993).

[139] P. W. Anderson, D. J. Thouless, E. Abrahams, and D. S. Fisher, Phys. Rev. B **22**, 3519 (1980).

[140] R. Schrader, H. Schulz-Baldes, and A. Sedrakyan, Ann. Henri Poincare **5**, 1159 (2004).

[141] E. J. Macdonald and D. J. Higham, Elect. Trans. Num. Analysis **12**, 234 (2001).

[142] D. Sedrakyan and A. Sedrakyan, Phys. Rev. B **60**, 10114 (1999).

[143] T. Hakobyan, D. Sedrakyan, A. Sedrakyan, I. Gómez, and F. Domínguez-Adame, Phys. Rev. B **61**, 11432 (2000).

[144] Y. J. Yan and H. Zhang, J. Theor. Comp. Chem. **1**, 225 (2002).

[145] A. Voityuk, J. Jortner, M. Bixon, and N. Roesch, J. Chem. Phys. **114**, 5614 (2002).

[146] K. Senthilkumar, F. C. Grozema, C. F. Guerra, F. M. Bickelhaupt, F. D. Lewis, Y. A. Berlin, M. A. Ratner, and L. D. A. Siebbeles, J. Am. Chem. Soc. **127**, 14894 (2005).

[147] E. L. Albuquerque, M. L. Lyra, and F. A. B. F. de Moura, Physica A **370**, 625 (2006).

[148] P. O. Löwdin, Rev. Mod. Phys. **35**, 1587 (1963).

[149] K. Iguchi, J. Phys. Soc. Jpn. **70**, 593 (2001).

[150] K. Iguchi, Int. J. Mod. Phys. **13**, 1845 (2004).

[151] A. Rodríguez, R. A. Römer, and M. S. Turner, phys. stat. solidi (b) **243**, 373 (2006).

[152] V. M. Apalkov and T. Chakraborty, Phys. Rev. B **71**, 033102 (2005).

[153] H. Mehrez and M. P. Anantram, Phys. Rev. B **71**, 115405 (2005).

[154] J. Yi, Phys. Rev. B **68**, 193103 (2003).

[155] S. S. Mallajosyula, J. C. Lin, D. L. Cos, S. K. Pati, and R. R. P. Singh, Phys. Rev. Lett. **101**, 176805 (2008).

[156] The author acknowledges a hint from P. Orellana on decoupling the equations.

[157] E. Artacho, M. Machado, D. Sánchez-Portal, P. Ordejón, and J. M. Soler, Mol. Phys. **101**, 1587 (2003).

[158] The author acknowledges enlightening discussions with A. V. Malyshev on the relevance of symmetries for the selection rules.

[159] D. Porath, G. Cuniberti, and R. Di Felice, Top Curr. Chem. **237**, 183 (2004).

[160] M. N. Lipsett, J. Biol. Chem. **239**, 1256 (1964).

[161] A. B. Kotlyar, N. Borokov, T. Molotsky, L. Fadeev, and M. Gozin, Nucl. Acids Resarch. **33**, 525 (2005).

[162] K. Poon and R. B. Macgregor, Biopolymers **45**, 427 (1998).

[163] E. Shapir, H. Cohen, N. Borokov, A. B. Kotlyar, and D. Porath, J. Phys. Chem. B **110**, 4430 (2006).

[164] http://www.idtdna.com/Home/Home.aspx.

[165] M. Zuker and N. Markham, http://mfold.bioinfo.rpi.edu/.

[166] E. M. Southern, *Denaturing gel electrophoresis of RNA and DNA using urea-polyacrylamide gels*. Oxford-UK (2002)

[167] D. M. Lilley, Methods Enzymol **317**, 368 (2000).

[168] P. Saardyen, N. Jonoska, and N. C. Seeman, Natural Computing **2**, 427 (2003).

[169] R. McGookin, Meth. Mol. Biol. **4**, 75 (1988).

[170] R. Owczarzy, B. G. Moreira, Y. You, M. A. Behlke, and J. A. Walder, Biochemistry **47**, 5336 (2008).

[171] V. May and O. Kuehn, *Charge and energy transfer dynamics in molecular systems*. Wiley-VCH, Germany (2004)

[172] J. Koch, A. Zybin, and K. Niemax, Spectrochimica Acta Part B **57**, 1547 (2002).

[173] E. Helgren, G. Grüner, A. Omerzu, D. Mihailovic, R. Podgornik, and H. Grimm, cond–mat/0111299.

[174] A. Hubsch, R. G. Endres, D. L. Cox, and R. R. P. Singh, Phys. Rev. Lett. **94**, 178102 (2005).

[175] D. N. Beratan, S. Priyadarshy, and S. M. Risser, Chem. Biol. **4**, 3 (1997).

[176] E. Boon, A. Livinstong, N. Chmiel, S. David, and J. Barton, Proc. Nat. Acad. Sci. **100**, 12543 (2003).

[177] V. Apalkov and T. Chakraborty, Phys. Rev. B **72**, 161102 (2005).

[178] B. B. Schmidt, M. H. Hettler, and G. Schön, Phys. Rev. B **75**, 115125 (2007).

[179] R. Gutiérrez, S. Mandal, and G. Cuniberti, Phys. Rev. B **71**, 235116 (2005).

[180] W. Tian, S. Datta, S. Hong, R. G. Reifenberger, J. I. Henderson, and C. P. Kubiak, Physica E **1**, 304 (1997).

[181] J. A. Freire and G. Voss, J. Chem. Phys. **122**, 124705 (2005).

[182] M. S. Xu, S. Tsukamoto, S. Ishida, M. Kitamura, and Y. Arakawa, Appl. Phys. Lett. **87**, 083902 (2005).

[183] The author acknowledges A. V. Malyshev the crucial design of the iterative method to solve the nonlinear master equation.

[184] I. M. Lifshitz, Usp. Fiz. Nauk **83**, 617 (1964). [Sov. Phys. Usp. **1**, 549 (1965)].

[185] The author acknowledges enlightening discussions with A. V. Malyshev and V. A. Malyshev on the possibility of incoherent transport mediated by disorder-induced midgap states.

[186] A. V. Malyshev, phys. stat. sol. (c) **3**, 3539 (2006).

[187] E. M. Conwell and S. V. Rakhmanova, Proc. Natl. Acad. Sci. USA, **97**, 4556 (2000).

[188] D. Ly, Y. Kan, B. Armitage, and G. B. Schuster, J. Am. Chem. Soc. **118**, 8747 (1996).

[189] Y. A. Berlin, A. L. Burin, and M. A. Ratner, J. Phys. Chem. A **104**, 443 (2000).

[190] H. Yamada, E. B. Starikov, and D. Hennig, Eur. Phys. J. B **59**, 185 (2007).

[191] E. Maciá, Phys. Rev. B **76**, 245123 (2007).

[192] S. V. Rakhmanova and E. M. Conwell, J. Phys. Chem. B **105**, 2056 (2001).

[193] V. D. Lakhno and N. S. Fialko, Pis'ma ZhETF **79**, 575 (2004).

[194] A. V. Malyshev, V. A. Malyshev, and F. Domínguez-Adame, J. Lumin. in press (2009).

[195] M. Peyrard and A. R. Bishop, Phys. Rev. Lett. **62**, 2755 (1989).

[196] T. Dauxois and M. Peyrard, Phys. Rev. E **47**, R44 (1993).

[197] S. Komineas, G. Kalosakas, and A. R. Bishop, Phys. Rev. E **65**, 061905 (2002).

[198] G. Kalosakas, S. Aubry, and G. P. Tsinronis, Phys. Rev. B **58**, 3094 (1998).

[199] P. Maniadis, G. Kalosakas, K. Ø. Rasmunssen, and A. R. Bishop, Phys. Rev. E **72**, 021912 (2005).

[200] J. A. Berashevich, A. D. Bookatz, and T. Chakraborty, J. Phys.: Condens. Matter **20**, 035207 (2008).

[201] J. Ojeda, R. P. A. Lima, F. Domínguez-Adame, and P. Orellana, J. Phys.: Condens. Matter **21**, 285105 (2009).

[202] E. Díaz, R. P. A. Lima and F. Domínguez-Adame, Phys. Rev. B **78**, 134303 (2008).

[203] E. Díaz, A. Rodríguez, F. Domínguez-Adame, and V. A. Malyshev, Europhys. Lett. **72**, 1018 (2005).

[204] E. Díaz, F. Domínguez-Adame, Y. Kosevich, and V. A. Malyshev, Phys. Rev. B **73**, 174210 (2006).

[205] E. Díaz and F. Domínguez-Adame, Phys. Rev. B **77**, 134201 (2008).

[206] E. Díaz, A. Sedrakyan, D. Sedrakyan, and F. Domínguez-Adame, Phys. Rev. B **75**, 014201 (2007).

[207] E. Díaz, A. V. Malyshev, and F. Domínguez-Adame, Phys. Rev. B **76**, 205117 (2007).

[208] E. Díaz, J. Chem. Phys. **128**, 175101 (2008).

[209] A. V. Malyshev, E. Díaz, F. Domínguez-Adame, and V. A. Malyshev, J. Phys.: Condens. Matter **21**, 335105 (2009).

[210] E. Díaz and F. Domínguez-Adame, submitted.

[211] S. S. Alexandre, E. Artacho, J. M. Soler, and H. Chacham, Phys. Rev. Lett. **91**, 108105 (2003).

List of publications

1. *Anomalous optical absorption in a random system with scale-free disorder*.

   E. Díaz, A. Rodríguez, F. Domínguez-Adame, and V. A. Malyshev.

   Europhysics Letters **72**, 1018 (2005).

2. *Wannier-Stark ladder in the linear absorption of a random system with scale-free disorder*.

   E. Díaz, F. Domínguez-Adame, Y. Kosevich, and V. A. Malyshev.

   Physical Review B **73**, 174210 (2006).

3. *Absence of extended states in a ladder model of DNA*.

   E. Díaz, A. Sedrakyan, D. Sedrakyan, and F. Domínguez-Adame.

   Physical Review B **75**, 014201 (2007).

4. *Interband optical transitions in DNA-like systems*.

   E. Díaz, A. V. Malyshev, and F. Domínguez-Adame.

   Physical Review B **76**, 205117 (2007).

5. *Intraband exciton relaxation in a biased lattice with long-range correlated disorder*.

   E. Díaz and F. Domínguez-Adame.

   Physical Review B **77**, 134201 (2008).

6. *Analysis of the interband optical transitions: Characterization of synthetic DNA band structure*.

   E. Díaz.

   Journal of Chemical Physics **128**, 175101 (2008).

7. *Bloch like oscillations in the Peyrard-Bishop-Holstein model.*

   E. Díaz, R. P. A. Lima, and F. Domínguez-Adame.

   Physical Review B **78**, 134303 (2008).

8. *Environment effects on the electric conductivity of double stranded DNA molecules.*

   A. V. Malyshev, E. Díaz, F. Domínguez-Adame, and V. A. Malyshev.

   Journal of Physics: Condensed Matter **21**, 335105 (2009).

9. *Stable Bloch oscillations in ultracold atoms with time-dependent interaction.*

   Ch. Gaul, R. P. A. Lima, E. Díaz, C. A. Müller, and F. Domínguez-Adame.

   Physical Review Letters **102**, 255303 (2009).

10. *THz oscillating currents enhanced by long-range correlations in DNA..*

    E. Díaz and F. Domínguez-Adame.

    Submitted to Chemical Physics (2009).